LBNL-51380

ERNEST ORLANDO LAWRENCE BERKELEY NATIONAL LABORATORY

Femtosecond Studies of Electron Dynamics and Structure at Metal-Molecular Interfaces

André D. Miller

Chemical Sciences Division

July 2002

Ph.D. Thesis

REFERENCE COPY
Does Not
Circulate

Library Annex Reference
Lawrence Berkeley National Laboratory

LBNL-51380

Copy 1

DISCLAIMER

This document was prepared as an account of work sponsored by the United States Government. While this document is believed to contain correct information, neither the United States Government nor any agency thereof, nor The Regents of the University of California, nor any of their employees, makes any warranty, express or implied, or assumes any legal responsibility for the accuracy, completeness, or usefulness of any information, apparatus, product, or process disclosed, or represents that its use would not infringe privately owned rights. Reference herein to any specific commercial product, process, or service by its trade name, trademark, manufacturer, or otherwise, does not necessarily constitute or imply its endorsement, recommendation, or favoring by the United States Government or any agency thereof, or The Regents of the University of California. The views and opinions of authors expressed herein do not necessarily state or reflect those of the United States Government or any agency thereof, or The Regents of the University of California.

This report has been reproduced directly from the best available copy.

Ernest Orlando Lawrence Berkeley National Laboratory is an equal opportunity employer.

DISCLAIMER

This document was prepared as an account of work sponsored by the United States Government. While this document is believed to contain correct information, neither the United States Government nor any agency thereof, nor the Regents of the University of California, nor any of their employees, makes any warranty, express or implied, or assumes any legal responsibility for the accuracy, completeness, or usefulness of any information, apparatus, product, or process disclosed, or represents that its use would not infringe privately owned rights. Reference herein to any specific commercial product, process, or service by its trade name, trademark, manufacturer, or otherwise, does not necessarily constitute or imply its endorsement, recommendation, or favoring by the United States Government or any agency thereof, or the Regents of the University of California. The views and opinions of authors expressed herein do not necessarily state or reflect those of the United States Government or any agency thereof or the Regents of the University of California.

LBNL-51380

Femtosecond Studies of Electron Dynamics and Structure at Metal-Molecular Interfaces

André David Miller
Ph.D. Thesis

Department of Chemistry
University of California, Berkeley

and

Chemical Sciences Division
Ernest Orlando Lawrence Berkeley National Laboratory
University of California
Berkeley, CA 94720

July 2002

This work was supported by the Director, Office of Science, Office of Basic Energy Sciences, Chemical Sciences Division, of the U.S. Department of Energy under Contract No. DE-AC03-76SF00098.

Femtosecond Studies of Electron Dynamics and Structure at Metal-Molecular Interfaces

Copyright © 2002

by

André David Miller

The U.S. Department of Energy has the right to use this document
for any purpose whatsoever including the right to reproduce
all or any part thereof.

Abstract

Femtosecond Studies of Electron Dynamics and Structure at Metal-Molecular Interfaces

by

André David Miller

Doctor of Philosophy in Chemistry

University of California at Berkeley

Professor Charles B. Harris, Chair

Femtosecond angle resolved two photon photoemission spectroscopy is used to study the electronic structure and electron dynamics at interfaces. At interfaces of thiolates chemisorbed on Ag(111), the adsorbate molecular electronic orbitals are observed to be nondispersive at low coverages and become dispersive at higher coverages. This is attributed to a phase transition of the layer. The molecules initially adsorb with their chains parallel to the surface. As the coverage is increased, the molecules order into a layer with the chains standing up from the surface. This closer packing results in a larger overlap between neighboring molecular orbitals and a dispersive electronic state. The lack of a change in the n=1 image potential state electron lifetimes as a function of chain length indicate that the electrons reside in the layer. The n=2 and 3 image potential state electron lifetimes decrease as the chain length is increased. This is attributed to the repulsive potential of

the alkyl chains pushing the electron density into the sulfur portion of the layer. At a layer of acetonitrile molecules adsorbed on Ag(111), the image potential state electrons interact strongly with the adsorbate molecular dipoles. The dipoles rotate to solvate the electron, resulting in a decrease of the observed photoemitted electron kinetic energy as a function of time delay between population and photoemission. This is attributed to a change in the local workfunction resulting from the reorganization of the adsorbate layer molecules. For two layers of acetonitrile adsorbed on the Ag(111) substrate, dynamic electron localization is also observed.

For my family

Contents

List of Figures vi

List of Tables viii

1 Introduction 1

2 Background 4
- 2.1 Substrate Electronic Structure 5
- 2.2 Surface States 9
  - 2.2.1 Image Potential States 10
  - 2.2.2 Adsorbate Electronic States 18

3 Experimental 20
- 3.1 Two Photon Photoemission 20
  - 3.1.1 Time Resolved Two Photon Photoemission 22
  - 3.1.2 Angle Resolved Two Photon Photoemission 23
- 3.2 Experimental Apparatus 26
- 3.3 Sample Preparation and Characterization 29
  - 3.3.1 Thiolate Self Assembled Monolayers 30
  - 3.3.2 Polar Acetonitrile Molecular Layers 34
- 3.4 Workfunction 36
  - 3.4.1 Global Workfunction 36
  - 3.4.2 Local Workfunction 41

4 A Self-Assembling Interface 43
- 4.1 SAM Adsorbate Electronic States 47
  - 4.1.1 Thiolate HOMO and LUMO Dispersions 48
  - 4.1.2 Coverage Dependence of the LUMO Dispersion 51
  - 4.1.3 Surface Phase Transition 54
- 4.2 Image Potential States at a SAM Interface 56
  - 4.2.1 Energies, Effective Masses and Lifetimes 56
  - 4.2.2 Dielectric Continuum Model Calculations 63

5 A Polar Molecular Interface **71**
5.1 Dynamic Kinetic Energies 72
5.1.1 Disk-Dipole Model 77
5.2 Localization 84

6 Conclusions **88**

Bibliography **92**

List of Figures

2.1 Band Structure of Silver 6
2.2 Bulk and Surface Brillouin Zones of Silver 7
2.3 Projected Bulk Band Structure 8
2.4 Image Interaction and Potential 11

3.1 Two Photon Photoemission 21
3.2 Wavelength Dependance of Photoelectron Kinetic Energies 22
3.3 Angle Resolved Two Photon Photoemission 25
3.4 Experimental Apparatus 27
3.5 Auger Electron Spectra of Thiolates/Ag(111) 31
3.6 Two Types of TPPE Spectra for Butylthiolate/Ag(111) 33
3.7 Acetonitrile Coverages: One to Two Layer Transition 35
3.8 Workfunction for Both an Infinite and a Finite Surface 37
3.9 Bias Potential Compensation for $V(z)$ 40

4.1 A Self Assembling Monolayer 45
4.2 Methylthiolate/Ag(111) UV-Vis and UV-UV Spectrum 46
4.3 Wavelength Dependence of Adsorbate Electronic States 49
4.4 Effective Mass Measurements for the Thiolate HOMO and LUMO 50
4.5 LUMO Dispersion Measurements at Three Exposures 52
4.6 Estimated Surface Coverage 53
4.7 Thiolate Assembly Mechanism 55
4.8 n=1 Image Potential State Dispersions 57
4.9 n=2 Image Potential State Dispersions 58
4.10 n=1 Image Potential State Lifetimes at Methylthiolate and Butylthiolate layers 60
4.11 n=2 and 3 Image Potential State Lifetimes at Methylthiolate and Butylthiolate layers 61
4.12 Dielectric Continuum Model n=1 Calculations 67
4.13 Dielectric Continuum Model n=2 Calculations 69

5.1 n=1 and n=2 Electron Solvation 73
5.2 n=1 IPS Electron Solvation for One and Two Layers of Acetonitrile 74

5.3 Local Workfunction Solvation of the IPS 76
5.4 Population Dynamics for the Acetonitrile Monolayer 78
5.5 Disk Dipole Model for the Local Workfunction 80
5.6 Disk-Dipole Potential for $R = d$, 100 Å and 10000 Å. 82
5.7 Localization of the n=1 IPS Electron at the Two Layer Acetonitrile Coverage 85
5.8 Population Dynamics of the n=1 IPS Electron 86

List of Tables

4.1 Energies, Lifetimes and Effective Masses of Image States at Thiolate/Ag(111) Interfaces 59
4.2 Calculated and Measured Lifetimes 70

Acknowledgements

The writing of a dissertation and the research that goes into achieving a Ph.D. are accomplishments made possible through the assistance and support of a great many people. As my advisor, Charles Harris has provided a fertile intellectual environment that has been essential to my growth as a scientist. Vijaya Narasimhan was essential to the daily administration of the group and navigation through the red tape of the university. Chung Wong and Kelly Gaffney trained both the experimentalist and the scientist in me. Simon Liu was a close companion through every stage of my graduate career. Paul Szymanski has been instrumental in the completion of my graduate work and extension beyond my small contribution. Sean Garrett-Roe and Ilya Bezel have taken the research in great new directions. All of my labmates have been wonderful companions as well as accomplished scientists.

My success within the academic world is due in no small part to the sanity, stress relief, perspective and grounding obtained through my friends and family. Ryan, Seth, Dave, and all of the sloths have been responsible for the laughter, good times, non-scientific mental exercise and support that has been essential to my outside life. Without my friends, this would have been impossible. My family are responsible for my initial conditions. My drive and ambition come from my mother, Brigitte. My curiosity and need to know why from my father, Dan. And from my brother Daniel, an awareness of the power of a view from a different paradigm as well as a vicarious enjoyment of a different path through and approach to life.

This work was supported by the Director, Office of Science, Office of Basic Energy

Sciences, Chemical Sciences Division of the U.S. Department of Energy, under Contract No. DE-AC03-76SF00098. The author acknowledges NSF support for specialized equipment used in the experiments described herein.

Chapter 1

Introduction

Electronic structure and electron dynamics at surfaces and interfaces are important in a wide variety of systems of both fundamental and technological interest. The electronic structure at an interface influences the efficiency of electron transfer across that interface. The dynamic interaction between the electron and the molecular media influence the scattering rate, mobility, lifetimes and spatial extent of the electron.

The electronic structure of molecules adsorbed onto a metal substrate is important to both device efficiency and surface electro- and photochemical reactions. Electron transfer into a dissociative molecular electronic state can induce dissociation and desorption [1–4]. Electron transfer from the metal into the molecular material is a crucial step in organic devices. The electronic structure of the organic layer at the interface strongly influences the efficiency of this transfer. Schottky barriers, the image potential and the electronic states of the media are all important to both thermal and photoinduced charge injection [5–9]. The two most important electronic states for charge injection are the highest occupied

molecular orbital (HOMO) and lowest unoccupied molecular orbital (LUMO) molecular electronic states or the valence and conduction bands formed from these states. Electrons are injected into the LUMO, whereas holes are injected into the HOMO.

Although the band structure of the substrate and its influence on the interfacial electronic structure is important, a specific probe of the surface and interfacial electronic properties is required. Image potential states (IPS) reside within a few Ångstroms of the surface, making them an ideal probe of surface and interfacial electronic structure. Image potential states are delocalized nearly free electron states parallel to the interface. They disperse parabolically as a function of wave vector parallel to the surface, $k_{||}$. Changes in the substrate or in any adsorbate will change the IPS electronic wavefunctions normal to the interface and influence the electronic binding energies and lifetimes. Parallel to the surface, interactions with the substrate and adsorbate will be manifested in the effective mass and in the $k_{||}$ resolved lifetimes.

One system that is of particular interest is a self assembled monolayer (SAM) chemisorbed onto a metal surface. Self assembled monolayers are of technological interest for their physical as well as electronic properties. They have been used to tune Schottky barriers, as molecular wires, and as rectifying layers [10–13]. Scanning tunnelling microscopy, electrochemical and other experimental techniques along with theoretical studies have elucidated the molecular electronic properties of SAMs. The parallel momentum, energy and lifetime information of specific electronic states available through the use of TPPE has only recently been used to investigate these systems [14–16].

Another system of interest is an adsorbate layer consisting of polar molecules. The

charge dipole interaction is stronger than that between a charge and an a non-polar layer. Within a polar adsorbate layer, this strong coupling of the charge to the layer can result in molecular motions that stabilize and solvate the electron. Compared to isotropic media, relatively little is known about the dynamics of electron solvation at metal/molecular interfaces where both the reduced dimensionality and hindered solvent motion result in dynamics distinct from those in the isotropic material [17–20]. Unlike electron solvation experiments in liquids [21–25], the state resolution available with TPPE allows the separation of the localization and the energy stabilization components of the solvation process. In addition to the energy resolution of TPPE, the temporal resolution is also important in order to monitor the time evolution of the solvation process.

Chapter 2

Background

Discussion of interfacial electronic structure should be grounded in the electronic structure of the substrate and an understanding of surface states. The substrate is the source of the electrons used in two photon photoemission, and thus its electronic structure will factor into the generation of the initial excited electron population. No bulk substrate electronic states are allowed at energies within the Ag(111) band gap. When probing electronic states at these energies, TPPE is a surface sensitive technique. One specific class of surface state important in this work is image potential states. The bulk band structure, surface states and image potential states will be discussed in detail in this chapter. The dissertation of W. Merry treats these subjects in greater depth than will be discussed here [26].

2.1 Substrate Electronic Structure

The bulk band structure of silver is shown in Figure 2.1 [27]. The energies of the bands are plotted as a function of wave vector ($\vec{k}$) for several high symmetry directions. The energy of a band as a function of $\vec{k}$ is referred to as the dispersion relation. In addition to the plotted bands, the vacuum level is also included and shows the silver workfunction of 4.56 eV. The d bands are located 4 to 8 eV below the Fermi level of silver, and are not accessible at the photon energies used in the experiments discussed in this dissertation. The s-p bands begin approximately 4.5 eV below the Fermi level and disperse upward from there. It is these bands that provide the initial state for most of the electrons used in this work. Though not plotted here, the density of states in the 0 to -4 eV range is determined only by the s-p bands and is fairly constant. This constant density of states reduces the variability of excitation population as a function of pump energy.

The bulk band structure is plotted between various points of high symmetry in the bulk Brillouin zone. The bulk Brillouin zone is depicted in Figure 2.2a. Of particular significance to the electronic structure of the (111) surface are the $\Gamma - L$, and $L - W$ directions. The $\Gamma - L$ in the bulk is along the ¡111¿ direction and projects onto the center of the surface Brillouin zone, $\bar{\Gamma}$. The surface Brillouin zone is shown in Figure 2.2b. The $\bar{\Gamma} - \bar{K}$ direction in the surface Brillouin zone is parallel to the $L - W$ direction in the bulk. Momentum parallel to the surface ($k_{||}$) is most influenced by the bulk band structure along this direction.

By projecting the bulk band structure onto the (111) surface, the resulting band structure is greatly simplified. The projected bulk band structure (PBBS) is plotted in

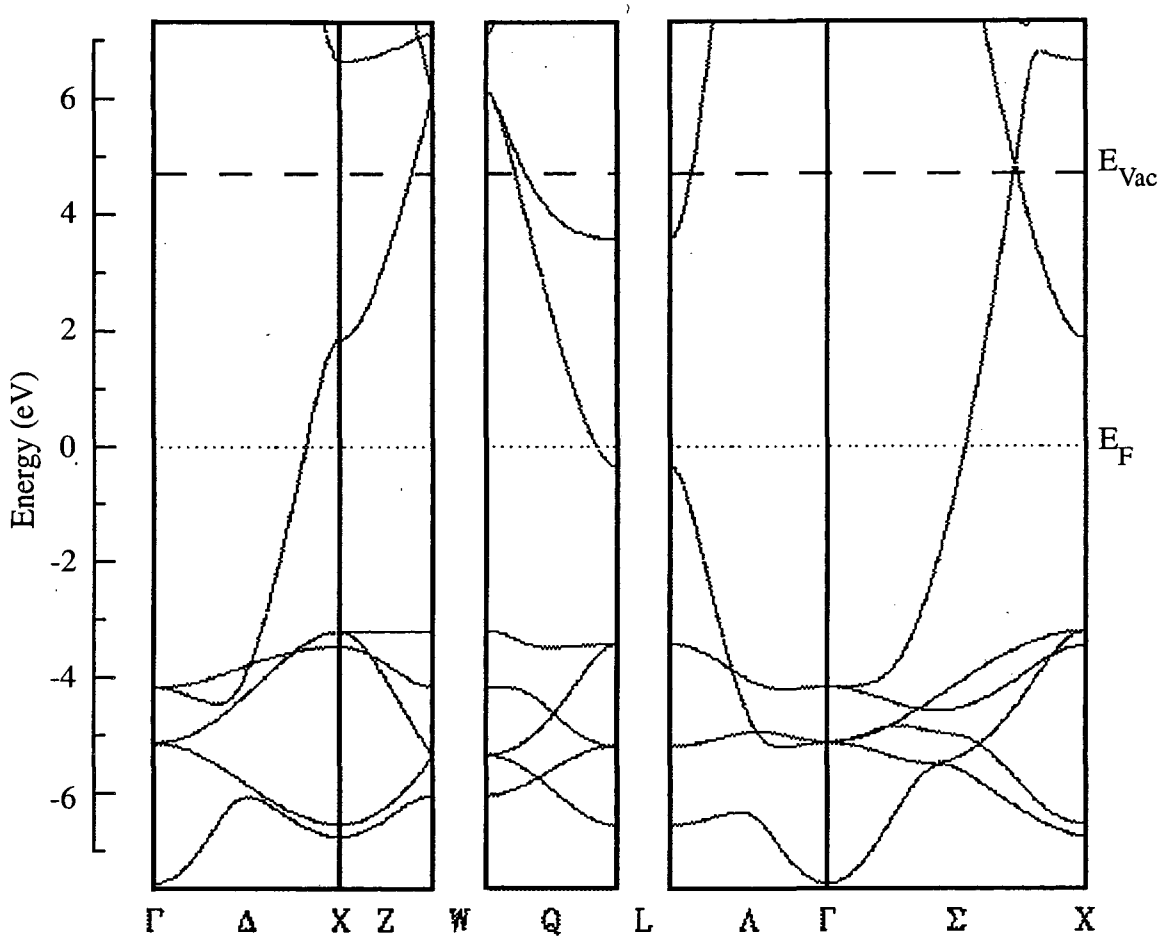

Figure 2.1: The silver bulk band structure.

a)

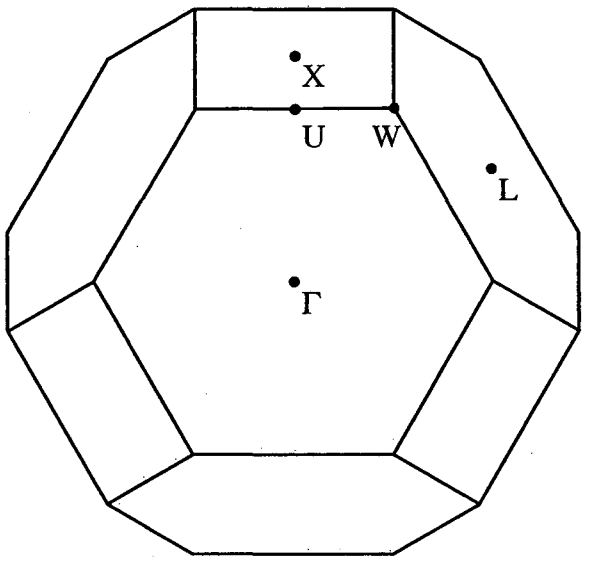

b)

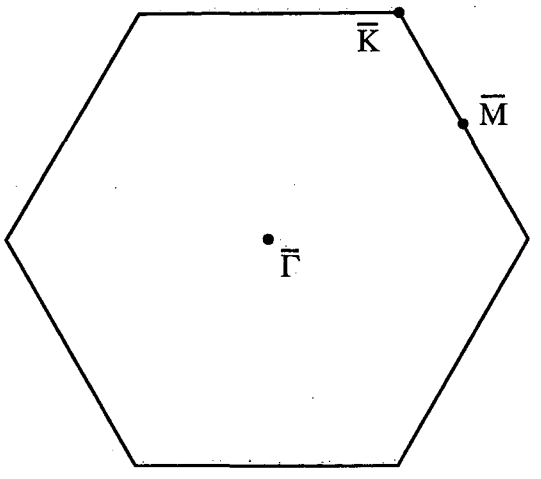

Figure 2.2: The silver bulk Brillouin zone and the surface Brillouin zone for the (111) surface of silver.

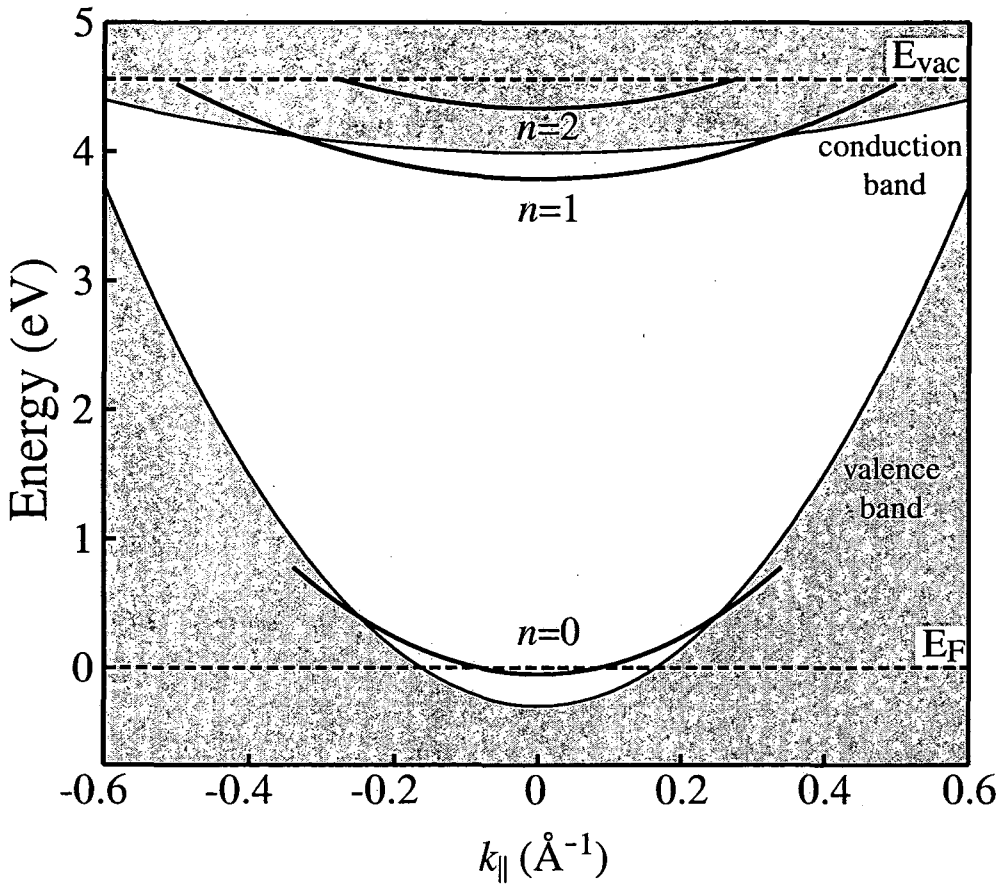

Figure 2.3: The projection of the silver bulk band structure onto the (111) surface. Included in the plot are the n=1 and n=2 image potential states and the surface state. At the $\bar{\Gamma}$ point ($k_{\|} = 0$), the valence is 0.3 eV and the surface state is 0.12 eV below the fermi level.

Figure 2.3. Since the PBBS is the projection onto the surface the energy bands are plotted as a function of $k_{\|}$. In the PBBS, below the valence band edge and above the conduction band edge are allowed electronic states of the bulk. At the $\bar{\Gamma}$ point in the center of the PBBS, the valence band edge is below the Fermi energy and the conduction band edge is 3.85 eV above the Fermi energy. This places the conduction band 0.71 eV below the vacuum level for the (111) surface. The gap is s-p inverted, with states at the top (bottom) of the gap possessing s-type (p-type) symmetry.

As can be seen in Figure 2.3, the energy of the bands increases parabolically as a function of $k_{||}$. An electron that is delocalized parallel to the surface can be approximated as a plane wave with energy

$$E(k_{||}) = \frac{\hbar^2 {k_{||}}^2}{2m_e}, \tag{2.1}$$

where m_e is the mass of a free electron, and $\hbar = \frac{h}{2\pi}$ where h is Plank's constant. In reality, there is a small periodic potential which perturbs the motion of the electron along the surface parallel. As a result of this potential, the electrons can be thought of as quasiparticles with a renormalized "effective mass", m^*. This effective mass will replace the free electron mass in Equation 2.1 to correct the energies for the parallel interaction of the electron with the surface. Equation 2.1 accounts for the parabolic dispersions, with the effective mass used as a parameter to describe the curvature. Nearly free electrons have an $m^* \approx m_e$, whereas localized electrons such as polarons have an $m^* \gg m_e$. A localized electron would have an energy independent of $k_{||}$. Within the tight binding model, m^* is related to the overlap of electronic wavefunctions on neighboring sites. A large overlap results in a dispersive electron with a small effective mass. A small overlap would result in a large effective mass.

2.2 Surface States

There are several types of surface states that bear discussion for the rest of this dissertation. Two different examples are plotted as lines in Figure 2.3. The $n = 1$ and $n = 2$ states at the top of the gap are image potential states, which result from an induced polarization of the substrate. These states comprise the primary states discussed in this

dissertation. The $n = 0$ state is an initially occupied crystal induced surface state. Crystal induced surface states result from the loss of the periodicity as the bulk is terminated at the surface. As with the bulk electronic structure, the occupied Ag(111) surface state is of primary concern as a state from which electrons can be excited. The $n = 0$ label is due to the ability of multiple reflection theory to obtain it as a solution in addition to the image potential states. An excellent source for the history and theories used to describe surface states is a book by Davison and Stęślicka [28]. The third type of surface state results from the electronic structure of an adsorbate. These states are only surface specific due to the two dimensional nature of the adsorbate.

2.2.1 Image Potential States

An electron outside of a conductive surface induces a polarization in that surface. The potential due to this polarization can be determined by the method of images [29]. The method of images is called such because it calculates the potential of a different problem, where there is an positive image charge the same distance behind the plane of the surface as the electron is in front of the plane. This charge configuration, depicted in Figure 2.4a, has a simple solution and satisfies the same boundary conditions as the electron outside of a conductive surface. Since the boundary conditions determine a unique potential, the Coulomb potential due to the image charge configuration ,

$$V = -\frac{q^2}{16\pi\epsilon_0 z}, \tag{2.2}$$

is the same as the potential outside of the surface due to the induced polarization.

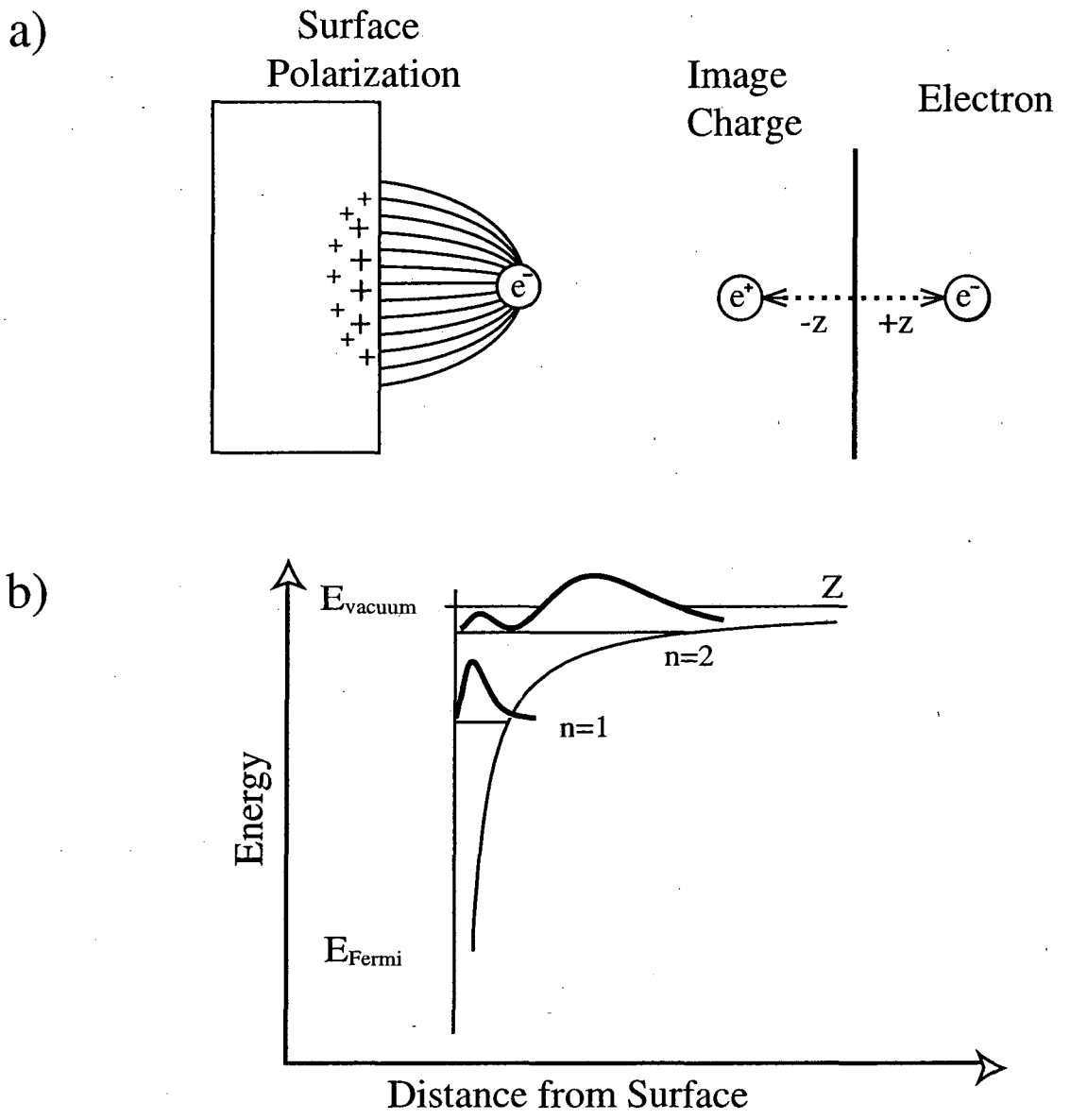

Figure 2.4: a) An electron near a surface induces a polarization in that surface. This results in a potential equivalent to the one produced by an opposite image charge behind the surface. b) The potential due to the image charge configuration, including the first two image potential states.

The image potential has the same form as the radial potential of the hydrogen atom. Similar to the hydrogen atom, the potential supports a series of Rydberg-like bound states which converge to the vacuum. These states are referred to as the image potential states (IPS). The first two IPS and the potential which supports them are depicted in Figure 2.4b. These states are bound close to the surface, with expectation values of 3 Å and 13 Å from the surface, respectively, which makes them sensitive to the changes and variations at the surface. The energies of the IPS are given by

$$E_n = -\frac{1}{16}\frac{m_e e^4}{2n^2\hbar^2} = -\frac{13.6}{16n^2}\,\mathrm{eV} = -\frac{0.85}{n^2}\,\mathrm{eV}, \tag{2.3}$$

where e is the elementary charge and n is the quantum number. These energies are exactly $\frac{1}{16}$ the value of the hydrogenic energies. This factor of 16 is due to the $2z$ distance dependance between the electron and the image charge and the fact that the electric fields only occur in the half space outside of the surface. The image potential is a one dimensional potential in the direction normal to the surface. The symmetry of the system results in a separability of the parallel and perpendicular components. The electron does not interact strongly with the substrate in the parallel direction, so the total energy is given as the sum of the parallel and perpendicular components (Equations 2.3 and 2.1)

$$E_{total} = E_n + \frac{\hbar^2 k_{\parallel}^2}{2m*}, \tag{2.4}$$

where the use of the effective mass accounts for the parallel interaction. In the perpendicular direction, the substrate electronic structure also influences the IPS electrons. This influence is due to the penetration of the IPS wavefunction into the metal. This interaction between

the IPS electron and the substrate electronic structure can be taken into account using the multiple reflection theory.

Electrons in the image potential were first observed experimentally outside of a liquid He surface [30]. Later, inverse photoemission spectroscopy was used to study IPS electrons outside of metal surfaces [31–34]. Two photon photoemission (TPPE) was used to observe IPS electrons with better resolution than inverse photoemission [35]. Using TPPE, both the n=1 and n=2 states could be observed. TPPE investigations of IPS electrons on both Ag(100) and Ag(111) have been compared with multiple reflection theory predictions [36, 37]. The experimental and theoretical results of binding energies and effective masses agree very well.

Multiple Reflection Theory

Multiple reflection theory (MRT) accounts for the influence of the substrate electronic structure on the image states [38–41]. The surface state electrons are treated as if their wavefunctions were reflecting back and forth between two barriers, the image potential barrier and the barrier for penetration into the substrate. This approximation is only useful when the IPS energies are in the band gap, otherwise there is no barrier at the surface. Bound states only occur when the phase accumulated over the course of a round trip $(\Phi_c + \Phi_b)$ is equal to $2\pi n$, where n is an integer. An expression for the phase for reflection from the image potential barrier can be obtained by using the WKB approximation. This results in the following expression,

$$\Phi_b = \left(\sqrt{\frac{3.4\,\mathrm{eV}}{E}} - 1\right)\pi, \tag{2.5}$$

where E is the binding energy of the electron with respect to the vacuum energy. For adsorbate covered surfaces, Φ_b can be obtained by integrating the Schrödinger Equation through a potential specified for the adsorbate layer and the vacuum beyond the layer.

By substituting Equation 2.5 into the phase matching condition, a more appropriate form of Equation 2.3 is obtained,

$$E_n = -\frac{0.85\,\mathrm{eV}}{(n+a)^2}, \tag{2.6}$$

where a is the quantum defect parameter and accounts for the influence of the substrate on the IPS binding energies. The quantum defect parameter is related to the crystal phase shift, ϕ_c by

$$a = \frac{1}{2}\left(1 - \frac{\Phi_c}{\pi}\right). \tag{2.7}$$

The use of this quantum defect parameter assumes that ϕ_c does not change over the range of energies spanned by the IPS.

Like a Rydberg series in the hydrogen atom, the IPS quantum number n in Equation 2.6 takes on values $n \geq 1$. Use of the value n=0, however, will still obtain a bound state corresponding to the crystal induced surface state for the Ag(111) band gap. For this reason, the crystal surface state, though not an image potential state, is often referred to as the n=0 state.

The two band nearly free electron model can be used to obtain Φ_c. The electron energies, ε, are given by solving the secular determinant

$$\begin{vmatrix} \frac{\hbar^2 k^2}{2m^*} - \varepsilon & V_g \\ V_g & \frac{\hbar^2 (k-g)^2}{2m^*} - \varepsilon \end{vmatrix} = 0 \tag{2.8}$$

where V_g, the perturbation due to the crystal ion core potential, is half of the energy of the band gap, k is the wave vector and g is the reciprocal lattice vector. Within the gap, solutions require that the wave vector be a complex quantity, $k = p + iq$. The imaginary part of the wave vector results in a solution that decays exponentially into the metal. In the z direction, the wavefunction in the metal is given by,

$$\psi_c = e^{qz} \cos(pz + \delta), \tag{2.9}$$

with the components of the wavevector and the phase parameter δ defined as,

$$q = \sqrt{\hbar^2/2m_e}\left(\sqrt{[\varepsilon E_g + V_g^2]} - \varepsilon - E_g\right)^{1/2} \tag{2.10}$$

$$p = \frac{g_z}{2} \tag{2.11}$$

$$\delta = \frac{1}{2} \arcsin\left(-\frac{pq\hbar^2}{2m^* V_g}\right) \tag{2.12}$$

The energies and effective masses of the valence and conduction bands as well as the lattice spacing of the metal are the important variables in these calculations. The wavefunction in the metal is matched with a plane wave (with wave vector κ) in the vacuum resulting in a phase shift expression for reflection from the surface,

$$\Phi_c = 2\arctan\left(\frac{p}{\kappa}\tan\left[pz+\delta\right]-\frac{q}{\kappa}\right). \tag{2.13}$$

With this Equation, the energies of the IPS electrons can be calculated as a function of substrate electronic properties. For a s-p inverted gap, such as the one present at the Ag(111) surface, Φ_c ranges from 0 at the bottom of the gap to π at the top of the gap. The possible values of the quantum defect given by Equation 2.7 are between 0 and $\frac{1}{2}$, with $n = 1$ IPS energies ranging from 0.85 eV at the top of the gap to 0.38 eV at the bottom. For the Ag(111) surface, the vacuum level is in the conduction band placing the $n = 1$ IPS close to the top of the band gap and resulting in a calculated binding energy of 0.76 eV, which is within error of the experimentally determined value of 0.77 eV [42].

Image Potential State Lifetimes

Lifetimes of IPS electrons can be measured using time resolved TPPE. Lifetimes for the n=1 and n=2 IPS electrons on Ag(111) and Ag(100) have been measured by Schoenlein and coworkers [43–45]. Lifetimes of electrons with $k_{||} = 0$ are primarily due to decay into the substrate. This main pathway is assumed to be via electron-electron scattering and the creation of electron hole-pairs in the metal. This type of a process results in a lifetime that is proportional to the overlap of the excited electron's wavefunction with the metal [46]. The wavefunctions calculated using Equation 2.9 in the metal matched with a hydrogenic wavefunction in the vacuum can be used. Thus a multiple reflection theory calculation can be used to obtain lifetime information for the respective surface states. More complex theoretical models can be used for clean metal surfaces, with accurate calculations for lifetimes and linewidths [47, 48]. The influence of the crystal induced surface state on

the IPS lifetimes has also been calculated [49]. Relative to the (100) surface, the linewidth of the (111) surface is increased by the presence of the surface state. This effect is offset, however, by the presence of the Fermi level in the band gap.

In addition to the reproduction of clean surface results, the MRT formalism can be used to obtain the lifetimes of image potential states on adsorbate covered surfaces. On these surfaces, the IPS wavefunction is calculated starting with Equation 2.9 at a specific energy and propagating the Schrödinger Equation through the potentials in the adsorbate and the vacuum. Calculations that result in wavefunctions that do not blow up as $z \rightarrow \infty$ give the bound states. These wavefunctions are then normalized and the magnitude of the overlap with the substrate can then be determined.

To calculate the lifetimes of IPS electrons at adsorbate covered surfaces, the potentials in the adsorbate and in the vacuum are needed. The potential in the vacuum was first derived by Cole [50]. A dielectric continuum model has been successfully used for this purpose. Within this approximation, the adsorbate is modelled as a simple dielectric. The dielectric constant, electron affinity and layer thickness represent the main parameters of the model. The model potentials obtained from this approach will be discussed in more detail in chapter 4. The lifetimes for IPS at interfaces formed by xenon and n-alkane adsorbates have been accurately calculated using the dielectric continuum model [51–58]. Repulsive electron affinities push the electron out into the vacuum, decouple it from the metal and result in longer lifetimes [53–55, 59]. Attractive electron affinities allow the electron to enter the layer and thus do not have as extreme of an effect on the lifetime [56–58, 60, 61].

2.2.2 Adsorbate Electronic States

The final category of surface states of concern to this dissertation are adsorbate induced electronic states. Unlike the crystal and image potential surface states, these states are not true surface states, but rather atomic and molecular electronic states confined to the surface along with the adsorbate. If the adsorbate layer thickness were increased, these states should become the electronic states of molecular crystals. This transition in the parallel direction should occur as a function of increased coverage up to a monolayer. In the direction normal to the surface, this transition should occur as the thickness of the layer is increased. In the quantum well formation from IPS electrons at a xenon/Ag(111) surface, the energies and effective mass of the electron parallel to the surface approached the values of crystalline xenon affinity level as the number of xenon layers was increased. The most important electronic states for technological purposes are the valence and conduction bands, and their molecular orbital counterparts, the HOMO and LUMO. These states are experimentally accessed as the ionization potential and the electron affinity level.

Most of the investigations of excited adsorbate electronic states study adsorbed metal atoms and the corresponding electronic structure. Petek and coworkers were able to populate a dissociative electronic state of Cs adsorbate atoms and observe the initial stages of the desorption process [62, 63]. Studies of alkali metal adsorbates have monitored the coverage dependant shifting of the unoccupied electronic states and a non-metal to metal transition [64, 65]. Photoemission experiments of Hg on Ag(100) have investigated both the parallel and perpendicular evolution of the Hg electronic structure [66]. The parallel electronic structure of CO on Ag(111) was compared to that of N_2 on graphite, and

structural information about the CO adsorption geometry was deduced.

Chapter 3

Experimental

3.1 Two Photon Photoemission

Angle resolved photoemission is a common technique used to study the occupied electronic bands of solids and surfaces [67]. In order to eject electrons, the photon energy is greater than the workfunction of the metal. The states probed are the occupied electronic states below the Fermi energy. Regular photoemission can not provide any information about the unoccupied electronic structure. Two photon photoemission is a pump probe technique that can access the unoccupied electronic levels of solids and interfaces. There are several excellent reviews of electron dynamics at surfaces and of TPPE [68–71].

The TPPE experiment is depicted in Figure 3.1. The first photon excites an electron from below the Fermi energy into an intermediate state. At energies in the band gap, these intermediate states are surface states. The second photon then photoemits the electron from the intermediate state into the vacuum. The kinetic energy of the electron is measured via time of flight analysis. The binding energies of the intermediate states can

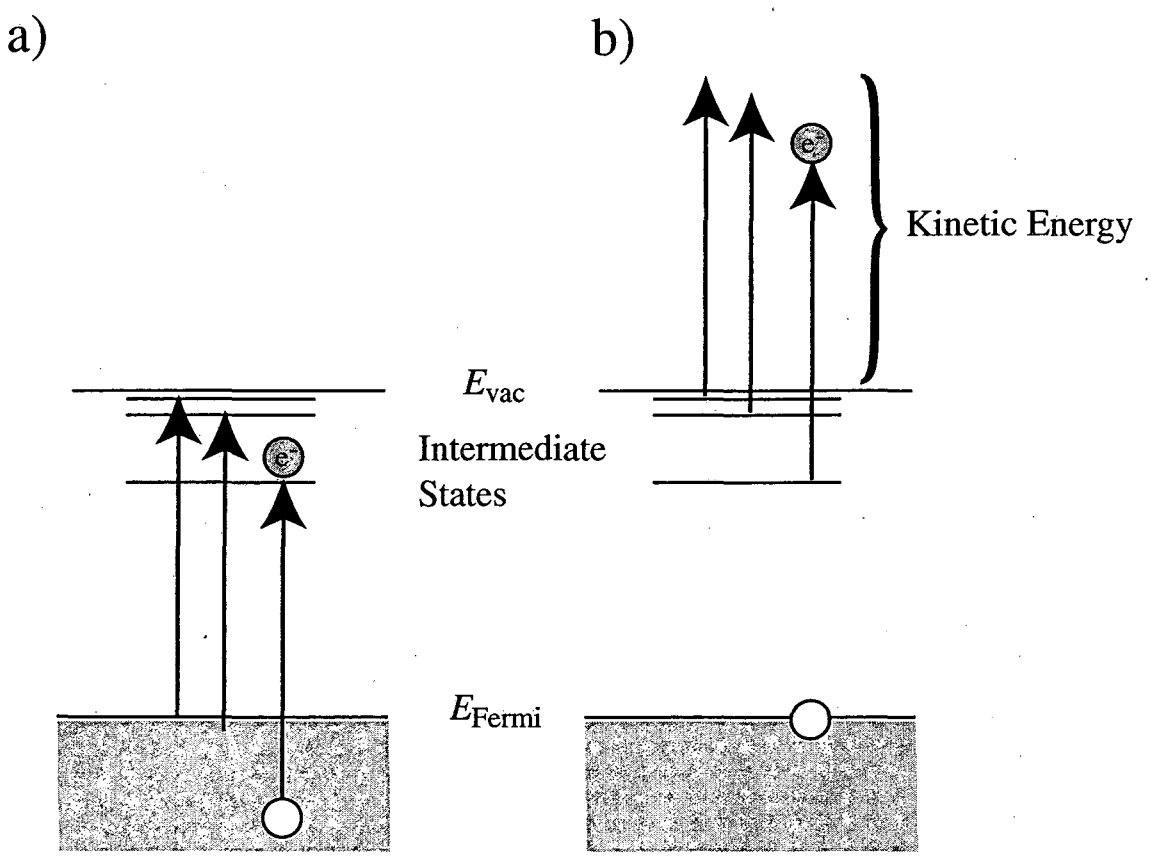

Figure 3.1: (a) Photons with energy less than the workfunction populate excited electronic states. (b) At a later time, t, a second photon photoemits the electron into the vacuum. The kinetic energy of the electron in the vacuum is the difference between the probe photon energy and binding energy of the excited electronic state.

be determined by subtracting the excess (kinetic) energy of the electron from the photon energy of the second pulse. An electron from an occupied state below the Fermi energy can also be observed with TPPE. In this case the electron simultaneously absorbs two photons and is photoemitted.

The wavelength dependance of the photoemitted electron kinetic energies can be used to distinguish between initially occupied electronic states and initially unoccupied intermediate states. This is schematically depicted in Figure 3.2. In Figure 3.2a an initially

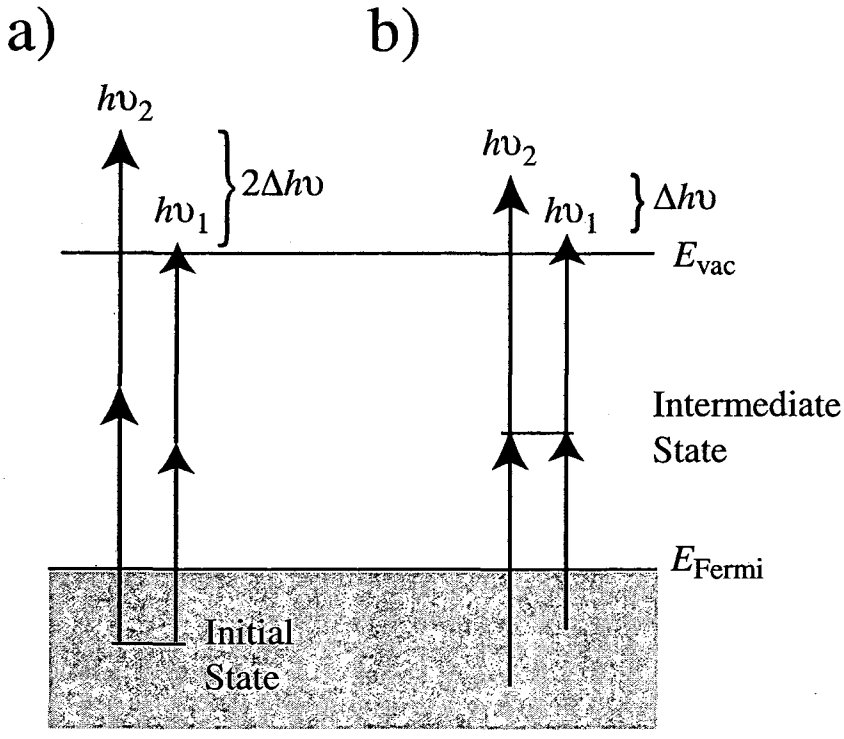

Figure 3.2: Schematic description of a monochromatic TPPE wavelength experiment. (a)Photoemission from an initially occupied state. The kinetic energy of the photoemitted electron changes by twice the change in photon energy ($2\Delta h\nu = 2(h\nu_2 - h\nu_1)$). (b)Photoemission from an intermediate state. The electron kinetic energy changes by the same amount as the photon energy ($\Delta h\nu = h\nu_2 - h\nu_1$).

occupied state is photoemitted at two different wavelengths. The change in kinetic energy is twice the change in photon energy due to the absorption of two photons. Figure 3.2b shows the same process for an intermediate state. As it only takes one photon to photoemit from the intermediate state, the change in kinetic energy is equal to the change in photon energy.

3.1.1 Time Resolved Two Photon Photoemission

In addition to its ability to access both occupied and initially unoccupied electronic states, TPPE can also provide a direct measure of the electron dynamics of the unoccupied

electrons. Time resolution is obtained by temporally delaying the probe pulse with respect to the pump pulse. The intensity of the photoemitted electron signal as a function of time reveals the dynamic behavior of the electrons bound in the intermediate state. The lifetime information is also present in the linewidths of the detected peaks. This information can be difficult to extract, however, as the inhomogeneity of the system and the dephasing time for both population and photoemission transitions contribute to the lineshape. These effects are treated in more detail in the dissertation of C.M. Wong [60]. Petek and coworkers have used interferometric time resolved TPPE to experimentally address dephasing and decoherence issues [63, 72–75].

TPPE has been used as a probe of hot electrons in both noble metals [76–78] and semiconductors [79, 80]. Spin dependent lifetimes have been measured at a magnetic Co surface [81]. The dynamics of electron transfer from a delocalized to a localized polaron electronic state have also been measured [53, 55]. The influence of xenon quantum well formation on IPS lifetimes has been observed with TPPE [56, 82].

3.1.2 Angle Resolved Two Photon Photoemission

For photoemission from a reflective surface, the parallel component of the electric field is cancelled out, thus only the wavefunction along the surface normal is coupled to the electronic state of the free electron in the vacuum. As a result of the cancelling of the parallel components of the electric fields, the parallel wavefunction of the electron must be the same before and after the photoemission process. This results in a conservation of $k_{||}$. For photoemission from bulk states, different values of $k_{\perp}$ are accessed at different wavelengths. This appears in the photoemission spectra as a peak whose energy shifts with

respect to the Fermi level as a function of wavelength. In this manner the perpendicular electronic bands can be mapped. For electronic states localized in the normal direction (surface states) $k_\perp$ is not a good quantum number, and variations in wavelength do not influence the peak position with respect to the Fermi level.

The parallel dispersions can be obtained by measuring the electron kinetic energy as a function of angle between the sample normal and the detector. This is depicted in Figure 3.3. The parallel wavevector is determined by the geometry of the system (Figure 3.3a) and is given by

$$k_{||} = \sqrt{\frac{2m_e E_{kin}}{\hbar^2}} \sin\theta. \tag{3.1}$$

The specific value of $k_{||}$ is dependant on the kinetic energy of the electron and the rotation of the sample with respect to normal. The highest $k_{||}$ states that can be probed are determined by the maximum rotation of the sample and the highest energy photon that can be used to photoemit electrons from a given state. In these TPPE experiments, the photon energy is limited by the workfunction of the sample to avoid overloading the detector with single photon photoemitted electrons and ruining the signal. This limits the kinetic energy of the electrons and how far the dispersions can be probed in $k_{||}$. The relation between the electronic energy and parallel wavevector obtained from Equation 3.1 can be fit using Equation 2.4 to obtain the effective mass of the electronic state. Experimental measurements of the dispersion have observed electrons localized at stepped surfaces, but delocalized along the steps [83]. The scattering of electrons moving parallel to the surface can also be determined by measuring the lifetimes of the electrons as a function of $k_{||}$ [60,82].

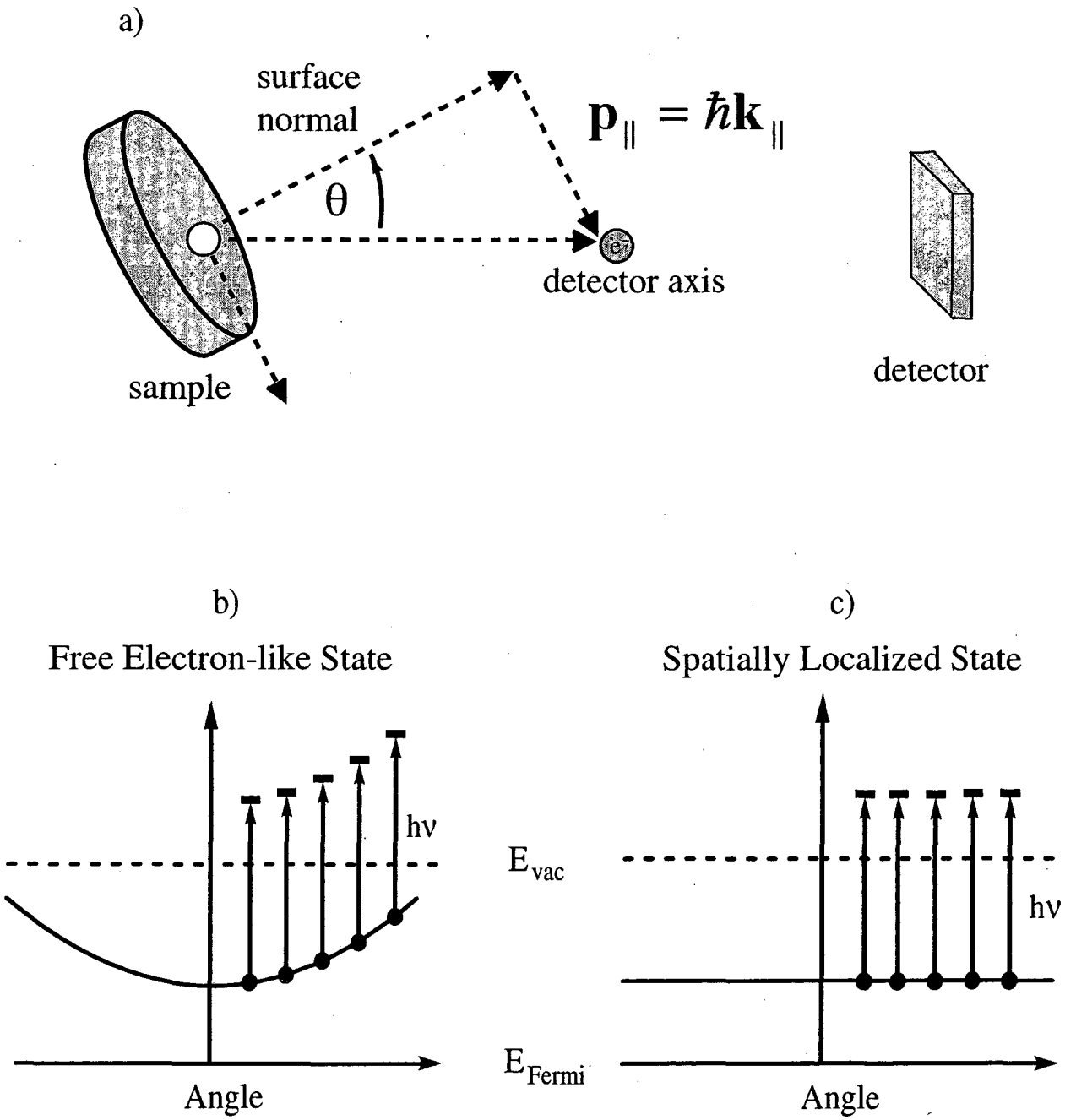

Figure 3.3: (a) With the sample at an angle, θ, with respect to the detector, an electron has to have momentum parallel to the surface, $P_{\parallel}$,in order to be photoemitted in the direction of the detector. (b) A delocalized electron with a free electron like dispersion. The kinetic energy of the photoemitted electron increases parabolically with $k_{\parallel}$. (c) The kinetic energy of a localized electron is independent of angle.

3.2 Experimental Apparatus

There are two major components necessary to conduct TPPE experiments, the laser and the vacuum chamber for the sample. The vacuum chamber, electron detection and data acquisition equipment are described in the dissertations of W. Merry and J.D. McNeill [26,61]. The laser used in these experiments was a Ti:sapphire regenerative amplifier seeded by a Ti:sapphire oscillator, both of which were pumped by an argon ion laser. An optical parametric amplifier was used to convert the pulses from the Ti:Sapphire laser system into a variety of wavelengths used in the TPPE experiments. This system is depicted in Figure 3.4.

A Coherent Innova 425 sealed mirror argon ion laser was used to pump the system. A current of approximately 48 Amps at 500 V produced 22W of visible light at multiple frequencies. About 8 W of this light was used to pump the Ti:Sapphire oscillator, the remaining 14 W were used to pump the regenerative amplifier.

The wavelength at which the Coherent Mira 900-F oscillator lases is determined by a birefringent filter in the beam cavity. With the use of a Ti:sapphire gain medium, the theoretical wavelength range is from 710nm to 1000nm. In practice this would require a different set of optics and changes in the cavity geometry. The actual wavelength range of the oscillator is from about 780 nm to 815 nm. Under normal conditions the laser is aligned for operation at 800 nm with a bandwidth of 10nm FWHM. When modelocked, the laser produces pulses with a 150 fs duration at a repetition rate of 76 MHz. Only about 350 mW of the 1.1 W output power is passed on to the amplifier.

The Coherent RegA 9000 picks out 200-250 kHz of the oscillator output to amplify.

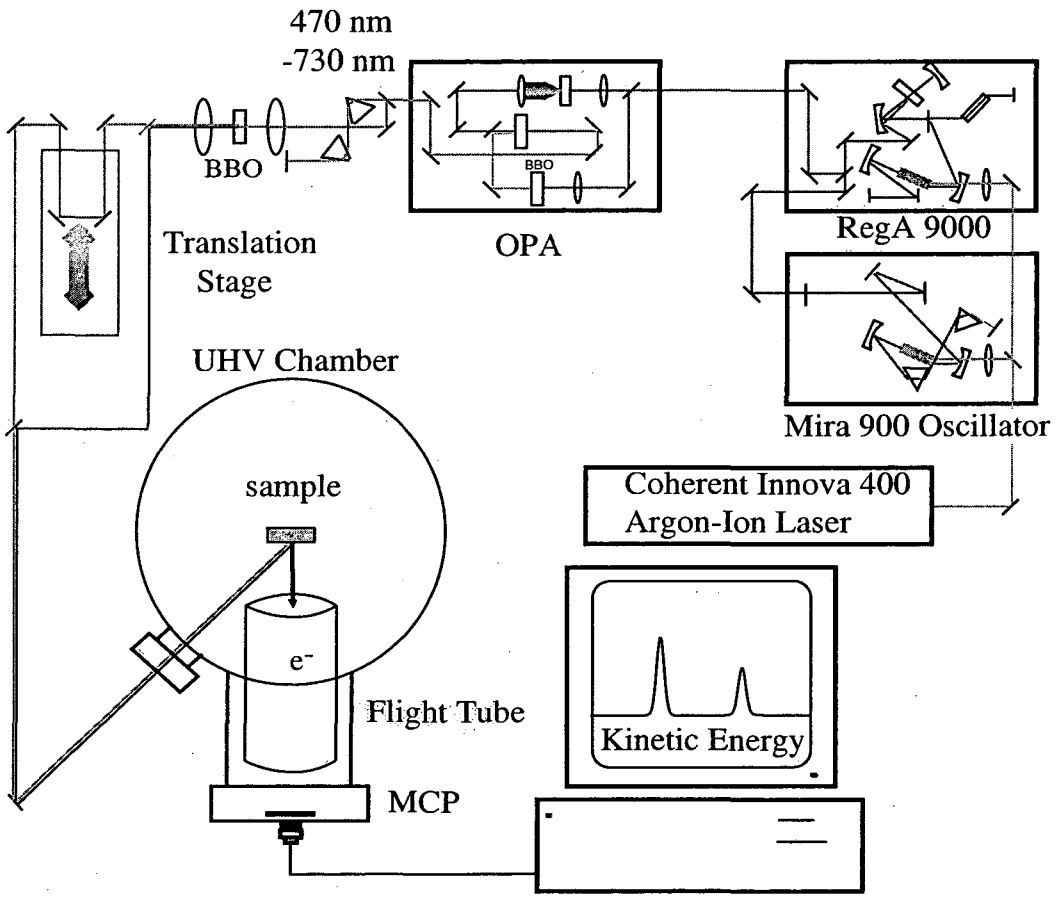

Figure 3.4: Depiction of the TPPE apparatus used to obtain the data reported in this dissertation.

The cavity dumper injects the pulses into the cavity where they undergo 22-25 round trips. The pulses are amplified with each pass through the Ti:sapphire crystal. The amplified pulse in then ejected from the cavity with the cavity dumper. A Q-switch in the cavity maximizes the population inversion in the gain medium by allowing lasing only when the pulse is being amplified and also stretches the pulses. After ejection from the cavity, a holographic grating is used to recompress the pulses, resulting in pulse widths of approximately 260fs.

The light from the RegA is passed to the Coherent OPA 9400. Half of the light is frequency doubled to generate the 400 nm second harmonic. The other half of the light is focused into a sapphire crystal to generate a white light continuum. These two beams are mixed in a Barium Borate (BBO) crystal, where part of the white light is parametrically amplified by the 400 nm light. The specific wavelength amplified is determined by rotation of the BBO crystal. This wavelength can range from 470 nm to 730 nm. The output from the OPA is compressed in a pair of prisms. The pulse width is wavelength dependant, with 60-80 fs pulses around 720 nm and pulses as long as 130 fs around 530 nm. The power output is also dependent on the wavelength, with powers of 25-30 mW common around 700 nm and powers of less than 2 mW below 500 nm. After compression, the light is frequency doubled in another BBO crystal to generate the ultraviolet pump wavelengths.

In the experiments discussed in the next chapter, ultraviolet light obtained from doubling light around 800 nm was used. Two different approaches were used to obtain tunable light around 400 nm. The birefringent filter in the Mira could be used to tune the wavelengths in a narrow region about 800 nm. This light then bypassed the OPA and was frequency doubled. This approach was used for ultraviolet pump infrared probe

experiments in the narrow wavelength range around 800nm that could be accessed by tuning the Mira. Though infrared light between the OPA and Mira accessible wavelengths was not obtainable, the corresponding ultraviolet second harmonic of these wavelengths was obtained via a second method. This method focused all of the power from the RegA into the sapphire crystal in the OPA. The resulting white light was then doubled in a BBO crystal. Rotation of the crystal determined which portion of the spectra was frequency doubled. This resulted in accessible ultraviolet wavelengths between 370 and 400 nm.

3.3 Sample Preparation and Characterization

The Ag(111) sample was polished using standard techniques and mounted on a manipulator in an ultra high vacuum (UHV) chamber. The sample is wedged and able to rotate between -4 and 24 degrees for dispersion measurements along the $\bar{\Gamma}$ to $\bar{K}$ direction. The use of a UHV chamber is essential to ensure sample cleanliness over the course of an experiment. The silver sample was cleaned before each experiment by sputtering in argon at a temperature of 500 K and annealing at 725 K. Temperatures as low as 50 K could be reached by using liquid helium to cool a copper braid attached to the sample holder. Order and lack of contamination could be measured with low energy electron diffraction (LEED) and Auger spectroscopy. Additionally, the widths of the peaks observed with TPPE were sensitive to surface quality.

3.3.1 Thiolate Self Assembled Monolayers

To obtain the chemisorbed self assembled monolayers, the sample was exposed to dialkyl-disulfide molecules, $(CH_3(CH_2)_nS)_2$. Upon interaction with a noble metal surface, the sulfur-sulfur bonds of disulfide molecules are cleaved and a strong sulfur-metal bond is formed, resulting in a monolayer of thiolate molecules, $(CH_3(CH_2)_nS-)$ [84, 85]. The thiolate molecules were adsorbed at 297K. The order and completion of the full layer was verified with LEED and the presence of sulfur was measured with Auger to ensure that the overlayers were indeed thiolate molecules. The Auger spectra is shown in Figure 3.5. After adsorption of the thiolate layer, the sample was cooled to 120 K. This improved the signal to noise ratio in the TPPE spectra. The coverage dependent data discussed in section 4.1 were taken at exposures of 1 L (Langmuir, 1 L $=10^{-6}$torr·seconds), 2.5 L and 4 L. At 4 L, LEED spots are observed, indicating an ordered overlayer. The electron diffraction pattern is consistent with the results previously observed for thiolates on Ag(111) [86]. The TPPE signal goes up as the exposure is increased until it is saturated at 4 L. After this point, increased exposure influences neither the number of photoemitted electrons detected nor the TPPE spectra of the thiolate covered surface. For these reasons, the 4L exposure will be referred to as the saturated monolayer.

Two different thiolate layers were used for the experiments described in this dissertation, methylthiolate (CH_3S) and butylthiolate $(CH_3(CH_2)_3S)$. The main difference between these two molecules is the length of the alkyl chain. The workfunction of the monolayers was determined by fitting the n=1-3 IPS progression to Equation 2.6. The difference between the measured and expected kinetic energies is the change in work function.

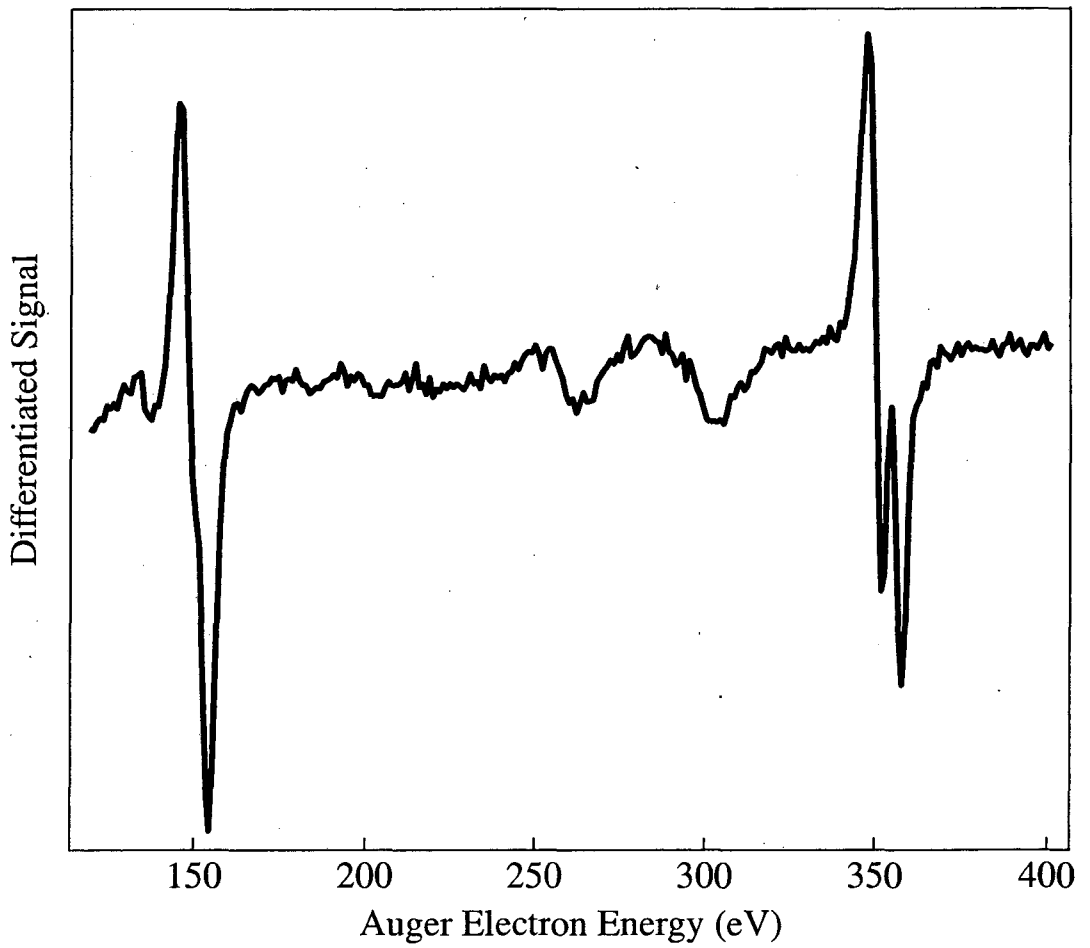

Figure 3.5: Auger electron spectra of a thiolate layer adsorbed onto Ag(111). The main silver peaks at 351 and 356, as well as at 260, 266, 301 and 304 eV are plainly apparent. The sulfur peak at 152 eV is also apparent. Signal from carbon atoms shows up at 268 eV is hidden beneath the silver peak at 266 eV.

A potential bias applied between the sample and detector is used to compensate for the contact potential. This potential is set to align the expected and measured kinetic energies. The methylthiolate workfunction was determined to be 3.2 eV. This energy corresponds to the double of a 775 nm photon. The higher energy photons available from the OPA are above the workfunction. This results in a lot of photoemitted electrons which may result in measurements of peak energies that are inaccurate, though the peak dynamics measured should not be affected. Using light from the RegA at 800nm, the energies and dispersions of the electronic states of these monolayers could be measured. The 260 fs pulse width from the RegA was too broad to time resolve the electron dynamics, so all dynamic data was collected using OPA light just above the workfunction.

Figure 3.6 shows two different spectra for butylthiolate/Ag(111). Both show the IPS progression, but the thiolate molecular electronic states discussed in section 4.1 are not present in Figure 3.6a. The thiolate electronic states were not consistently observed in any given adsorption of the butylthiolate monolayer. The methylthiolate monolayer did not have these problems. Both types of butylthiolate layers had the same LEED pattern and auger spectra. In an attempt to rule out surface order, the silver sample was sputtered, but not annealed. Both types of spectra were observed for layers adsorbed onto the rougher, unannealed surface. The difference was not attributable to a difference in coverage. Successive adsorption, sputtering/annealing and readsorption using the same disulfide sample and the same laser wavelength and power for the TPPE experiment resulted in observation of both types of spectra. Though a structural difference may be the reason for the two types of spectra observed, we were unable to determine that difference. This same incon-

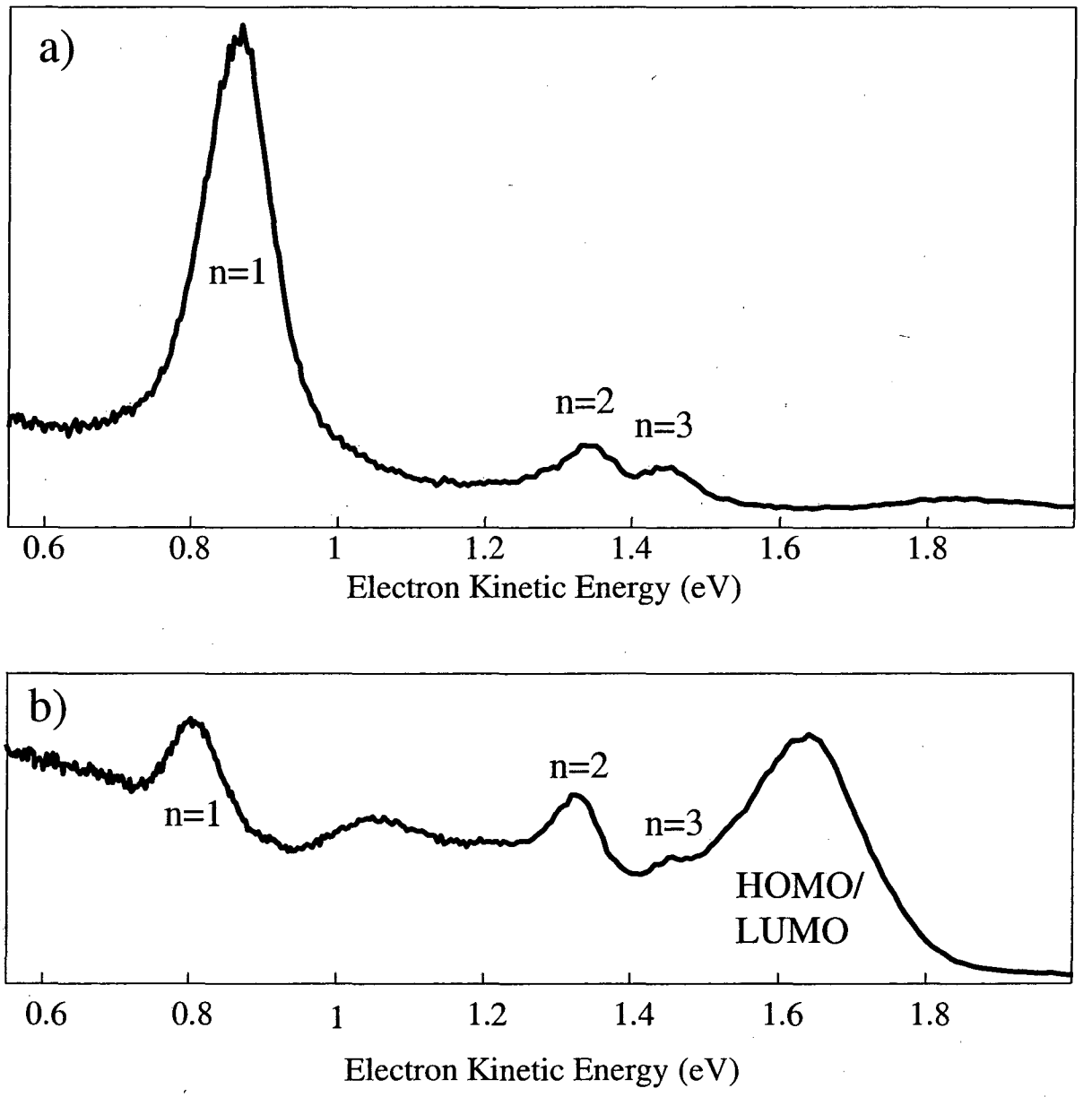

Figure 3.6: Spectra representative of the two different butylthiolate results. (a) Image potential state progression, but no adsorbate electronic states observed. (b) Both the IPS progression and the thiolate HOMO/LUMO observed

sistency in the observation of the thiolate electronic states was observed for ethanethiolate and propanethiolate as well as the butylthiolate. Only for the methylthiolate layers were the adsorbate electronic states observed on every occasion that the layers were dosed.

3.3.2 Polar Acetonitrile Molecular Layers

Acetonitrile molecules do not chemisorb to the silver surface, necessitating the use of cryogenic temperatures for physisorption of the layer. The kinetics of acetonitrile adsorption are complicated, being both temperature and pressure dependent. If the sample is exposed to pressures less than $\sim 4\text{x}10^{-8}$ Torr, no adsorption is observed. Molecules will adsorb onto the clean surface below 140 K, but quickly desorb unless the temperature is below 125 K. At higher pressures, the second layer will adsorb at 125 K, but doesn't remain until temperatures colder than $\sim$95 K are reached. The layer by layer adsorption of acetonitrile is monitored by TPPE, which produced distinctly different spectra for one and two layer coverages due to the differences in the workfunction and binding energies. Figure 3.7 shows the n=1 IPS spectra for several coverages of acetonitrile adsorbed on Ag(111). As the coverage is increased, the monolayer n=1 IPS is reduced in intensity and the two layer n=1 IPS intensity is increased. After the adsorption of a monolayer of acetonitrile, the workfunction decreased to 3.8 eV. The adsorption of a second layer increased the workfunction of the sample (relative to the monolayer) to 3.9 eV.

Low energy electron diffraction experiments of the acetonitrile/Ag(111) interface do not show any LEED spots, indicating the absence of long-range translational order. Similar conclusions have been drawn from LEED experiments of acetonitrile on Au(100) [87]and near edge x-ray absorption fine structure experiments for acetonitrile adsorbed

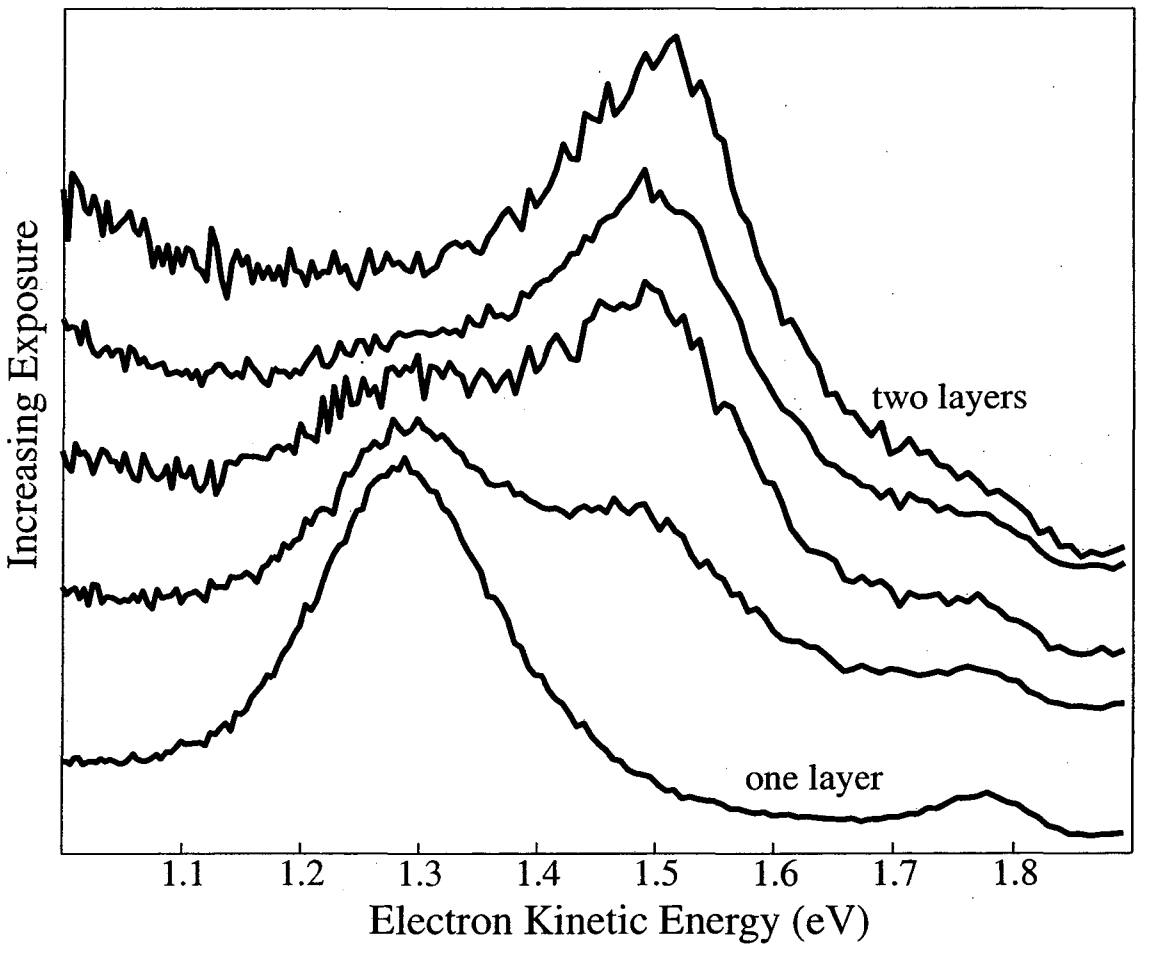

Figure 3.7: As the exposure is increased, the monolayer n=1 IPS decreases in intensity and the two layer n=1 IPS increases in intensity.

on Ag(110) and Au(100) [88, 89]. The x-ray experiments were able to conclude that the molecules adsorbed with their bond axis close to parallel to the surface, but with a random orientation in the azimuthal coordinate.

3.4 Workfunction

In chapter 5, the solvation phenomena observed for the polar acetonitrile layers adsorbed onto a Ag(111) crystal surface are explained as a dynamic change in the local workfunction. The local nature of the workfunction of an inhomogeneous surface is well known [90, 91]. In TPPE, the local workfunction is observed when partial layers adsorb in islands [70]. The different islands have different local workfunctions, and thus the IPS electrons photoemitted from the islands have kinetic energies different from electrons photoemitted from the underlaying substrate or layer. This effect can be observed in the adsorption of acetonitrile layers shown in Figure 3.7. This section will discuss the concept of a local workfunction and how the local workfunction influences the photoemitted electron.

3.4.1 Global Workfunction

The workfunction of metal with an infinite homogeneous surface is the energy required to remove an electron from the metal and place it infinitely far away from the surface. Thus the common conception of the workfunction is the difference between the Fermi energy and the vacuum energy. This picture of the workfunction is depicted in Figure 3.8a. There are two contributions to the workfunction, the difference in chemical

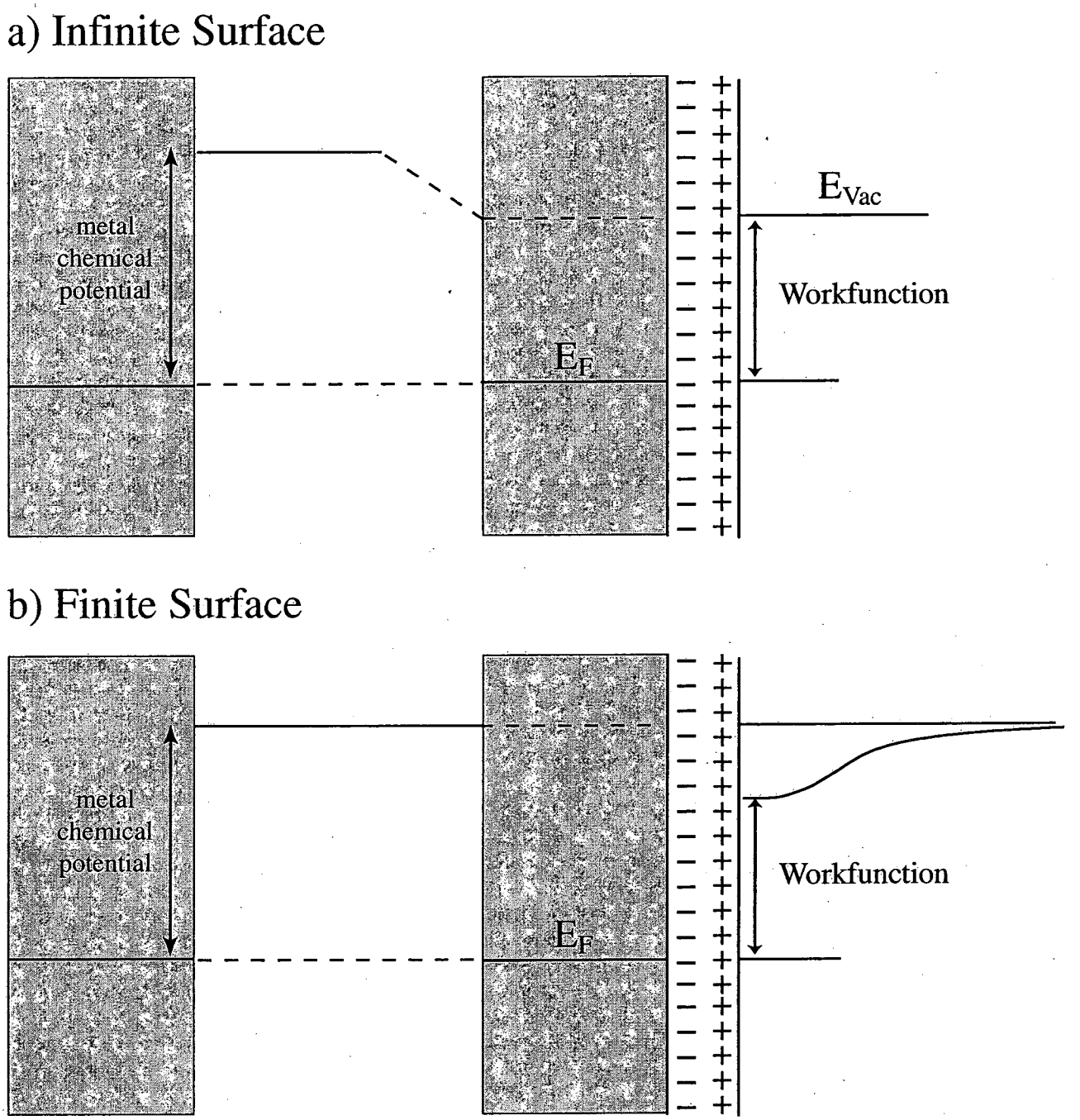

Figure 3.8: (a) The workfunction of an infinite surface is the difference between the Fermi energy and the vacuum energy. It results from the differences in chemical potential and the surface dipole. (b) for a finite surface, the workfunction has to be measured close to the surface.

potential for an electron in the metal versus an electron in the vacuum, and the surface potential that the electron must cross to reach the vacuum. It is the second contribution that is important within the context of this research, as changes to the surface via an adsorbate should not have much influence on the bulk chemical potential. The dipole layer depicted in Figure 3.8a is the opposite of what would be expected of a clean surface, but is consistent with the reoriented reoriented acetonitrile dipolar layer that is discussed in chapter 5.

The workfunction of a real metal with a finite surface is not defined as easily as it is for an infinite surface. The difference in chemical potential has not changed, but the fields outside of the surface are no longer simple. Even without the influence of detectors and other instruments in the vacuum chamber with a real sample, the above definition has problems. Infinitely far away from a finite surface, the potential due to the dipole at the surface goes to zero. Using the above definition for the infinite surface would leave out the contribution of the surface dipole, resulting in a workfunction that only depended on the difference in chemical potentials between the bulk metal and the vacuum. This would result in a workfunction that is independent of crystallographic orientation and insensitive to the adsorption of thin layers. This is obviously incorrect and must be accounted for.

A better definition of the workfunction would be the difference between the potential in the metal and the potential just outside of the surface due to the surface dipole. This picture of the workfunction is depicted in Figure 3.8b. The potential in the z direction just outside the surface can be broken up into two components,

$$V(z) = V_{IP}(z) + V_{dip}(z), \tag{3.2}$$

where $V_{IP}(z)$ is the image potential induced by the presence of the electron and $V_{dip}(z)$ is the static potential at the surface. The $V_{dip}(z)$ component is due to the electronic structure of the adsorbate and the inherent surface dipole as modified by the adsorbate. In the case of a polar adsorbate, $V_{dip}(z)$ includes the projection of the molecular dipole onto the surface normal and is thus strongly influenced by the adsorption geometry of the adsorbate. It is with reference to this dipolar surface potential that the workfunction of a finite surface is defined.

With the workfunction defined close to the surface, the behavior of the electron as it leaves the surface becomes important. The electron's kinetic energy will change as it traverses the potential in the z-direction. This behavior is depicted in Figure 3.9a, and results in an electron kinetic energy at the detector that is different than the kinetic energy of the initially photoemitted electron. The potential between the sample and the electron detector is due to two contributions, the local nature of any real workfunction and a contact potential due to the workfunction difference between the sample and detector. For accurate photoemission measurements, a bias potential is applied to compensate for both of these contributions. This is depicted in Figure 3.9b for the flight time energy measurements used in these experiments. The detector and the flight tube, which ensures that the kinetic energy of the photoemitted electron is constant through the majority of the flight path, is floated at a potential bias. The bias ensures that the electron has the correct kinetic energy when entering the flight tube.

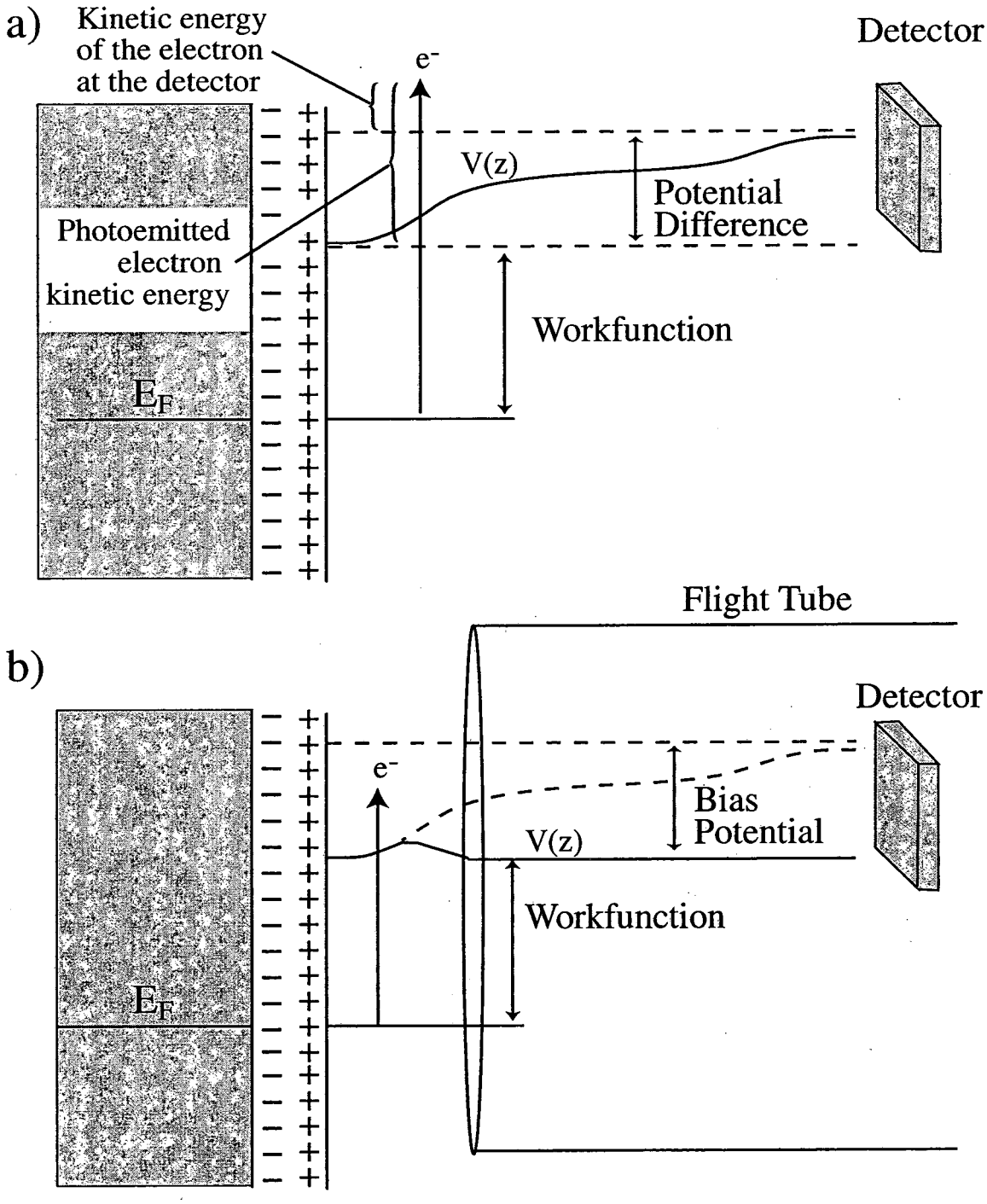

Figure 3.9: (a) The kinetic energy of the photoemitted electron is changed as the electron traverses the $V(z)$ between the sample and detector. (b) The potential bias applied to the flight tube compensates for the contact potential, resulting in a field free flight path that does not alter the kinetic energy of the electron.

In the TPPE experiments, the workfunction of the sample is determined by fitting an IPS progression to Equation 2.6 to obtain the binding energies. These binding energies are subtracted from the photon energy to obtain the expected kinetic energies of the photoemitted IPS electrons. The bias potential applied to the flight tube is then adjusted to obtain these kinetic energies. An incorrect bias potential will either accelerate or decelerate the photoemitted electrons and change the measured kinetic energies of the electrons.

3.4.2 Local Workfunction

In the definition of the workfunction arrived at in section 3.4.1, the phrase 'just outside the surface' requires some clarification. The electron must be close enough to the surface that the surface can be approximated as nearly infinite in the x, y direction and the potential $V(z)$ is roughly a constant. The electron must also be far enough from the surface that the inhomogeneities in the surface do not influence the potential in the z direction. If the electron is too close the reference potential becomes a function of all three directions, $V(z, x, y)$. This close to the surface, there are different workfunctions at different positions in the x, y-plane, these are the local workfunctions. The global workfunction is the weighted average of these local workfunctions. The solid angle of the individual inhomogeneities from the position of the electron determines the appropriate weights for each of the local workfunctions.

Local workfunctions occur due to inhomogeneity in the surface dipole. Different patches of surface dipole have different local workfunctions. The ability to measure the local workfunction due to a specific patch is determined by how close the electron is to the surface and the size of the patch. Electrons closer to the surface can measure local workfunctions

of smaller patches. Specifically, for a local workfunction measurement, the electron must be at a point $z < 2R$ where R is the radius of the inhomogeneous patch. [90] The n=1 and 2 IPS electron expectation values of 3 Å and 13 Å from the surface, respectively, makes them sensitive to the local workfunctions of patches with radii greater than 6 Å and 26 Å.

Image potential state electrons photoemitted from patches with different workfunctions on the same surface will manifest at different kinetic energies in the TPPE spectra. In Figure 3.7, the bias potential has been set as determined for the monolayer coverage. With the adsorption of patches of a second layer of acetonitrile, a second n=1 IPS peak grows in at higher kinetic energy. The workfunction for two layers of acetonitrile is greater than for the monolayer. The monolayer bias potential accelerates electrons photoemitted from the patches of the second layer, resulting in the increased kinetic energy.

Chapter 4

A Self-Assembling Interface

Charge injection from a metal electrode into a molecular layer is an essential step in the operation of molecular electronic devices. A detailed understanding of the electronic structure at the metal/molecule interface is important to the investigation of molecular electronic events. Individual molecular electronic states like HOMOs and LUMOs combine to form the valence and conduction bands in molecular crystals. Electronic structure in the direction parallel to the interface can also influence charge injection and conduction perpendicular to the interface [92].

Many experimental and theoretical investigations of molecular electronic devices have focused on thiolate self assembling monolayers (SAMs) [10–13, 93, 94]. Thiolate SAMs provide an excellent system for several reasons: the layer structure and assembly dynamics are well documented, chemisorption ensures a strong bond between the molecule and the substrate, self assembly ensures structurally consistent overlayers, and current synthesis techniques can be applied to create a variety of systems to study [93, 94]. The structure and

adsorption of the thiolate SAM adsorbed on Ag(111) has been extensively studied [95–97].

The electronic structure of and electron transfer through thiolate SAMs is of great interest due to the possible use of these monolayers in electrical device applications. Experiments have measured conduction through single molecules [12], as well as rectification by an assembled monolayer [13]. Thiolate monolayer tail groups have been used to tune the Schottky energy barrier, and control charge injection into organic diode device structures [10,11]. Electron transfer through both unconjugated monolayers and conjugated thiolate molecules inserted into an unconjugated monolayer has been studied using STM [98–100]. Using thiolate covered mercury drop electrodes, Slowinski et al. measured both through bond and between chain coupling for electron tunneling [101]. Using theoretical methods, Yaliraki and Ratner investigated the influence of the interface on electron transport [92]. They concluded that increasing the number of bonds between the molecule and the substrate, or between neighboring molecules, would increase the conductance. Thus the electronic structure parallel to the interface will influence the conduction of electrons in the perpendicular direction.

Figure 4.1 depicts the components of a self assembling monolayer. In thiolate molecules, the sulfur head group has a strong chemisorption interaction with the metal. The Van der Waals attraction between the molecules results in an ordered layer where the alkyl chains stand upright on the surface. Poirier and Pylant studied the adsorption of a wide variety of thiolate molecules chemisorbed onto a Au(111) surface using scanning tunnelling microscopy (STM) [102]. By monitoring the surface structure as a function of thiolate coverage, the assembly mechanism of the monolayer was elucidated. Thiolate

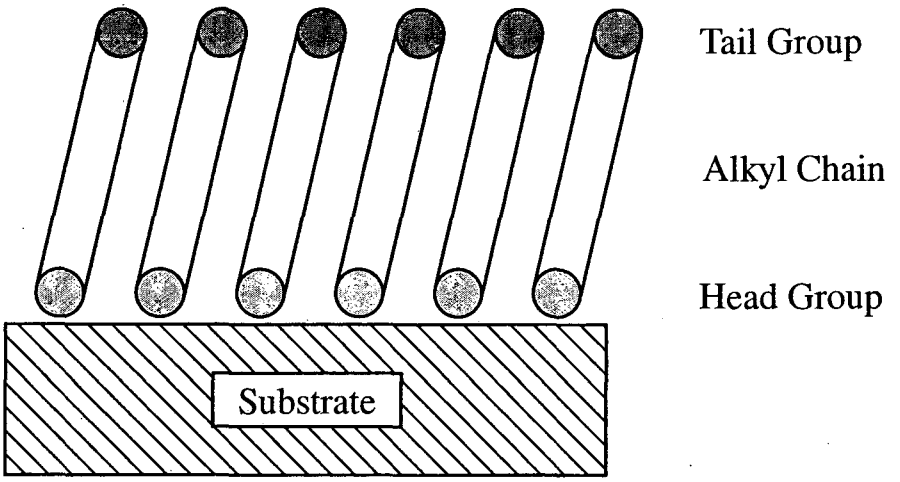

Figure 4.1: A self assembling monolayer consists of three parts: the head group adsorbs to the substrate, the alkyl chain is responsible for the assembly and a tail group at the vacuum or air interface. The attractive van der Waals interaction between the adsorbate molecular chains results in an ordered assembled monolayer.

molecules with a wide variety of alkyl chain and tail groups all had the same general assembly mechanism. For small coverages, the sulfur head group bonds strongly to the substrate and the alkyl body of the molecule lays flay against the surface. The molecules are far apart in this phase and form a lattice gas. As more molecules adsorb onto the surface, islands of molecules are formed all adsorbed with their chains flat against the surface. Eventually the entire surface is covered in this manner. If the coverage is increased past this point, a phase transition occurs, with islands of a more dense phase growing in. This more dense phase consists of thiolate molecules with the chains standing up from the surface. As the coverage is saturated, the layer consists almost entirely of the dense configuration with the upright chains.

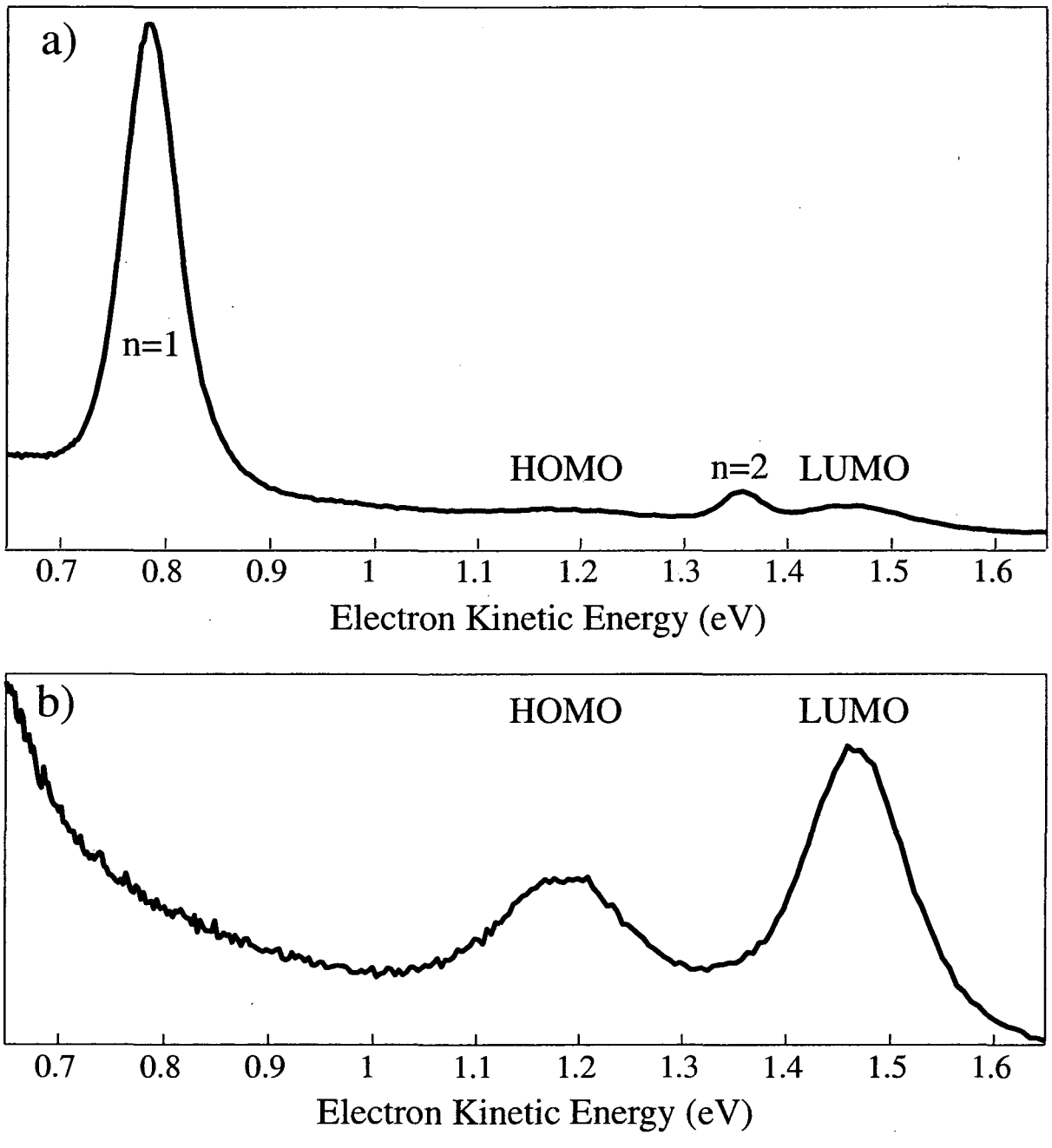

Figure 4.2: Spectrum of the methylthiolate monolayer. (a) With a 400 nm pump/800 nm probe, both the IPS and the thiolate electronic states are photoemitted. (b) With only 400 nm light, only the thiolate states are observed.

4.1 SAM Adsorbate Electronic States

The spectrum for a full methylthiolate layer are shown in Figure 4.2. At the 800 nm wavelength used to obtain this spectra, the n=3 IPS is not populated, so only the n=1 and n=2 states are observed. The visible light is filtered out in Figure 4.2b, showing two states photoemitted with the 400 nm second harmonic ultraviolet light. A wavelength survey is used to help with the identification of these peaks.

Figure 4.3a shows the kinetic energy spectra for several wavelengths. As described in section 3.2, the ultraviolet wavelengths used for this survey were obtained by doubling the white light, with the angle of the doubling crystal determining the specific wavelength. Figure 4.3b plots the kinetic energies of the photoemitted electrons as a function of the ultraviolet photon energy. The slopes of the lines are fit to 0.91±0.11 and 2.01±0.11, or 1 and 2 within error. As depicted in Figure 3.2a these slopes determine whether the electrons are photoemitted from an intermediate state above the Fermi level or an initially occupied state below the Fermi level. These results clearly indicate that one of the thiolate electronic states is initially occupied and the other is an initially unoccupied intermediate state. The occupied state, referred to as the HOMO, is located 1.8 eV below the Fermi level. The unoccupied state, referred to as the LUMO, is located 1.6 eV above the Fermi level. Taking the workfunction into account, this places the HOMO and LUMO 5.0 eV and 1.6 eV below the vacuum level, respectively. Resonant enhancement of the photoemission signal is observed in Figure 4.3 as the photon energy approaches the energy difference between the two states, indicating that a direct HOMO to LUMO transition occurs. These photoemitted electron peaks are assigned as the interfacial thiolate HOMO and LUMO because no silver

peaks are located at the observed energies prior to thiolate absorption. The unoccupied state is in the band gap of the Ag(111) surface where other surface states are not observed. The occupied state is located at an energy where silver has a constant density of states.

4.1.1 Thiolate HOMO and LUMO Dispersions

For the saturated monolayer, both of the observed adsorbate electronic states have kinetic energies that depend on $k_{||}$. The dispersion measurements for these states are presented in Figure 4.4. The unoccupied band has an effective mass of $m^* = 0.50m_e \pm 0.05m_e$. The kinetic energy of electrons from the occupied band decreases with increased $k_{||}$, fitting an effective mass of $m^* = -2m_e \pm 0.5m_e$. Thiolate interfacial electronic states have been seen recently for several molecules on a Cu(111) surface. Nondispersive HOMO and LUMO states [14], as well as dispersive LUMO and LUMO+1 states have been observed [15]. Dispersion measurements for these states were mentioned, but not published due to poor detector resolution. The angle resolved measurements reported here for adsorption on a Ag(111) surface show that both states are dispersive. The small effective mass of the unoccupied band ($m^* = 0.50m_e$) is indicative of a dispersive electronic state with large overlap between neighboring thiolate molecular orbitals. While still dispersive, the larger magnitude of the unoccupied band's effective mass ($m^* = -2m_e$) indicates a smaller overlap between the molecular orbitals. Within the tight binding approximation, the negative effective mass of the occupied band is consistent with p type orbitals possessing nodal planes perpendicular to the surface. This is in agreement with calculations of copperthiolate molecules, whose HOMO is primarily composed of sulfur 3p orbitals with a nodal plane parallel to the S-Cu bond axis [15].

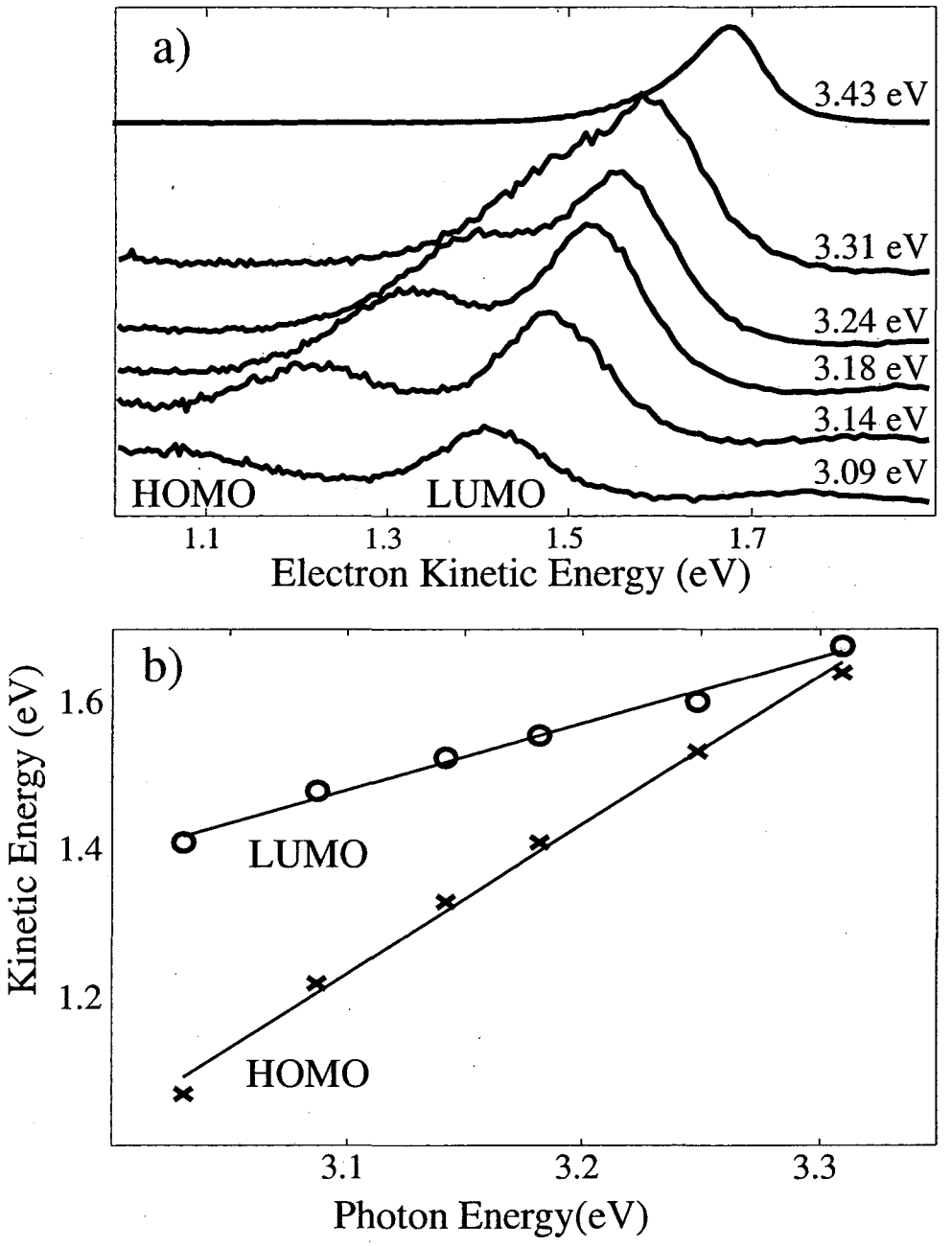

Figure 4.3: (a) Two photon photoemission spectra of the adsorbate electronic states as a function of photon energy. The signal of the spectra at 3.43eV photon energy is reduced by a factor of four. (b) Peak positions from (a) and least squares fit to the data points. The slopes of the two fit lines are 1 and 2 within error and clearly indicate that one state is initially occupied and that the other is initially unoccupied

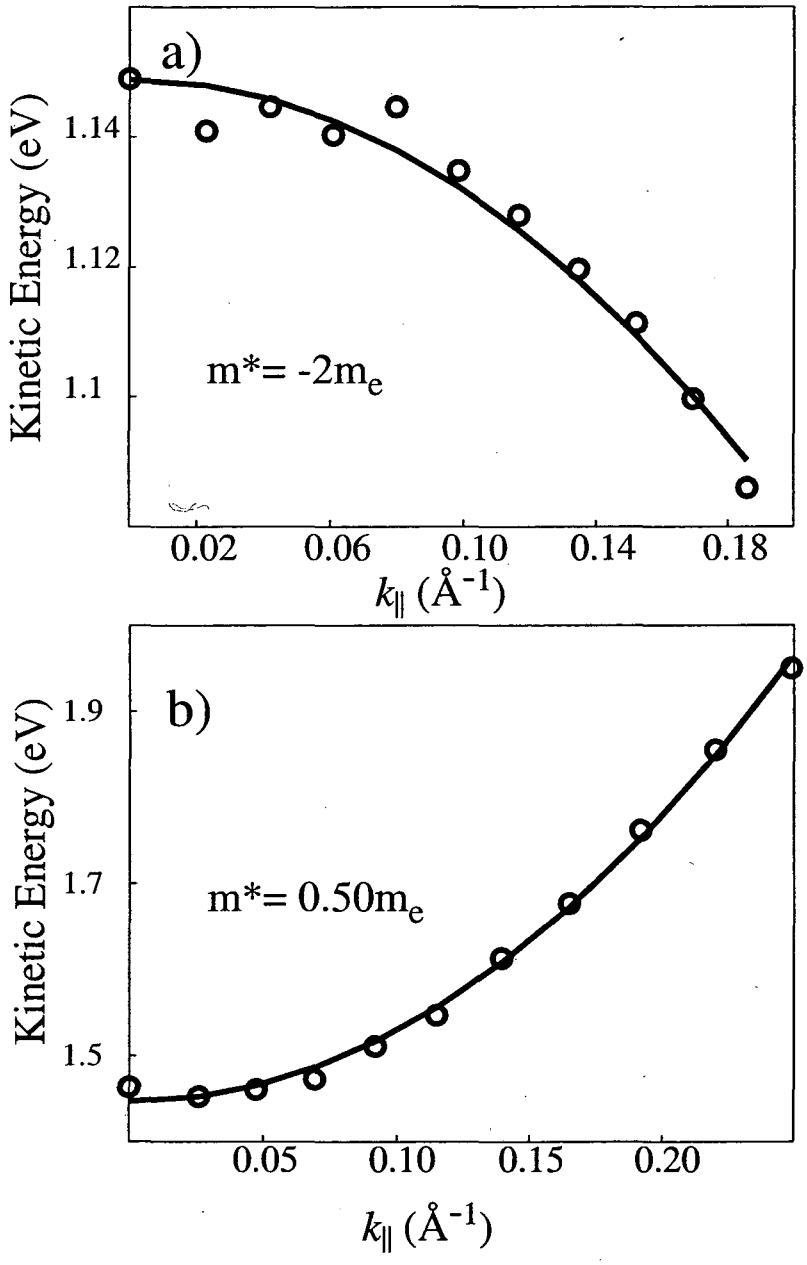

Figure 4.4: Dispersion measurements for the thiolate LUMO and HOMO. (a) The LUMO dispersion fits to an effective mass of $m^* = 0.50m_e$. (b) The HOMO dispersion fits to an effective mass of $m^* = -2m_e$.

4.1.2 Coverage Dependence of the LUMO Dispersion

At coverages less than that of the saturated monolayer, the LUMO is observed to be nondispersive. Dispersion measurements for the occupied state at sub-monolayer coverage have an effective mass that is too large and a signal to noise ratio that is too small to distinguish between dispersive and nondispersive behavior. Figure 4.5 shows dispersion measurements for the LUMO at three different exposures. At a 1 L exposure, the state is nondispersive. By the 2.5 L exposure, both dispersive and nondispersive states are observed. The effective mass of the dispersive signal at the 2.5 L coverage is the same as for the complete monolayer. At complete saturation (4 L) the nondispersive feature has mostly disappeared. At coverages between 1 L and 4 L, the dispersive signal grows in and the intensity of the nondispersive signal decreases as the exposure is increased. These coverage dependant dispersion measurements clearly show an abrupt transition from a nondispersive molecular state into a dispersive, delocalized electronic state. No gradual shift of the effective mass as a function of coverage was observed.

A discussion of these results would be facilitated by an estimation of the actual coverages at which the data were obtained, rather than the exposures. These coverages can be estimated using a few assumptions. First order Langmuir adsorption kinetics have been observed for thiolate adsorption onto gold surfaces [102, 103]. Assuming that these kinetics are also appropriate for adsorption onto silver surfaces, the relationship between the exposure time and the coverage is

$$\frac{d\theta}{dt} = -K(1-\theta), \tag{4.1}$$

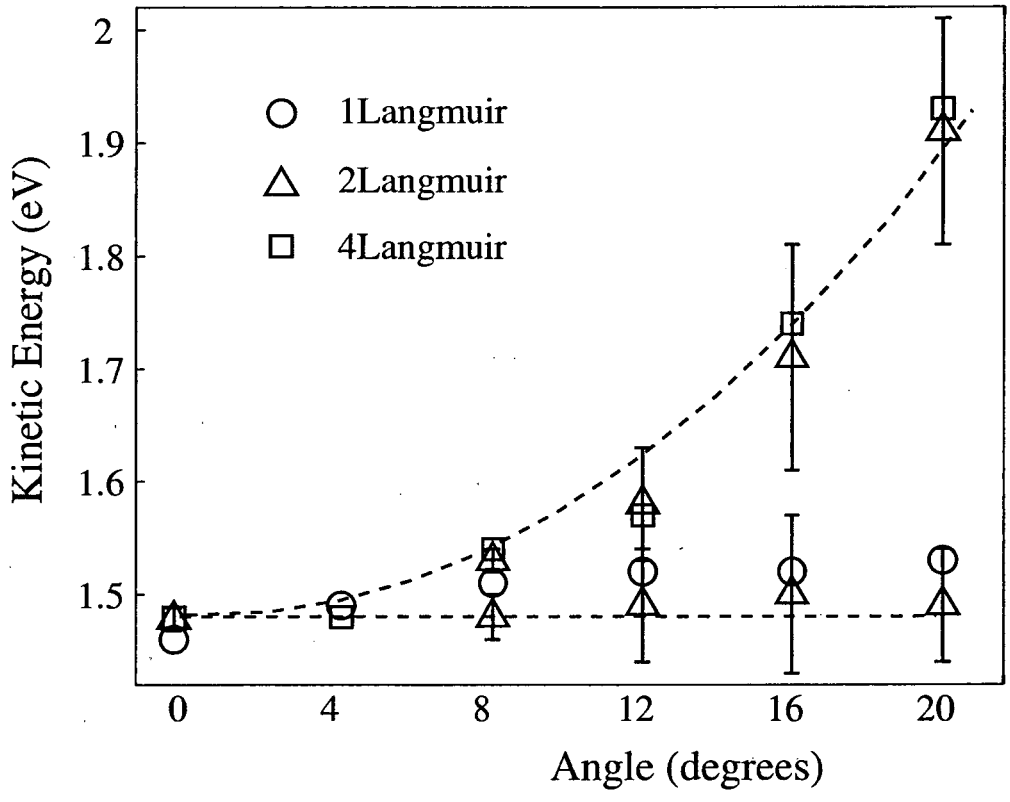

Figure 4.5: The LUMO is nondispersive at a small coverage and dispersive at a high coverage. At an intermediate coverage, both dispersive and nondispersive signal is observed.

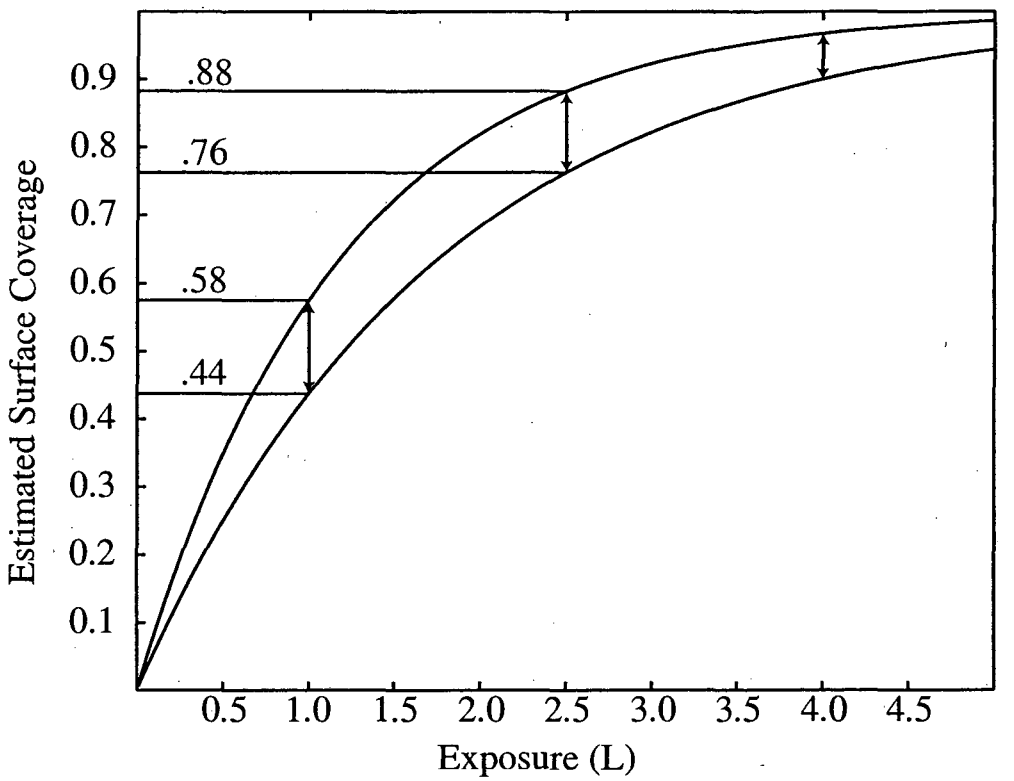

Figure 4.6: Assuming Langmuir kinetics, two plots of coverage as a function of exposure have been constructed. These plots can be used to estimate the coverage of methylthiolate molecules at the 1 L and 2.5 L exposures to be approximately 50% and 80%, respectively.

where θ is the surface coverage, t is time and the rate constant K includes the sticking probability and the flux of molecules at the surface. The molecular flux in the rate constant is related to the pressure of the gas introduced into the chamber, or the concentration of the thiol molecules for adsorption from solution. The flux can be removed from the rate constant to give a relation between the coverage and the exposure (L),

$$\frac{d\theta}{dL} = -k(1-\theta). \tag{4.2}$$

In Equation 4.2 the new rate constant, k, accounts only for the sticking probability. The flux has been accounted for by using the exposure instead of time.

Figure 4.6 plots the coverage as a function of exposure as obtained from Equation 4.2 for two different values of k. The values of k were chosen such that the 4 L exposure corresponded to 90% and 95% surface coverages. These values are taken as the lower and upper bounds on the coverage and constitute the second assumption necessary in the estimation of the surface coverage for the other exposures. As discussed in section 3.3.1, the 4 L exposure corresponds to the saturated monolayer and thus assuming $\theta \geq 90\%$ is reasonable. The upper bound of $\theta \leq 95\%$ is used because of the functional form obtained from Equation 4.2. If the upper bound is greater than 95%, the coverage difference between the 1 L, 2.5 L and 4 L exposures is smaller and starts to appear unreasonable. Using these bounding conditions, the coverage for the 1 L and 2.5 L exposures can be estimated to be within the ranges of 44-58% and 76-88%, or about 50% and 80%, respectively.

4.1.3 Surface Phase Transition

The simultaneous observation of both the dispersive and the nondispersive unoccupied states, with no gradual transition between the two, is strongly indicative of a phase transition. Though the chemisorption and data collection occurred at different temperatures, the phase transition was not observed with the temperature change, but rather with the change in coverage. This is consistent with the coverage dependant STM studies of Poirier and Pylant [102]. Their observations show that as the coverage is increased a lattice gas condenses into a more solid like phase, with the assembly chains parallel to the surface. Further increase in coverage results in a phase transition to a more dense layer with the chains standing up from the surface and the sulfur atoms from neighboring molecules packed closer together. This process is depicted in Figure 4.7 and is consistent with the energetics

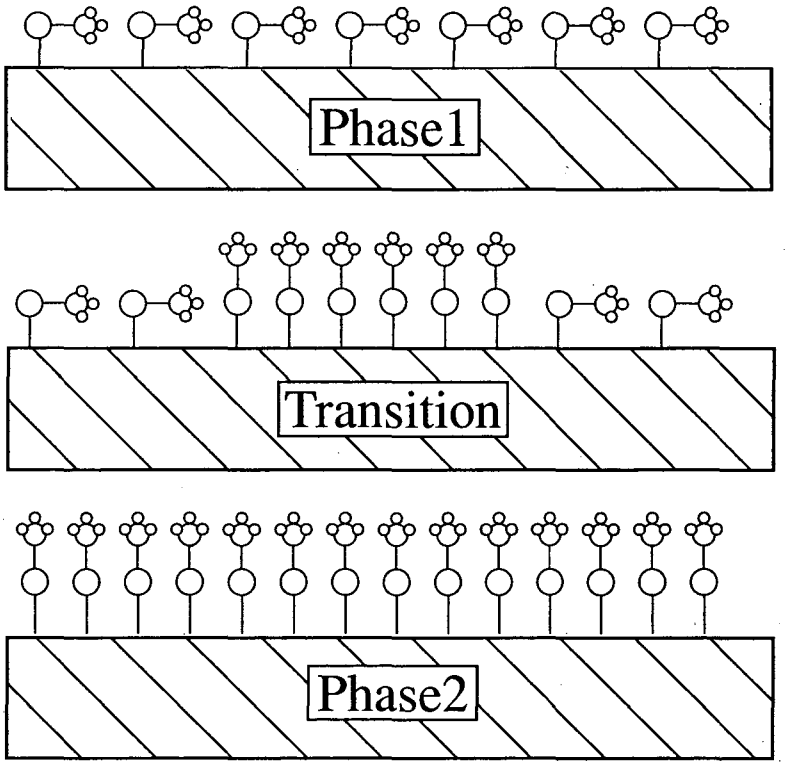

Figure 4.7: Phase 1 corresponds to the lowest coverage where the LUMO is nondispersive. Phase 2 corresponds to the tightly packed complete monolayer with a dispersive LUMO.

of a methylthiolate molecule adsorbed on a Ag(111) surface. Calculations indicate that the adsorbed molecule is slightly more stable with the sulfur-carbon bond parallel to the surface than with the S-C bond normal to the surface [95]. With greater coverages, the attractive interaction between carbon chains on neighboring molecules, and the increased energy of chemisorption overcomes the slight preference for parallel adsorption and results in more dense layers with upright chains.

The data is consistent with the following picture. At the 50% coverage, the thiolate layer resides mostly in the low density phase with the chains parallel to the surface (Figure 4.7a). This places the sulfur atoms further apart, influences the molecular orbital orientation with respect to the other molecules and prevents significant overlap of molec-

ular orbitals. By the 80% coverage, significant area corresponding to islands of upright chains have appeared (Figure 4.7b). The sulfur atoms are closer together and the molecular orbitals at the linkage between the thiolate and the surface overlap, creating a dispersive electronic state. As the coverage is increased the islands grow to become the dominant phase on the surface (Figure 4.7c) and the dispersive signal increases in strength while the nondispersive signal disappears.

4.2 Image Potential States at a SAM Interface

4.2.1 Energies, Effective Masses and Lifetimes

Figures 3.6 and 4.2a show the IPS for surfaces covered with methylthiolate and butylthiolate. For the methylthiolate layer, the IPS progression fits to a quantum defect (Equation 2.7)value of $a = 0.03$. The butylthiolate layer IPS fits to a quantum defect of $a = 0.05$. The binding energies obtained from these values are shown in Table 4.2.1.

Dispersion measurements for the n=1 and n=2 states at both of these layers are shown in Figures 4.8 and 4.9. The data are fit using

$$E_{kin}(k_{||}) = E_{kin}(k_{||} = 0) + \frac{\hbar^2 {k_{||}}^2}{2m*}, \tag{4.3}$$

where $k_{||}$ is obtained from Equation 3.1 and the effective mass and kinetic energy at $k_{||} = 0$ are the two parameters used in the fitting. Using this Equation, the effective masses for the n=1 IPS at the methylthiolate and butylthiolate monolayers are $0.75m_e \pm 0.15m_e$ and $0.9m_e \pm 0.2m_e$, respectively and the values for the n=2 IPS are $1.1m_e \pm 0.15m_e$ and $1.0m_e \pm 0.15m_e$, respectively. These values are also included in Table 4.2.1. All of these

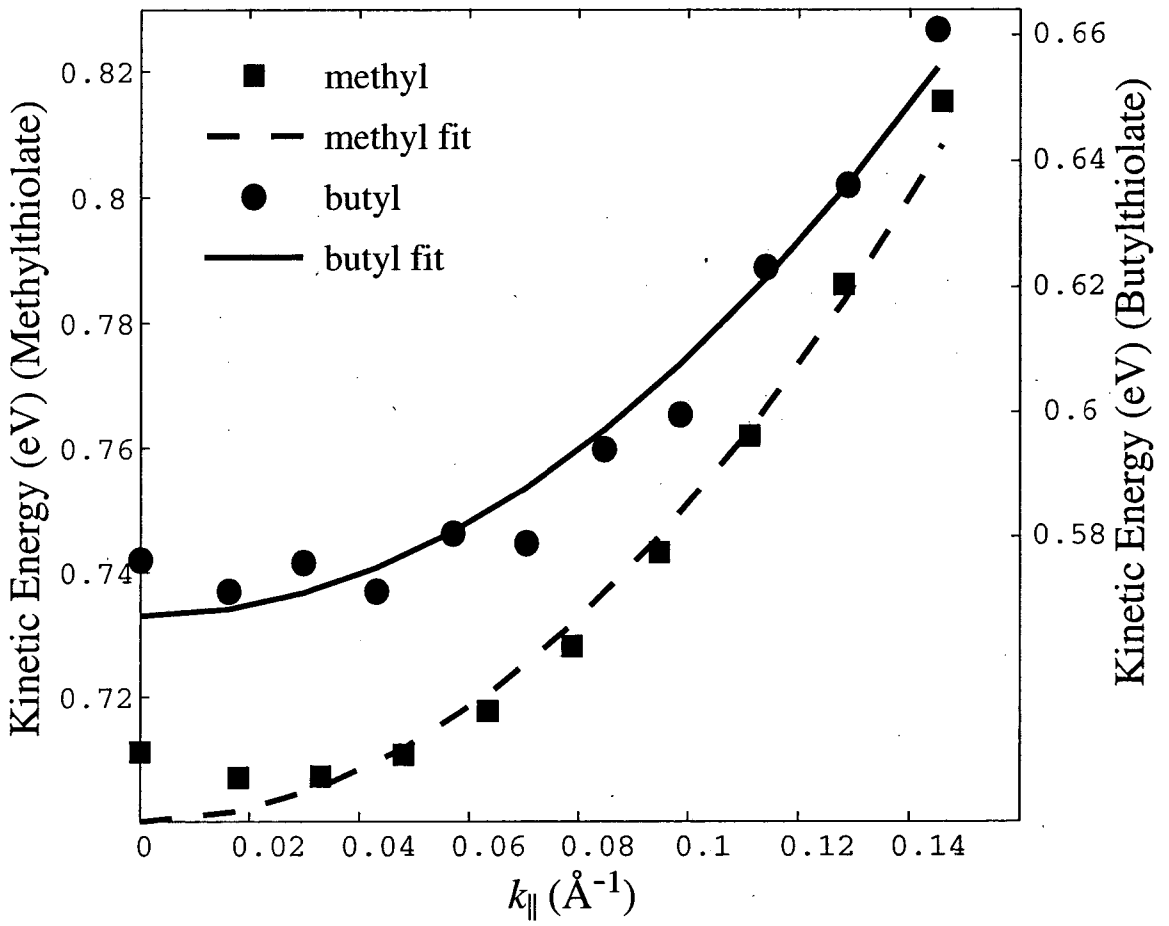

Figure 4.8: The dispersion measurements and the effective mass fits for the n=1 IPS at the methylthiolate and butylthiolate monolayers. These layers have effective masses of $0.75m_e$ and $0.9m_e$, respectively.

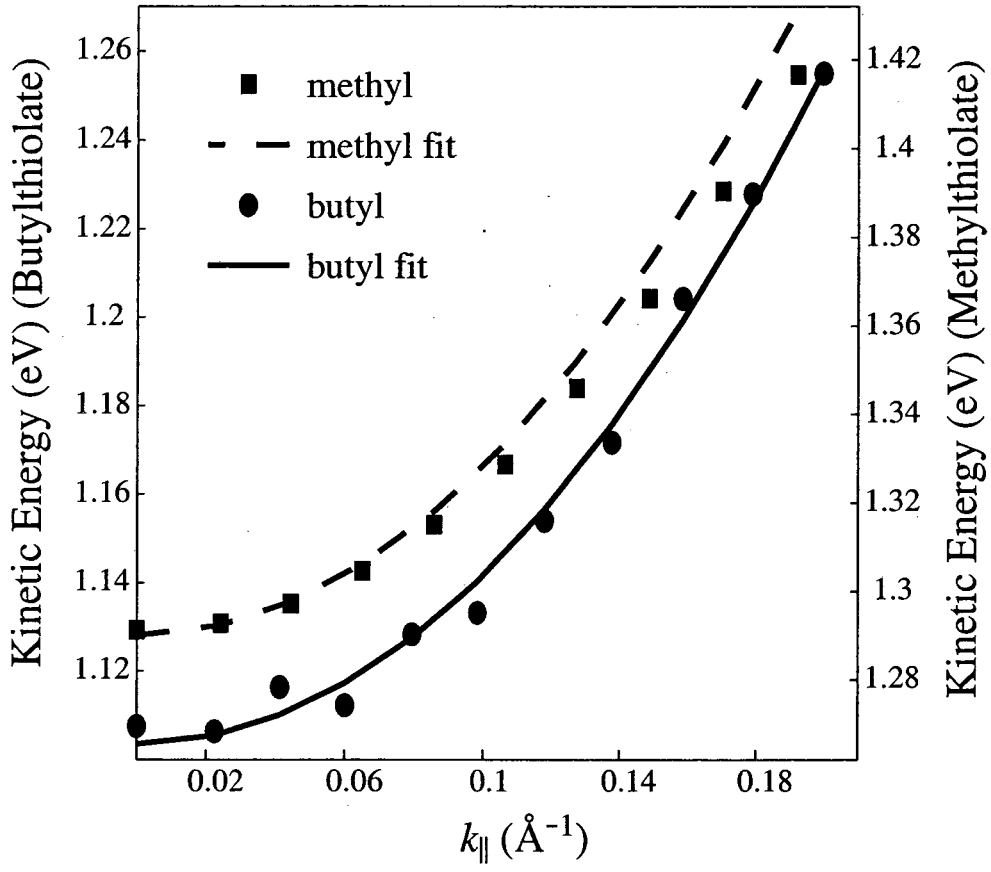

Figure 4.9: The dispersion measurements and the effective mass fits for the n=2 IPS at the methylthiolate and butylthiolate monolayers. These layers have effective masses of $1.1m_e$ and $1.0m_e$, respectively.

Table 4.1: Energies, Lifetimes and Effective Masses of Image States at Thiolate/Ag(111) Interfaces

	Binding Energy (eV)		Lifetime (fs)		Effective Mass($m*/m_e$)	
	Methyl	Butyl	Methyl	Butyl	Methyl	Butyl
n=1	-0.79	-0.76	80	80	0.75	0.9
n=2	-0.20	-0.20	250	60	1.1	1.0
n=3	-0.09	-0.09	500	110	-	-

states are dispersive. The effective mass of the n=1 IPS at the methylthiolate covered surface is less than that of a free electron. This is often an indication that the electron resides in the band structure of the layer. The effective mass of IPS electrons that have become quantum wells in xenon overlayers approaches the value for electrons in solid xenon. [58] The effective mass of the IPS electrons at the butylthiolate layer are free electron like and do not show this behavior.

The dynamic decay of electron population from the first three IPS at both the methylthiolate and butylthiolate layers are shown in Figures 4.10 and 4.11. As discussed in section 3.3.1, there were two distinct types of spectra observed for the butylthiolate layer. The lifetimes of the IPS electrons for both types of spectra were measured to be the same. Though the reason for the different types of butylthiolate spectra has not been determined, the difference did not manifest itself in the electronic lifetimes, indicating that the IPS electrons were not significantly influenced by the difference. Lifetimes for the IPS electrons were obtained by fitting the data to a convolution of two functions: a gaussian and an exponential. The gaussian width representing the instrument function of the laser pulses was determined by fitting the dynamics of the occupied surface state at the clean Ag(111)

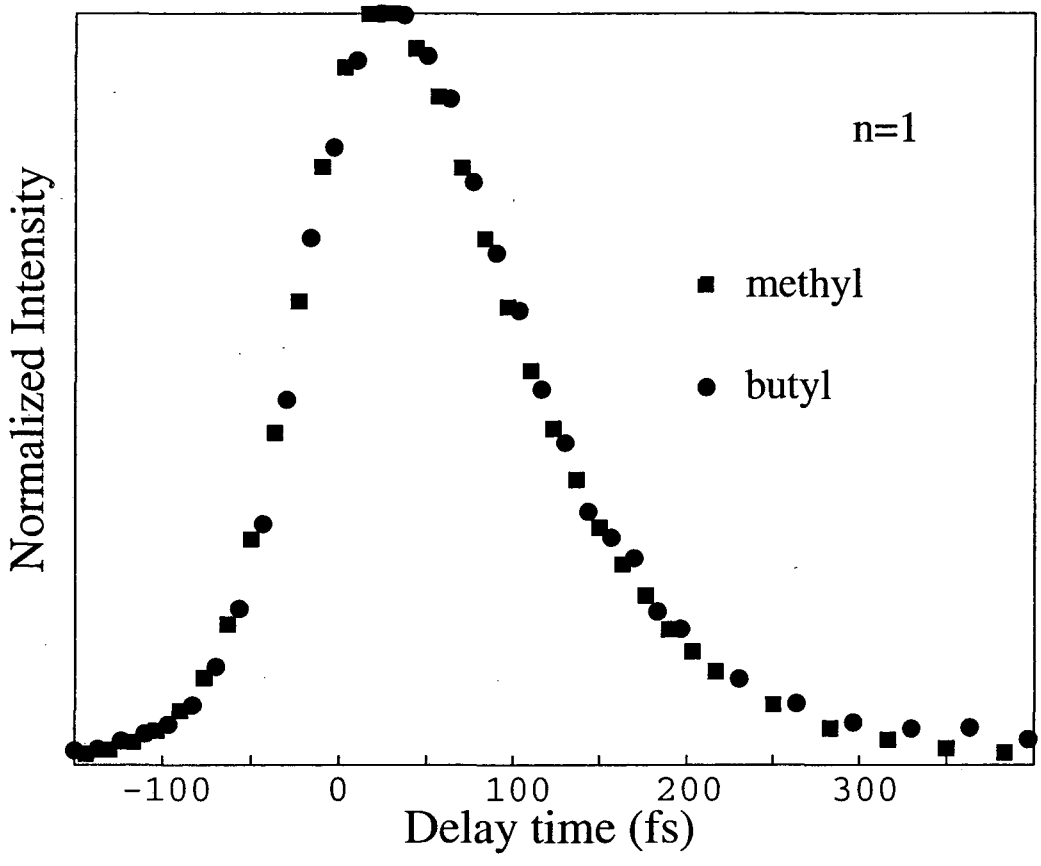

Figure 4.10: The lifetime data for the n=1 IPS electrons at methylthiolate and butylthiolate layers. Electrons at both layer types decay into the substrate at the same rate.

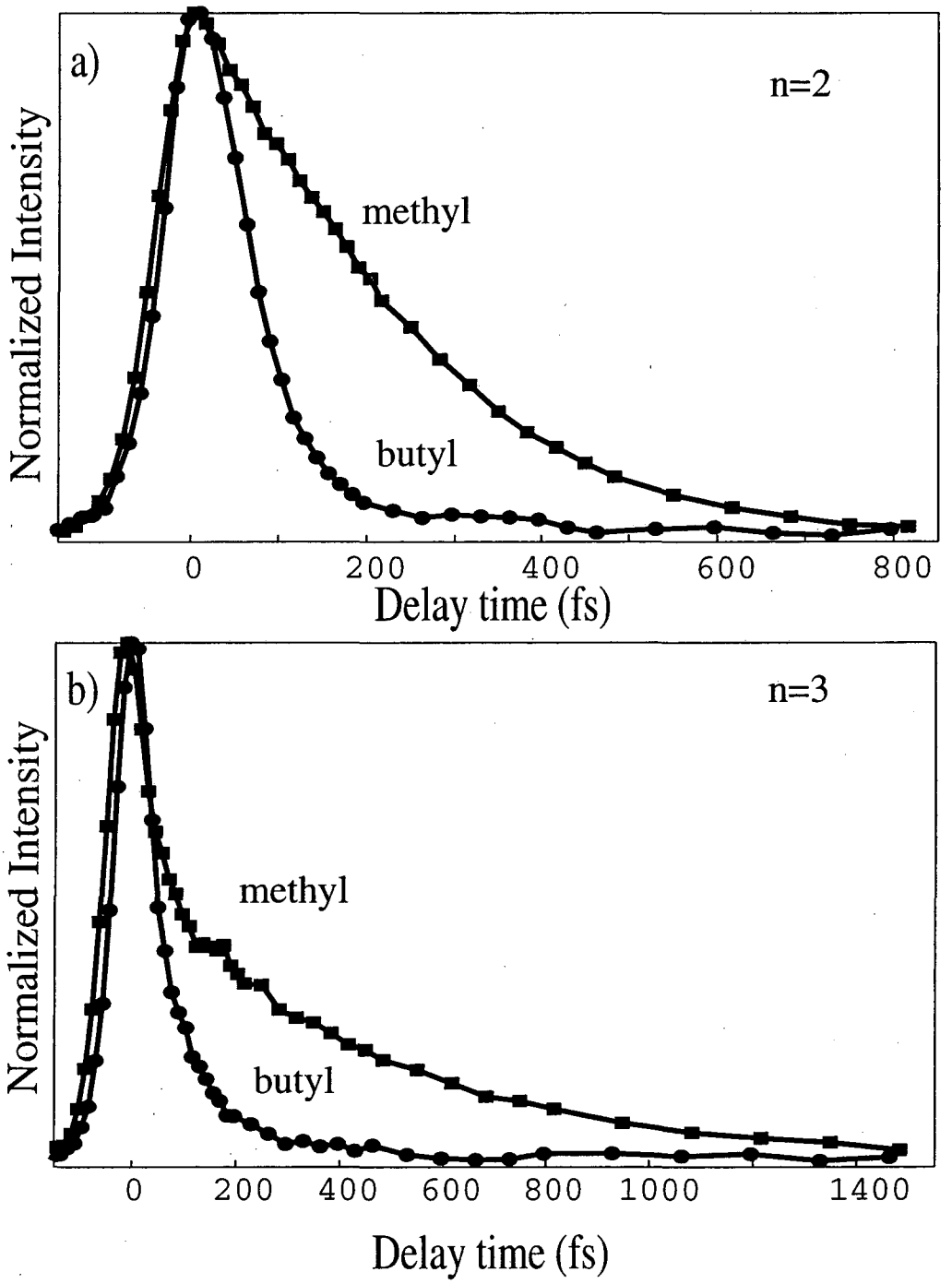

Figure 4.11: (a) and (b) Dynamics of the n=2 and n=3 IPS electrons, respectively. Electrons at the butylthiolate layer decay faster than those at the methylthiolate layer.

surface. The time constants for these fits are reported in Table 4.2.1.

Previous TPPE studies have exhibited two distinct types of IPS electron dynamics as a function of increased layer thickness. For layers with a negative electron affinity, the electron is not allowed within the layer and thus resides at the layer/vacuum boundary. By increasing the layer thickness, the electron has to tunnel through a larger barrier and the lifetimes increase exponentially. These dynamics are well described within dielectric continuum model calculations [54,59,69]. Alternatively, for layers with an attractive electron affinity, the IPS electrons are allowed inside the layer and increasing the layer thickness does not have as dramatic an effect on the lifetimes [56, 57]. These dynamics are also well described by dielectric continuum model calculations.

The primary difference between the methylthiolate and butylthiolate adsorbates is the thickness of the layer. The change from a one to a four carbon chain group increases the layer thickness from approximately 4 Å to 8 Å. This is similar to the physisorption of an additional layer used to investigate the electron dynamics as a function of layer thickness in the previous studies. The results of this additional thickness, however, can not be explained within the understanding gained by the previous results. The n=1 IPS electron lifetimes do not change as a function of the chain length. This lack of change, as well as the relatively short value of the lifetimes, is consistent with an IPS electronic wavefunction that is located within the layer and does not change significantly with the adsorption of the longer chain length molecular layer. A similar behavior is observed for growth of benzene layers on Ag(111) [57]. The layer dependent dynamic behavior of the higher IPS electrons is not consistent with previous studies. The lifetimes do not increase

as a function of layer thickness, as would be observed for negative electron affinity materials like alkanes. Neither do the lifetimes remain roughly constant, as would be observed for positive electron affinity materials, like benzene or xenon. Instead the lifetimes get shorter as the layer thickness is increased. In the next section, a dielectric continuum model will be used to explain this phenomenon. Though this model can explain the higher IPS electronic lifetime trends, the n=1 IPS lifetimes are not reproduced.

4.2.2 Dielectric Continuum Model Calculations

The dielectric continuum model assumes that the adsorbate layers can be treated as a dielectric, and ignores any structure on the layer. This is used to generate the potential normal to the surface outside of the substrate. These potentials can then be used to determine the wavefunctions of bound solutions and from the overlap with the metal obtain the lifetimes of the electrons. This was discussed qualitatively and within context of multiple reflection theory in section 2.2.1. Once the wavefunction has been calculated, its penetration into the metal can be calculated as

$$p = \int_{-\infty}^{0} \psi(z)^* \psi(z) dz, \tag{4.4}$$

where p is the penetration and $\psi(z)$ is the normalized wavefunction calculated using the dielectric continuum model. In order to obtain the lifetimes, the assumption is made that the scattering processes leading to decay of the IPS electrons are the same as for hot electrons in the bulk. The bulk electron linewidth can be calculated as $\Gamma_B = 0.13(E - E_{Fermi})$, where the scaling value of 0.13 was determined for silver [70]. Using this expression for the bulk

linewidth, the lifetime can be calculated using

$$\tau = \frac{\hbar}{\Gamma \cdot p} = \frac{0.66}{0.13(E - E_{Fermi})p}. \tag{4.5}$$

Since this takes into account the energy of the state relative to the Fermi level, in addition to the wavefunction penetration into the metal, the workfunction of the surface and the binding energy of the specific IPS are needed to calculate the lifetimes. The experimentally determined values for these energies are used in the lifetime calculations.

To obtain wavefunctions using the dielectric continuum model, a potential is required for both within the layer and outside of the layer in the vacuum. In the vacuum, the potential used is one determined by Cole [50] for an electron outside of a thin layer adsorbed onto a metal. This potential accounts for the polarization induced in the dielectric both by the electron and the charge distribution induced in the metal, as well as the polarization induced in the metal by the screened electron and the charge distribution in the layer. All of these components combine to form the vacuum potential outside of the layer,

$$V_{out}(t < z, t) = \frac{-\beta e^2}{4(z-t)} + \frac{(1-\beta^2)e^2}{4\beta} \sum_{n=1}^{\infty} \frac{(-\beta)^n}{z - t + nt}, \tag{4.6}$$

where z is the distance from the metal surface, t is the thickness of the adsorbed dielectric, $\beta = \frac{\epsilon-1}{\epsilon+1}$, where ϵ is the dielectric constant of the layer and e is the fundamental electric charge. This potential is undefined at the layer/vacuum boundary, so it is cutoff below -3.2 eV. Though this is arbitrarily set to the value of the workfunction, the results of the calculation are not significantly influenced by the exact cutoff used.

Within the layer, a couple of different potentials have been used. The simplest

form used set the potential equal to the electron affinity of the layer $V_{in} = -EA$. A slightly more complex potential is obtained in the approximation that the layer is infinitely thick. This results in the following potential,

$$V_{in}(z < t) = -\frac{e^2}{4\epsilon z} - EA. \tag{4.7}$$

This is essentially the image potential screened by the dielectric and referenced to the layer electron affinity instead of the vacuum energy. For finite layer thicknesses, this is not completely accurate, as it does not take into account the potential due to the induced polarization of the dielectric. Another potential has been used which takes this polarization into account [57,58,60,104]. Using Equation 4.7 as a starting point, an infinite series of corrections are added for the polarizations induced in the layer and the metal. This potential has the added problem that the potential diverges at the layer/vacuum boundary because of the bound surface charge and due to the abrupt discontinuity in the polarization at the interface. This aspect makes Equation 4.7 a more useful potential, especially for thin dielectrics where the unphysical nature of the layer/vacuum discontinuity can dominate the potential.

As already mentioned, these calculations cannot reproduce the lifetime behavior observed for the thiolate layers. While the alkyl chain tail group of the assembled layer is similar to the repulsive electron affinity alkane layers, the sulfur head group of the thiolate layers has a positive electron affinity. Indeed, the LUMO is directly observed by the TPPE experiments and is bound 1.6 eV below the vacuum energy. In addition to these problems, the chemisorbed nature of the adsorbate makes the assignment of a sharp layer/substrate

interface inaccurate.

The electronic structure of the thiolate layers can be approximated within the dielectric continuum model by using two layers. The inner layer represents the sulfur portion of the thiolate adsorbate and has a positive electron affinity of 1.6 eV (The LUMO energy measured with TPPE) and a dielectric constant bulk sulfur of ϵ=4. The second layer represents the alkyl chain groups and has a repulsive electron affinity of -0.2 and a dielectric constant of ϵ=2.3, the same values used for alkane molecules [54]. The interface between the two layers and the substrate is assumed to be sharp. The width of the sulfur layer used is 2.25 Å, which is half of the S-Ag bond distance plus half of the S-C bond distance. The alkyl thickness used for the methyl and butyl layers was 2.15 and 6.15 Å, respectively.

Equation 4.6 is used for the potential in the vacuum. Within the alkyl layer, the potential

$$V_{out}(t_1 < z < t_2, t_1) = \frac{-(\epsilon_1 - 1)e^2}{4\epsilon_2(\epsilon_1 + 1)(z - t_1)} + \frac{(1 - \frac{\epsilon_1 - 1}{\epsilon_1 + 1}^2)(\epsilon_1 + 1)e^2}{4\epsilon_2(\epsilon_1 - 1)} \sum_{n=1}^{\infty} \frac{(-\frac{\epsilon_1 - 1}{\epsilon_1 + 1})^n}{z - t_1 + nt_1}, \quad (4.8)$$

is used, where t_1 is the thickness of the sulfur layer, t_2 is the thickness of the entire adsorbate and ϵ_1 and ϵ_2 are the dielectric constants of the sulfur and alkane layers, respectively. This is just the potential given in Equation 4.6 due to the sulfur layer and screened by the alkane layer. Within the sulfur layer the best results were obtained by using $V = -EA$. Another possible potential used was a variation on Equation 4.7,

$$V_{in}(z < t_1, t_1) = -\frac{e^2}{4\epsilon_1 z} - \frac{\epsilon_2 - 1}{4\epsilon_1(\epsilon_2 + 1)(t_1 - z)} - EA, \quad (4.9)$$

which includes a term for the polarization induced in the alkyl layer by the electron as

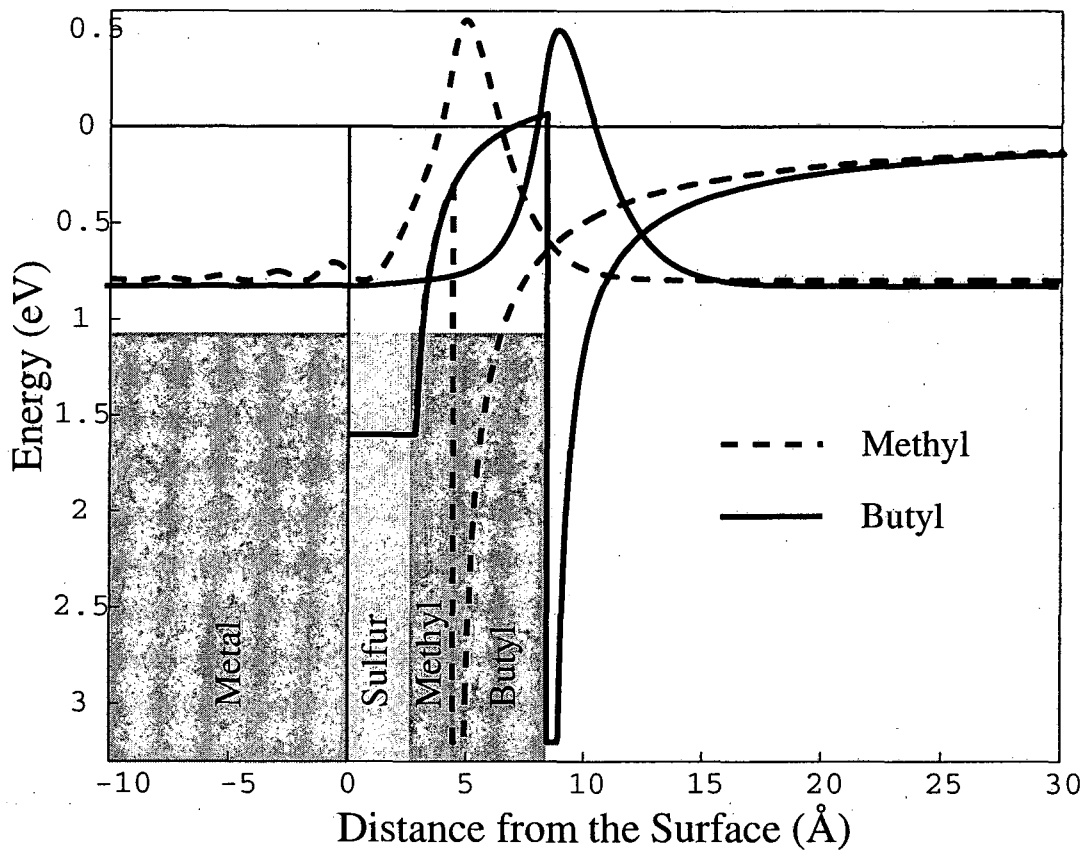

Figure 4.12: The potentials and calculated square wavefunctions for the n=1 IPS at the methylthiolate and butylthiolate adsorbate layers. Though the wavefunction for the methylthiolate IPS electron is close to the surface, the butylthiolate IPS electron wavefunction is pushed out to the vacuum/layer interface. This is inconsistent with the measured lifetimes.

screened by the sulfur layer. This potential also neglects the polarization effects due to the finite thickness of both the sulfur and alkyl layers. Qualitatively, the same trends were observed for this potential as for the simple flat potential at the electron affinity.

The potentials and resulting wavefunctions obtained from these calculations are shown in Figures 4.12 and 4.13. The lifetimes obtained from these wavefunctions were scaled by a factor of 1.5. These are reported alongside the measured IPS lifetimes in Table 4.2.2.

The n=1 IPS wavefunctions and lifetimes demonstrate the inability of this model to correctly model all of the important aspects of the layer. The calculations for methylthiolate has the n=1 IPS electronic wavefunction within both the sulfur and alkyl layers. For such a thin alkyl layer, there is not much of a barrier and the electron can have appreciable density in both places. This leads to a large overlap with the metal and a fairly short lifetime. For the butylthiolate calculations, the alkyl layer forms a substantial barrier and the n=1 IPS electronic wavefunction must reside either in the layer or in the vacuum. It is pushed into the vacuum, decreasing its overlap with the substrate and increasing its lifetime, disagreeing with the actual lifetime measurements. In fact, even increasing the sulfur layer thickness to an arbitrarily large value did not result in the electron moving into the layer; it always resided at the layer/vacuum interface.

The n=2 calculations (and n=3, though the wavefunctions are not shown) accurately reflect the trend of the decrease in lifetime as a function of alkyl chain length. This trend can be explained by the calculated n=2 wavefunctions shown in figure 4.13. For the methylthiolate calculations, the alkyl layer is too small to form much of a barrier between

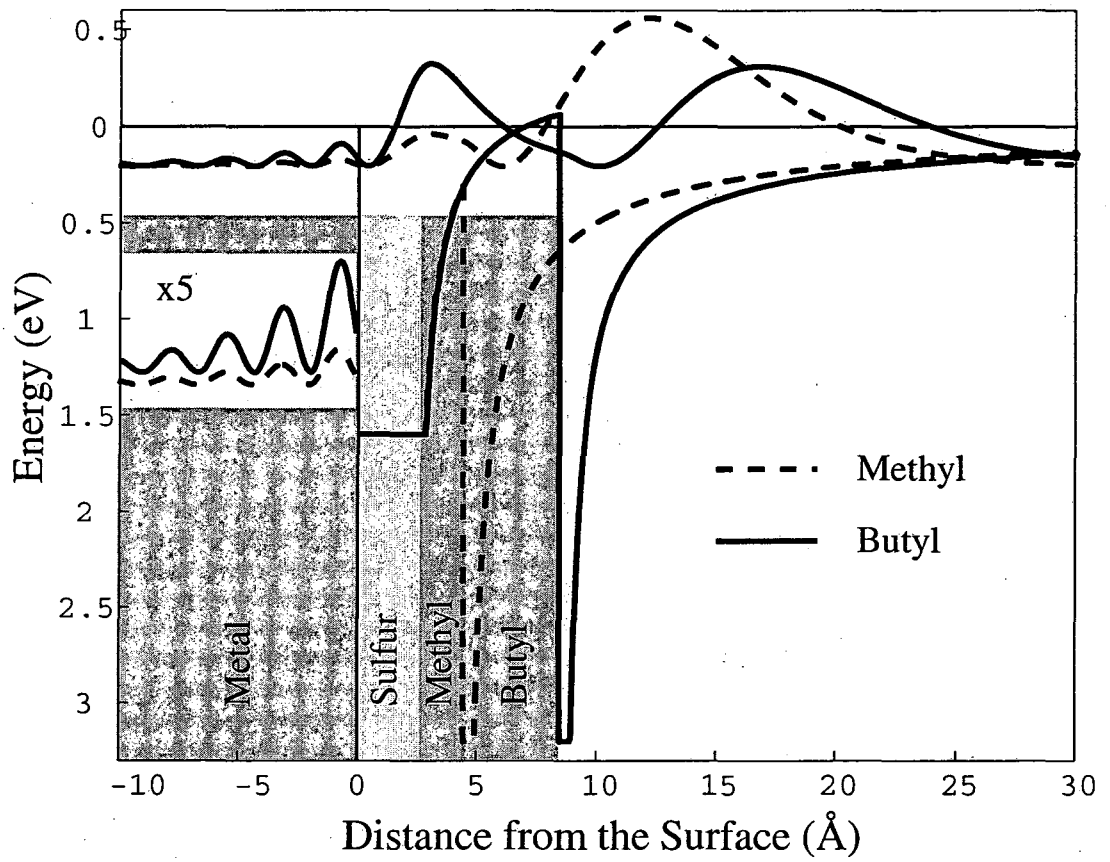

Figure 4.13: The potentials and calculated squared wavefunctions for the n=2 IPS at the methylthiolate and butylthiolate adsorbate layers. The larger barrier due to the butylthiolate alkane chain forces the electron into the layer and increases the overlap with the substrate. This results in a shorter lifetime relative to the methylthiolate layer, consistent with the measured trend.

Table 4.2: Calculated and Measured Lifetimes

	$n = 1$		$n = 2$		$n = 3$	
	Measured	Calculated	Measured	Calculated	Measured	Calculated
methylthiolate	80	84	250	202	500	508
butylthiolate	80	1355	60	62	110	32

the attractive potential in the sulfur layer and in the vacuum. As a result, the electron spreads out over this entire area. As the alkyl layer thickness is increased for the butylthiolate calculations, the barrier becomes significant, and the electron is forced into the sulfur layer.

This then leads to a conceptual understanding of the IPS lifetimes as a function of alkyl chain length. Though the calculations did not reproduce the n=1 experimental observations, the same measured lifetimes for both layers shows that the electron was not influenced by the change in the layer. This indicates that the electron was in the sulfur portion of the layer, bound between the surface and the alkyl chain. An increase in alkyl chain length would not change these boundaries, so the lifetime should be constant. The n=2 (and n=3) IPS electrons are initially able to be both in the sulfur layer and in the vacuum. Increasing the alkyl chain length confines the electron between the surface and the alkyl chain, pushing it in closer to the surface an decreasing the lifetime.

Chapter 5

A Polar Molecular Interface

Electron solvation describes an interaction of an electron with its surroundings. In the broadest sense, solvation occurs when the molecules surrounding a solute reorganize to accommodate changes in the solutes's spatial and electrical properties. Most experimental studies of solvation use molecular probes as solutes. An electronic transition within the molecule changes the net molecular dipole or the spatial configuration of the molecule, and the surrounding solvent molecules reorganize to accommodate this change. The time dependent solute energy is probed as a measure of this solvation. Reorganization of the internal molecular structure can also result, which complicates the interpretation of the measurements. Use of an electron as a solute eliminates this complication because an electron does not have any internal structure. Thus any dynamic changes in the measured electronic energy can result only from a reorganization of the surrounding solvent.

In general, solvation dynamics are known to critically influence the rates of a wide variety of process, including vibrational relaxation [22–24], ion transport [25], molecular

isomerization [17, 23], protein folding [18], and electron transfer reactions [19, 20]. While extensive investigations of solvation in isotropic media have been conducted [21–25], comparatively little is known about the dynamics of electron solvation at metal/molecular interfaces. This is a particularly interesting problem since both the reduced dimensionality and hindered solvent motion can result in dynamics distinct from those of isotropic materials [17–20].

This chapter describes the observation of electron solvation by overlayers of acetonitrile adsorbed on a Ag(111) surface. Image potential state electrons are stabilized by the reorientation of the acetonitrile molecules. The solvation manifests as a time dependent shift in the kinetic energy of the photoemitted electrons. This shift is observed for both localized and delocalized electronic states.

5.1 Dynamic Kinetic Energies

The kinetic energies of the monolayer n=1 and n=2 IPS electrons as a function of time delay between the pump and probe pulses are shown in Figure 5.1. The kinetic energies of both states are observed to decrease as a function of time delay. The kinetic energy of the n=1 IPS electron shifts by 0.277 ±0.010 eV and the kinetic energy of the n=2 IPS electron shifts by 0.280 ±0.010 eV. After about the 400 fs time delay, the n=2 IPS signal is lost in the noise, only reappearing after about the 700 fs time delay. Both the n=1 and n=2 IPS electrons decay back into the metal, and cannot be observed for delay times much greater than 1 ps. Throughout the lifetime of the IPS electrons, the kinetic energies continues to shift and a final energy is never reached, indicating that the layer never finishes

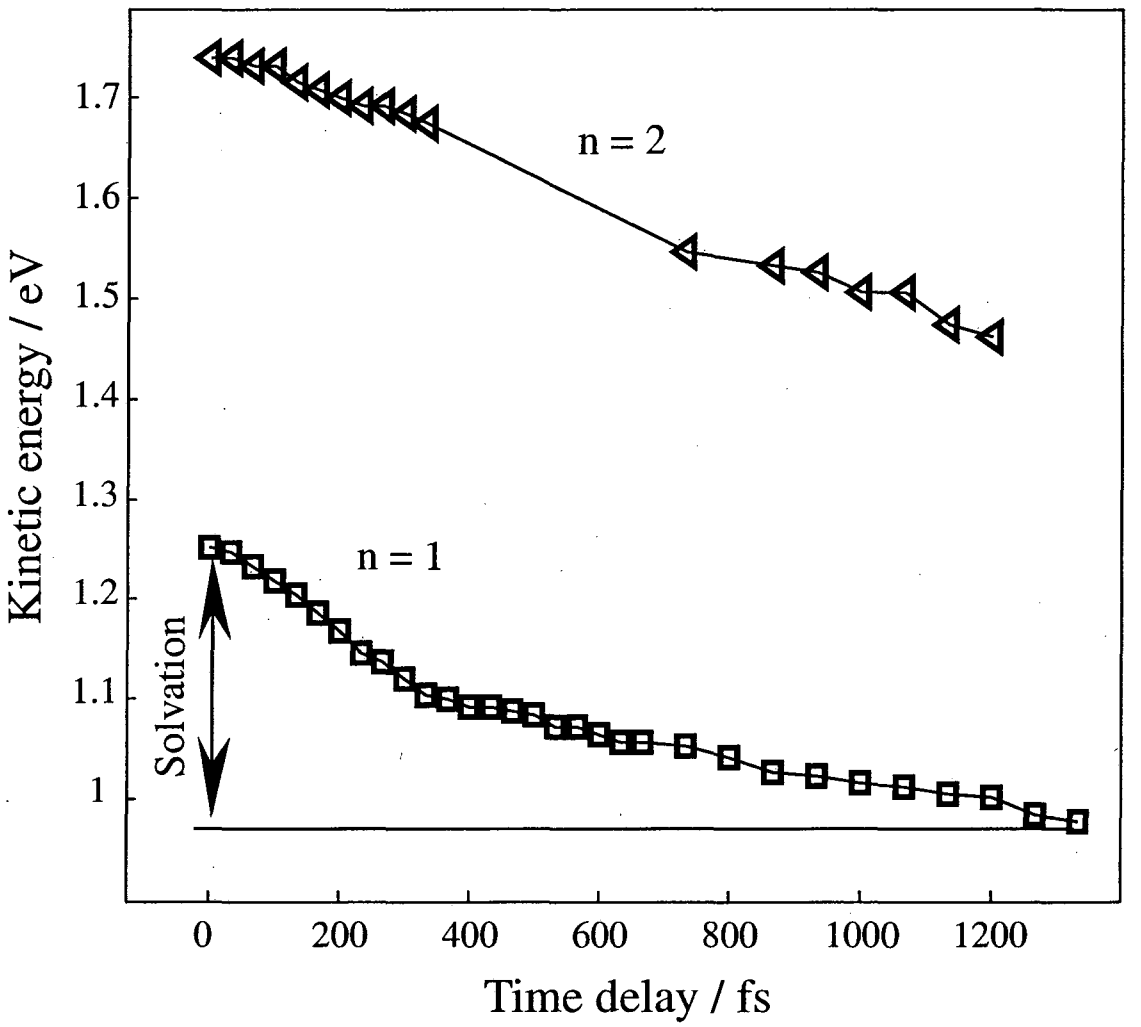

Figure 5.1: The n=1 and n=2 IPS electron kinetic energies are plotted as a function of time delay between the pump and probe pulses. The dynamic shift in kinetic energy is a result of electron solvation by the acetonitrile layer.

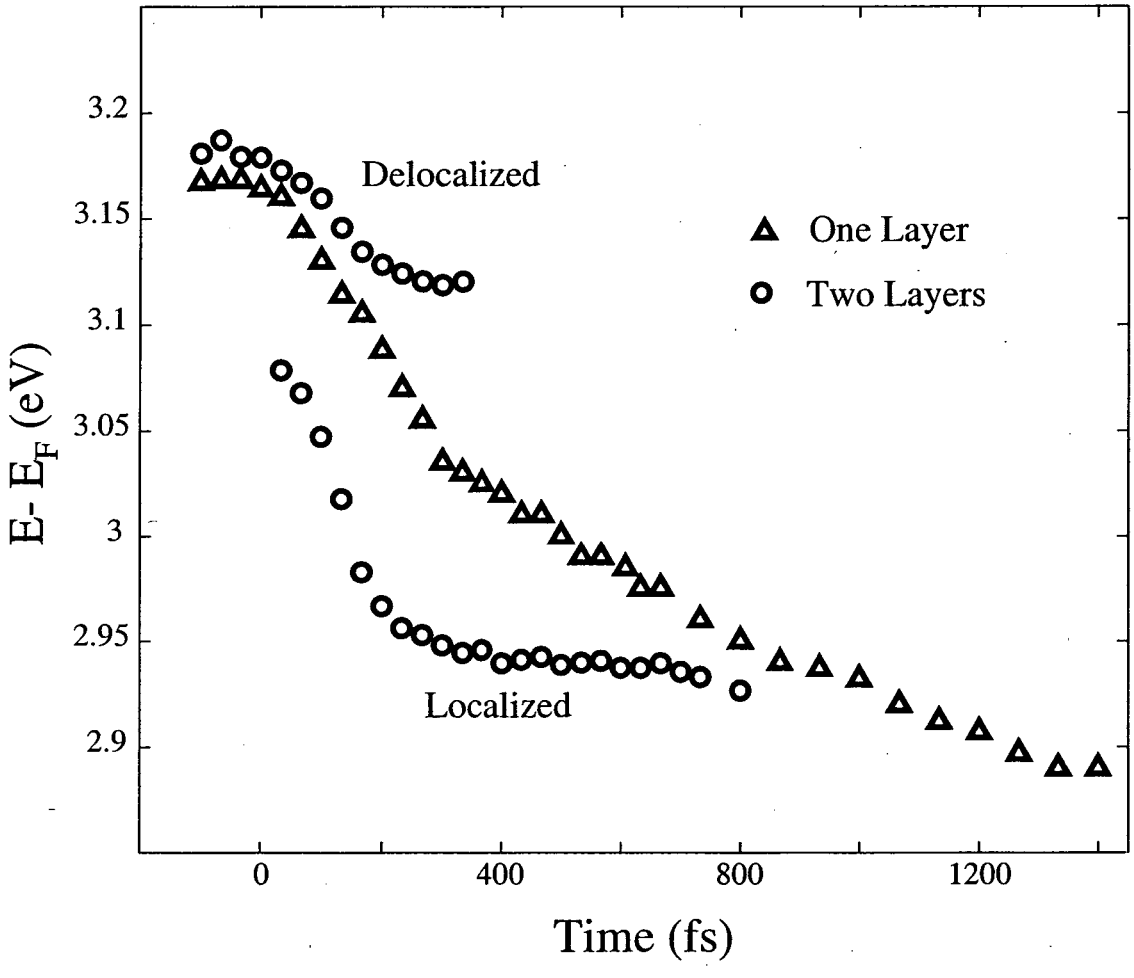

Figure 5.2: The n=1 IPS electronic energies as a function of time delay between pump and probe pulses show electron solvation. All energies are plotted in reference to the Fermi energy. The two layer data show the solvation of both the localized and delocalized states.

the reorientation in response to the electron.

Figure 5.2 shows the solvation of the n=1 IPS electron for both the one and two layer coverages. At the two layer coverage, the IPS electrons localize, as will be discussed in section 5.2. Both the delocalized and the localized state solvate, as can be seen in the figure. Similar dynamics have also been observed for butyronitrile and primary alcohols, ranging from methanol to 1-pentanol. All of these polar molecular solvation dynamics result from reorientations of the molecular dipoles in the adsorbate layer.

A key feature of the solvation dynamics shown in Figure 5.1 is that the energy shift for the n=1 IPS is the same as for the n=2 IPS. This indicates that the binding energies of the IPS electrons do not change. Equation 2.6 from section 2.2.1, used to calculate the IPS binding energies, is more accurately written as

$$E_n = V - \frac{0.85\ \text{eV}}{(n+a)^2}, \tag{5.1}$$

where the binding energies are referenced to some potential, V. The reference potential is usually assumed to be the vacuum level and is set to zero. Since the IPS electrons are bound to the surface, this potential is more accurately given as the surface potential, $V_{dip}(z)$ from Equation 3.2, used in the definition of the workfunction. Changes in the kinetic energies of the photoemitted IPS electrons are either due to changes in the photon energy or to changes in the IPS electronic energy as calculated by Equation 5.1. Changes in the photon energy can be ruled out as a cause of the observed solvation dynamics. Changes in the IPS binding energies has also been ruled out by the lack of variation in the energy separation between the n=1 and n=2 IPS. This leaves only the surface dipolar potential to account

for the observed solvation dynamics.

The surface potential, $V_{dip}(z)$, is due to the structure of the interface. Changes in the orientation of the acetonitrile molecular dipoles change the surface structure at the interface which changes $V_{dip}(z)$ and thus changes the workfunction. This corresponds to the solvation observed at the acetonitrile interfaces. The presence of the electron photoexcited to the surface by the first laser pulse induces a reorientation of the acetonitrile molecular dipoles near the IPS electron. This reorientation results in a local workfunction referenced to a local surface potential, $V_{loc}(z)$, to which the IPS progression converges. The difference in energies between the global and the local surface potentials is the solvation energy. This process is depicted in Figure 5.3.

The population dynamics of the n=1 IPS for two layers of acetonitrile are discussed in the next section. Figure 5.4 shows the population dynamics of the n=1 IPS for the monolayer acetonitrile coverage at several different wavelengths. The initial dynamics in the data collected at 665 nm fit to an exponential lifetime with constant τ=65 fs. A recurrence in the signal is observed at different times in all of the monolayer dynamics. The n=2 IPS population dynamics are also observed to have recurrences. The signal recurrence in the n=2 IPS is the reason that the longer time data in Figure 5.1 can be obtained. Though the n=1 data presented in Figure 5.4 resemble quantum beats, there is no other state close enough in energy for coherence oscillations to provide an explanation.

5.1.1 Disk-Dipole Model

The potential along the axis of a uniformly charged disk is used to obtain a model for the patch of reoriented acetonitrile molecules responsible for the local workfunction.

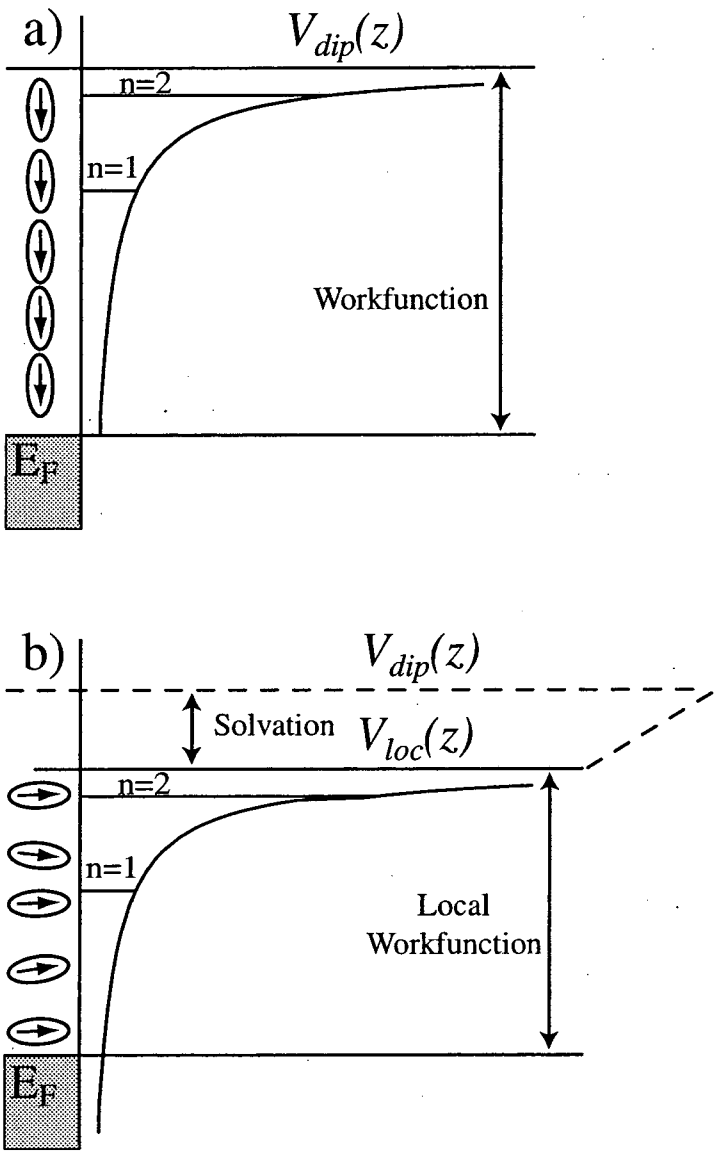

Figure 5.3: (a) The IPS progression converges to the surface potential, $V_{dip}(z)$. (b) After reorientation of the acetonitrile molecules, the progression converges to the local surface potential, $V_{loc}(z)$, making IPS electrons sensitive to local workfunctions.

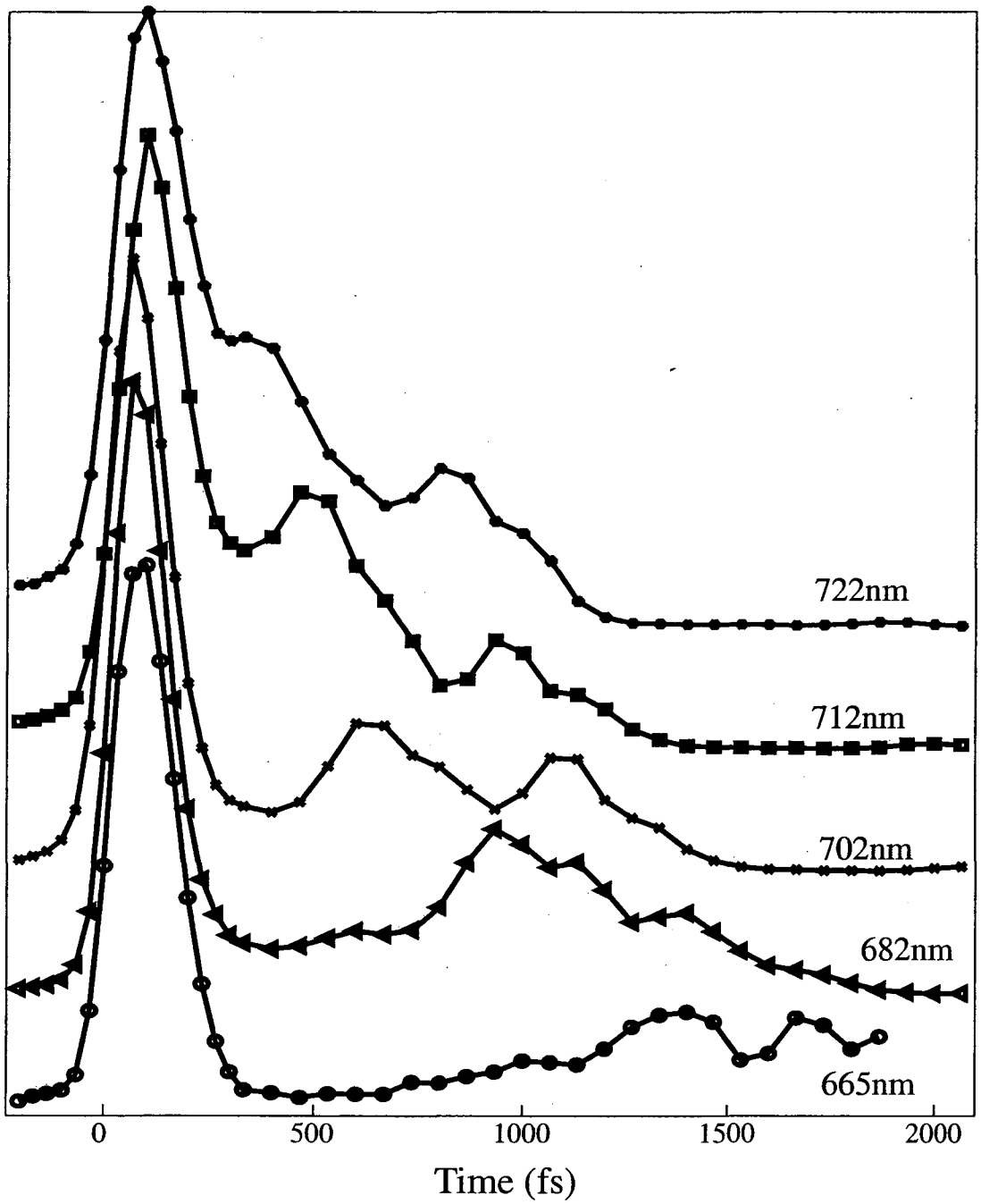

Figure 5.4: The population dynamics for a monolayer of acetonitrile at several different wavelengths. Population recurrences in all of the dynamic data.

The projection of the molecular dipoles onto the surface normal are represented by a pair of oppositely charged disks, as depicted in Figure 5.5. The potential along the axis of this configuration is given by

$$V(z) = -V_{\circ}\left(\frac{1}{d}\left[\sqrt{R^2+z^2} - \sqrt{R^2+(z+d)^2}\right]+1\right), \tag{5.2}$$

where d is the distance between the disks, R is the radius of the patch of inhomogeneity and z is the distance from the adsorbate. The constant, $V_{\circ}$, in front of the spatial variables determines the magnitude of the potential and is given by

$$V_{\circ} = \frac{qd\sigma}{2\epsilon_{\circ}}, \tag{5.3}$$

where q is the elementary charge, $\epsilon_{\circ}$ is the permittivity of free space and σ is the charge density on the disks.

The geometry of the oppositely charged disks mimics the surface patch or reoriented acetonitrile molecules. The distance between the disks, d, is the primary parameter through which reorientations of the molecules manifest in the model. Acetonitrile molecules with their dipole/bond axis parallel to the surface is represented by a value d=0. As the molecules rotate to solvate the electron, the projection of the dipole onto the surface normal increases until d takes on the value of the length of the acetonitrile molecular dipole. Thus an increase in the distance between the disks accounts for the reorientation of the molecules. The adsorption studies of acetonitrile molecules indicate that the bond axis of molecules in the second layer is closer to parallel than perpendicular to the surface [88]. In this case, the molecules initially have a nonzero projection of their dipoles onto the surface normal. This

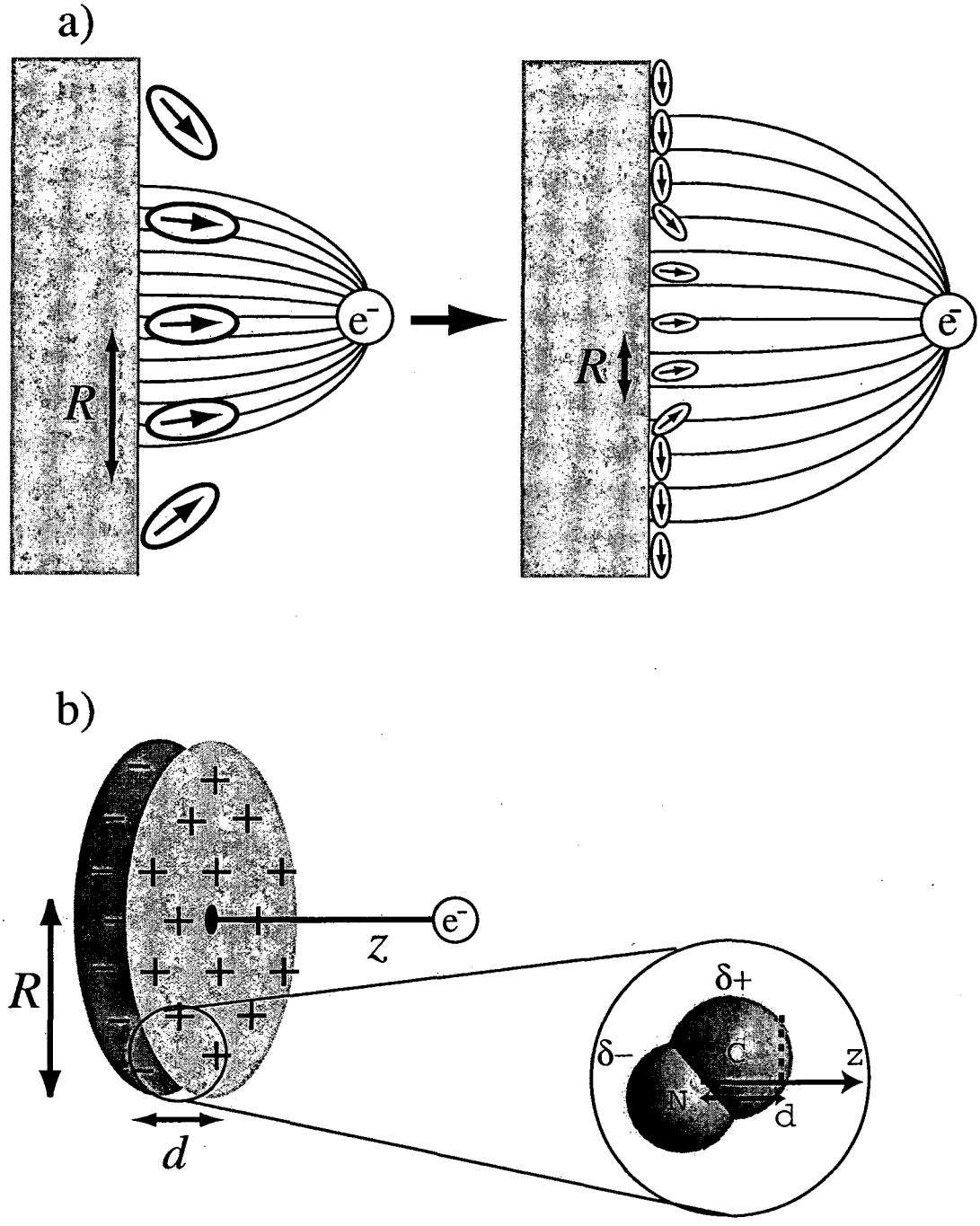

Figure 5.5: (a) An electron polarizes a local patch of molecules. After photoemission, the influence of the local patch is decreased. (b) Two oppositely charged disks are used to model the polarized patch.

would still be represented within the model as d=0, since d is the difference in the projected dipole of the reoriented patch with respect to the equilibrium position of the molecules. In this case the maximum value that d could take on would be less than the length of the molecular dipole.

The radius of the disks accounts for the finite size of the surface patch solvating the electron. As long as $R \gg d$, the radius of the disks will not significantly influence the magnitude of the potential change in the z direction. As discussed in section 3.4.2, in order to observe the local workfunction effect with the n=2 IPS electron, the radius of the local patch must be greater than $\sim$ 26 Å. This radius is more than an order of magnitude larger than the length of the dipoles, so the radius of the patch should not influence the magnitude of the change in local workfunction. This value of 26 Å represents a lower bound for the radius of the solvating patch. The main influence of the radius on the potential is to determine how quickly it drops off as the electron departs from the surface. For values of R in the 100 Å range, the potential has the correct distance dependance. It does not change significantly over the distance occupied by the n=1 and n=2 IPS, making them sensitive to changes in the potential. After photoemission, the electron quickly traverses the potential, so that the majority of the electron's flight time is at the appropriate kinetic energy.

Figure 5.6 shows the potentials generated using Equation 5.2 with three different radii, $R = d = 1.1$ Å, R=100 Å and R=10000 Å. All three potentials have the same functional form, though they scale differently with distance. Close to the surface, relative to the radius of the disks, the potential is fairly flat, as observed for the R=10000 Å potential. Far away from the disks, the potential takes on the form of a dipole potential, as observed

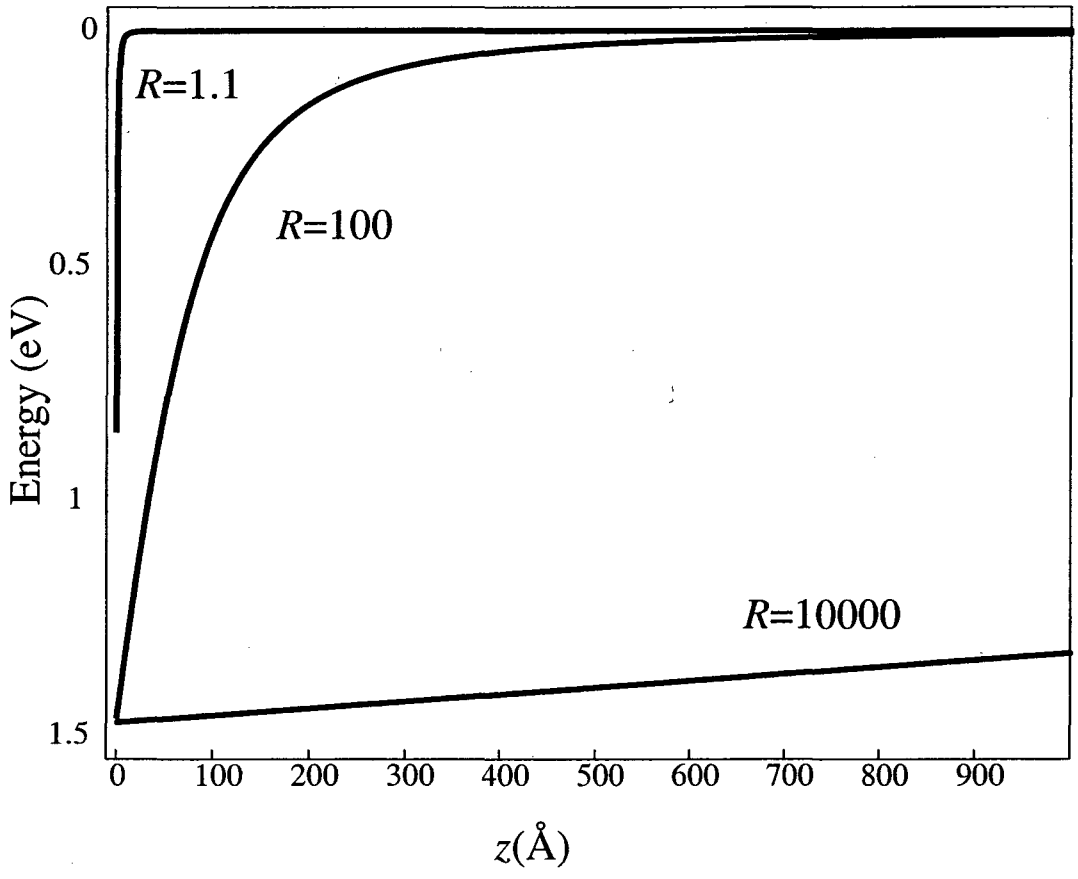

Figure 5.6: The potential generated from the disk-dipole potential (Equation 5.2) for three different disk radii.

for the R=100 Å potential. All three potentials approach the vacuum energy (0 eV) at large z. The two potentials with large R have the same energy at the surface, since these radii are much larger than d and thus are independent of the R value chosen. For the R=1.1 Å potential, the total energy is influenced by the size of the radius. This potential does not have the same energy at the surface as the other two. The energy difference at the surface between potentials generated with R=10 Å and R=10000 Å is less than 10% of the total energy.

The actual magnitude of the change in local workfunction is determined by V_o. The two parameters in Equation 5.3 that are system dependent are d and σ. The value of d is set at the carbon-nitrogen triple bond length of 1.1 Å. The 3.9 Debye dipole moment of acetonitrile [105] is divided by the dipole length to obtain the magnitude of the charge at each end of the dipole. This value is divided by area per molecule (50 Å^2) to obtain the charge density $\sigma = 2.37 \times 10^{-21}$ coulombs/Å^2 or $\sigma = 0.0148$ in units of the fundamental charge/Å^2. These values result in a maximum shift in the local workfunction of 1.47 eV. The measured value of 0.28 eV for the monolayer is within the range of this value. Though the measured energy shift differs from the theory by almost an order of magnitude, two factors must be taken into account. First, the electrons decay back into the metal before the layer completely reorients, so the actual total energy shift might be much larger. Second, the value calculated by the model assumes that all of the dipoles reorient from an initial parallel to an final perpendicular orientation. In reality, thermal disorder may result in fluctuations about the totally perpendicular orientation resulting in a measured energy shift smaller than the calculated value. Also, the molecules of the second layer do not start out in an

initial configuration that is completely parallel to the surface, though they are closer to parallel than to perpendicular [88]. This may help explain the reduced magnitude of the measured energy shift for the two layer coverage as compared to the monolayer coverage.

5.2 Localization

Figure 5.7 shows the angle resolved spectra of the n=1 IPS for two layers of adsorbed acetonitrile at 0 fs and 670 fs pump-probe time delay. The IPS electron is dispersive at the 0 fs delay time, while it has become localized by the 670 fs delay time. This is in contrast to the monolayer coverage, where the electron is dispersive at all times observed. The solvation dynamics for the localized and delocalized peaks for the two layer coverage are shown in Figure 5.2. As solvation in the liquid phase is commonly associated with localized solutes, it is surprising to note that the electron solvation observed can occur in response to a delocalized electron. Within the disk-dipole model, however, the solvation energy is independent of spatial extent parallel to the surface, as long as the radius is greater than about 10 Å. It is important to note that this model only accounts for the local workfunction potential of a given patch of the surface on the electron. Though this model gives a lower bound to the patch size it does not provide an upper bound. The size of the reorientation is limited by the number of molecules in the patch. For large patches, the reorientation energy per molecule is very small. If this energy is too small, no reorientation will be observed.

Figure 5.8 shows the population dynamics for the n=1 IPS for two layers of adsorbed acetonitrile at $\theta = 0°$. The contour plot shown in Figure 5.8a shows the population transfer from the delocalized state at about 1.45 eV of kinetic energy to the localized state

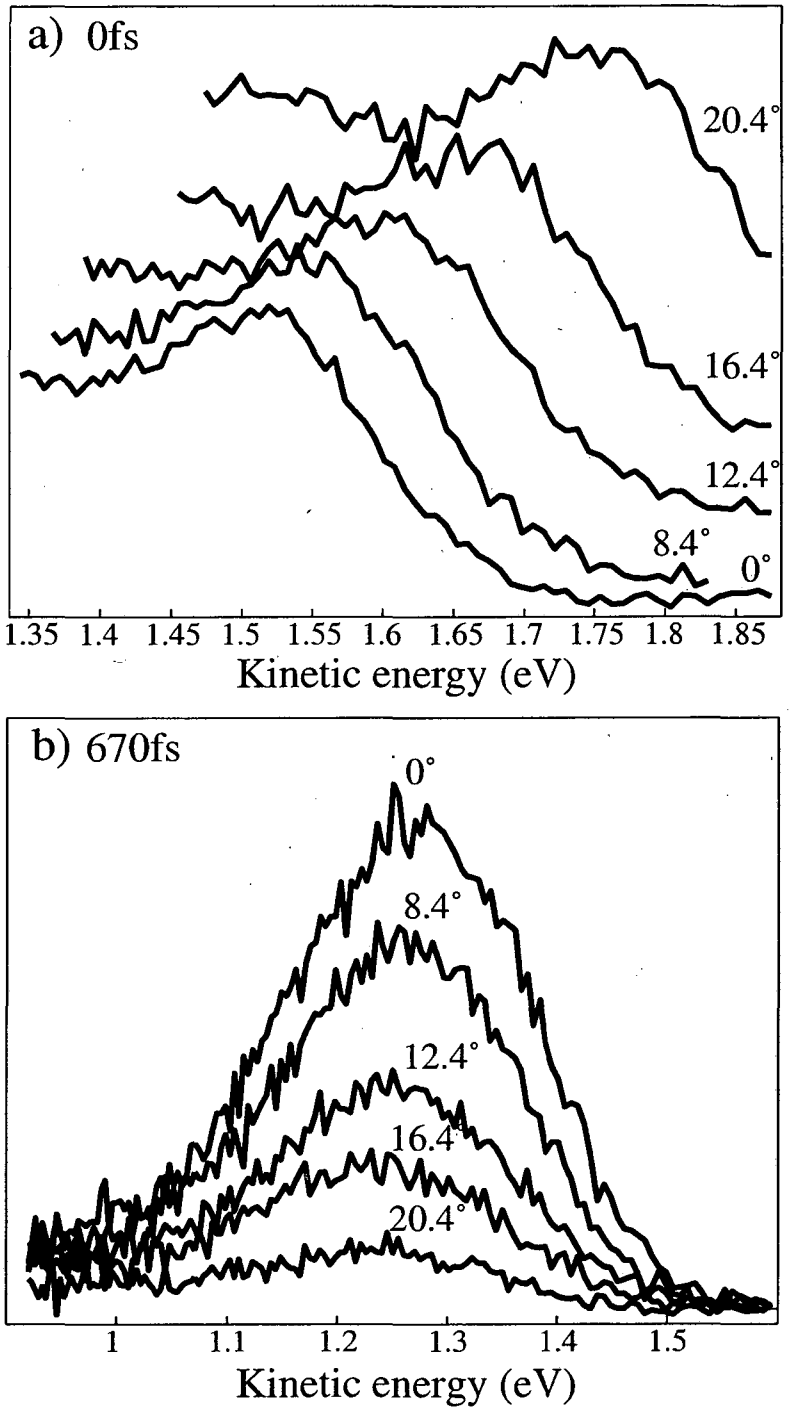

Figure 5.7: The photoemitted n=1 IPS kinetic energies as a function of angle at two time delays. (a) At a 0 fs delay, the electron is delocalized. (b) By 670 fs, the electron has localized.

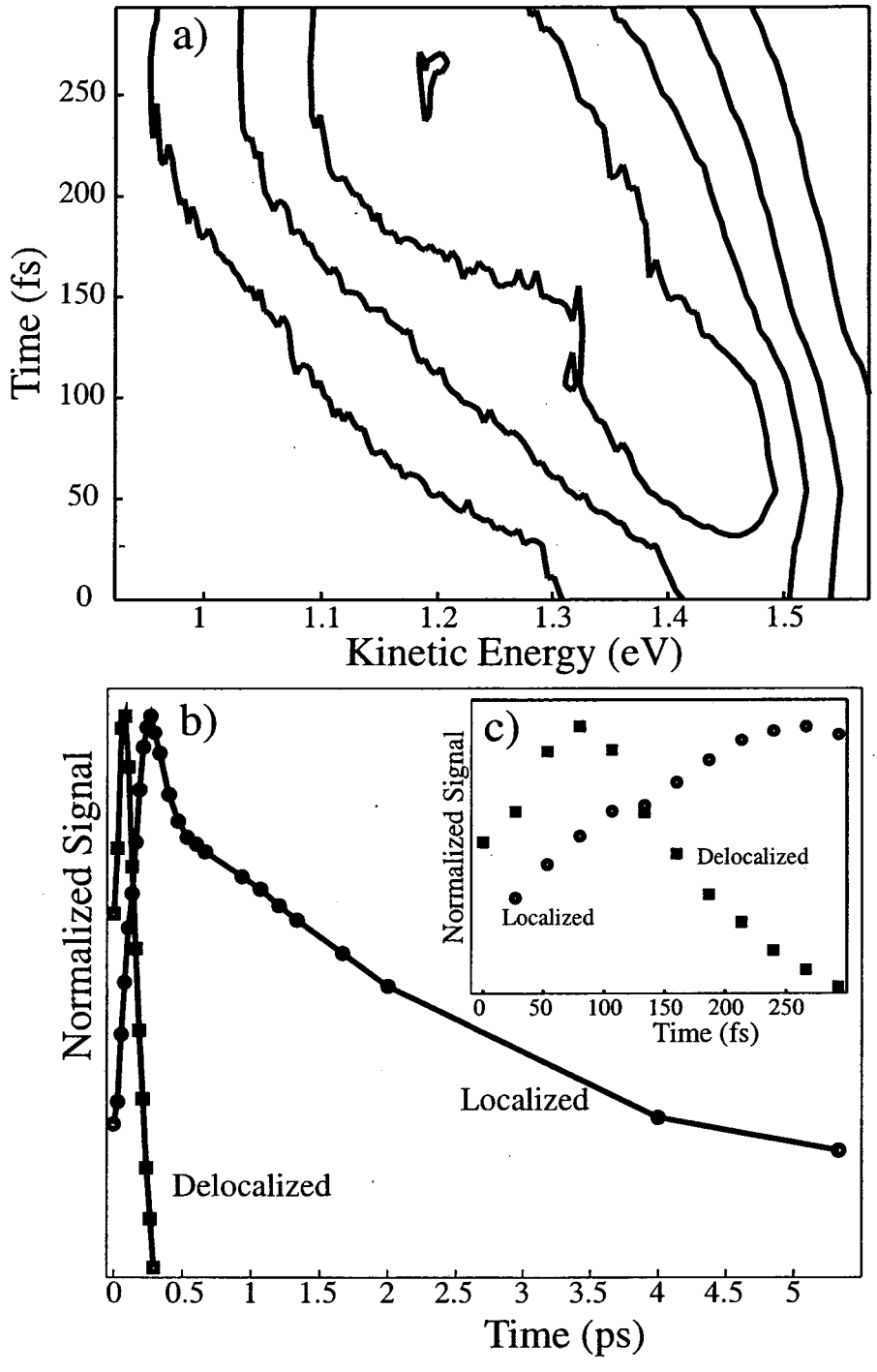

Figure 5.8: The population dynamics of the n=1 IPS electron at two layers of acetonitrile adsorbed on Ag(111). (a) A contour plot shows the population transfer. (b) Amplitudes of the localized and delocalized states. (c) Enlargement of the short time rise of the localized state and decay of the delocalized state population.

at about 1.25 eV of kinetic energy. The shifting of the peaks from higher to lower kinetic energy due to solvation can also be observed. One feature of interest in the two acetonitrile adsorbate layer data is the fact that the energy difference between the localized and delocalized states is large relative to other systems (including butyronitrile) that also localize IPS electrons. This energy separation simplifies the extraction of the population dynamics of the respective states at the $\theta = 0°$ angle shown here. Figure 5.8b shows the normalized population dynamics of the delocalized and localized electronic states. The delocalized state data fit to a rise time of 40 fs and a decay time of 60 fs. The localized state data fit to a rise time of 80 fs and a decay time of 3.5 ps. The similar time scales for the rise of the localized state and the decay of the delocalized state are indicative of population transfer. The dynamics of this population transfer occur at early times have been enlarged to match the time scale used in the contour plot. This can be seen in the inset, Figure 5.8c.

The difference between the 65 fs decay time constant of the delocalized monolayer n=1 IPS and the 3.5 ps time constant for decay of the localized state through two layers of acetonitrile is dramatic. This difference reflects the change in overlap of the IPS electronic wavefunctions with the metal. Two layers of acetonitrile molecules are much more efficient at screening the electron from the metal than one layer, resulting in significantly longer lifetimes.

Chapter 6

Conclusions

This dissertation has investigated the structure and dynamics of electrons at two strongly interacting interfaces. The alkylthiolate self assembling monolayers form a strong bond with the silver substrate. The electronic structure of the layer is observed, as well as the interaction of the IPS electrons with the layer's electronic structure. The use of thiolate SAMs in investigations of molecular electronic devices makes knowledge of the specific layer electronic structure and the influence of this structure on charge transfer important. At the acetonitrile/Ag(111) interface, the interaction between the surface and the adsorbate molecules is a weak physisorption. The excited electrons, however, have a relatively strong charge-dipole interaction. This strong interaction between the electron and the adsorbate results in both solvation and localization of the electron. Electron solvation at metal surfaces is important in a wide variety of problems of importance and interest within the fields of chemistry and physics.

Adsorption of methylthiolate onto Ag(111) results in a decrease in workfunction

from 4.56 eV to 3.20 eV. Two adsorbate electronic states are observed for the methylthiolate SAM. The HOMO is located 1.8 eV below the Fermi energy. The LUMO is located 1.6 eV above the Fermi energy in the band gap of the (111) surface of silver. Both adsorbate electronic states are dispersive for the complete coverage. The HOMO has an effective mass of -$2m_e$ and the LUMO has an effective mass of $0.5m_e$. The dispersive nature of the LUMO parallel to the surface is dependent on the coverage of the adsorbate molecules. The transition from nondispersive to dispersive behavior as a function of coverage is attributed to a surface phase transition. In the lower coverage phase, the molecules adsorb with their sulfur-carbon bond axis parallel to the surface. At the higher coverage a more dense layer is formed with the bond axis perpendicular to the surface. The importance of the dispersive nature of the LUMO is emphasized by theoretical calculations [92]. These calculations indicate that the conductivity of electrons through a SAM perpendicular to the interface is increased by the presence of electronic connections between adsorbed molecules in the parallel direction.

The dynamics of IPS electrons at methylthiolate and butylthiolate interfaces have been measured. The 80 fs lifetime of the n=1 IPS electrons does not change as the length of the thiolate carbon chain is increased. This is consistent with an IPS that is located within the layer, and more specifically within the sulfur region of the thiolate adsorbate. With the electron in this region, changes in the distance to the alkyl/vacuum interface will not influence the penetration of the electronic wavefunction into the metal, and thus will not influence the lifetime. The lifetimes of the n=2 and n=3 IPS electrons *decrease* as the thickness of the alkyl chain is increased. The n=2 IPS electron lifetimes changes

from 250 fs for the methylthiolate layer to 60 fs for the butylthiolate layer. Dielectric continuum calculations are used to illustrate this behavior. For the methylthiolate layer, at the binding energy of the n=2 IPS (and the n=3 IPS as well) the short alkyl chain does not provide a significant barrier between the attractive sulfur portion of the adsorbate and the attractive image potential induced in the vacuum. The electron is able to spread out over the entire region, and the lifetime reflects the resulting overlap with the substrate. For the butylthiolate layer, the longer alkyl chain presents a more significant barrier between the inside and outside portions of the potential. This barrier reduces the ability of the n=2 IPS electron to spread throughout the region, forcing the electron density more into the layer and increasing the overlap of the electronic wavefunction with the metal. The drastically shortened lifetime reflects this increase in overlap.

Adsorption of acetonitrile layers onto the Ag(111) surface changes the static global workfunction to 3.8 eV for a one layer and 3.9 eV for two layers of coverage. The strong charge dipole interaction between the excited IPS electrons results in a reorientation of the molecular dipoles to solvate the electron. One of the surprising results of this study is that this solvation process occurs for delocalized electrons as well as localized electrons. Delocalized electron solvation has not been observed in liquid phase experiments and the observation of it is unique to the two dimensional system studied here. The solvation is explained as a change in the local workfunction. The rotation of the molecular dipoles changes the local surface potential in the vicinity of the electron. This shift in the potential is equivalent to a shift in the workfunction. This change in the local surface potential is modelled by a pair of oppositely charged disks representing the change in the projection

of the molecular dipole onto the surface normal. This measured solvation energy is within the range of and on the same order of magnitude as the change in the local workfunction obtained from the model. One important aspect of these results is that the IPS can be used to monitor solvation at a two dimensional polar interface. Another benefit of applying the TPPE technique to investigate interfacial solvation is that the solvation dynamics are separate from the localization dynamics.

Bibliography

[1] W. Ho. *J. Phys. Chem.*, 100(31):13050, 1996.

[2] J. W. Gadzuk. *Phys. Rev. Lett.*, 76(22):4234, 1996.

[3] J. A. Prybyla, H. W. K. Tom, and G. D. Aumiller. *Phys. Rev. Lett.*, 64(4):503, 1992.

[4] D.G. Busch, S. Gao, R.A. Pelak, M.F. Booth, and W. Ho. *Phys. Rev. Lett.*, 75:673, 1995.

[5] Y. N. Gartstein and E. M. Conwell. *Chem. Phys. Lett.*, 255:93, 1996.

[6] Y. Shen, M. W. Klein, D. B. Jacobs, J. C. Scott, and G. G. Malliaras. *Phys. Rev. Lett.*, 86(17):3867, 2001.

[7] I. H. Campbell, T. W. Hagler, D. L. Smith, and J. P. Ferraris. *Phys. Rev. Lett.*, 76(11):1900, 1996.

[8] M.N. Bussac, D. Michoud, and L. Zuppiroli. *Phys. Rev. Lett.*, 81(8):1678, 1998.

[9] T. Kugler, M. Logdlund, and W.R. Salaneck. *Acc. Chem. Res.*, 32:225, 1999.

[10] I. H. Campbell, S. Rubin, T. A. Zawodzinski, J. D. Kress, R. L. Martin, D. L.

Smith, N. N. Baraskkov, and J. P. Ferraris. *Physical Review B (Condensed Matter)*, 54(20):R14321, 1996.

[11] I. H. Campbell, J. D. Kress, R. L. Martin, D. L. Smith, N. N. Barashkov, and J. P. Ferraris. *Applied Physics Letters*, 71(24):3528, 1997.

[12] M. A. Reed, C. Zhou, C. J. Muller, T. P. Burgin, and J. M. Tour. *Science*, 278(5336):252, 1997.

[13] A. Dhirani, P. H. Lin, P. Guyot-Sionnest, R. W. Zehner, and L. R. Sita. *Journal of Chemical Physics*, 106(12):5249, 1997.

[14] T. Vondrak, C. J. Cramer, and X. Y. Zhu. *Journal of Physical Chemistry B*, 103(42):8915, 1999.

[15] T. Vondrak, H. Wang, P. Winget, C. J. Cramer, and X. Y. Zhu. *J. Am. Chem. Soc.*, 122(19):4700, 2000.

[16] A.D. Miller, K.J. Gaffney, S.H. Liu, P. Szymanski, S. Garrett-Roe, C.M. Wong, and C.B. Harris. *J. Phys. Chem. B.*, (in press).

[17] B.J. Loughnane, R.A. Farrer, A. Scodinu, T. Reilly, and J.T. Fourkas. *J. Phys. Chem. B*, 104:5421, 2000.

[18] D.M. Willard, R.E. Riter, and N.E. Levinger. *J. Am. Chem. Soc.*, 120:4151, 1998.

[19] D. Zimdars and K. B. Eisenthal. *J. Phys. Chem. A*, 103(49):10567, 1999.

[20] I. Benjamin. *Chem. Rev.*, 96:1449, 1996.

[21] R. M. Stratt and M. Maroncelli. *J. Phys. Chem.*, 100(31):12981. Review Year = 1996.

[22] G. R. Fleming and M. H. Cho. *Annu. Rev. Phys. Chem.*, 47:109, 1996.

[23] P.J. Rossky and J.D. Simon. *Nature*, 370:263, 1994.

[24] P. K. Walhout, J. C. Alfano, Y. Kimura, C. Silva, P. J. Reid, and P. F. Barbara. *Chemical Physics Letters*, 232(1-2):135, 1995.

[25] J. A. Kloepfer, V. H. Vilchiz, V. A. Lenchenkov, and S. E. Bradforth. *Chemical Physics Letters*, 298(1-3):120, 1998.

[26] W.R. Merry. *Image Potential States at Dielectric-Metal Interfaces.* PhD thesis, University of California at Berkeley, 1992.

[27] The band structure plot and band energies were obtained online at: http://manybody.nrl.navy.mil/esdata/database.html.

[28] S.G. Davison and M. Stęślicka. *Basic Theory of Surface States.* Oxford University Press, New York, 1992.

[29] D.J. Griffiths. *Introduction to Electrodynamics Second Edition.* Prentice Hall, New Jersey, 1989.

[30] C. C. Grimes and T. R. Brown. *Phys. Rev. Lett.*, 32:280, 1974.

[31] V. Dose, W. Altmann, A. Goldmann, U. Kolac, and J. Rogozik. *Phys. Rev. Lett.*, 52:1919, 1984.

[32] P. Johnson and N. Smith. *Phys. Rev. B*, 27:2527, 1983.

[33] D. Straub and F. J. Himpsel. *Phys. Rev. Lett.*, 52:1922, 1984.

[34] D. Straub and F. J. Himpsel. *Phys. Rev. B*, 33:2256, 1986.

[35] K. Giesen, F. Hage, F. J. Himpsel, H. J. Reiss, and W. Steinmann. *Phys. Rev. B*, 33:5241, 1986.

[36] K. Giesen, F. Hage, F. J. Himpsel, H. J. Reiss, and W. Steinmann. *Phys. Rev. B*, 35:971, 1987.

[37] K. Giesen, F. Hage, F. J. Himpsel, H. J. Reiss, W. Steinmann, and N. V. Smith. *Phys. Rev. B*, 35:975, 1987.

[38] P. M. Echenique and J. B. Pendry. *J. Phys. C:Solid State Phys.*, 11:2065, 1978.

[39] P.M. Echenique and J.B. Pendry. *Prof. Surf. Sci.*, 32(2):111, 1989.

[40] N. V. Smith. *Rep. Prog. Phys.*, 51:1227, 1988.

[41] N. V. Smith. *Phys. Rev. B*, 32:3549, 1985.

[42] K. Giesen, F. Hage, F. J. Himpsel, H. J. Riess, and W. Steinmann. *Phys. Rev. Lett.*, 55:300, 1985.

[43] R. W. Schoenlein, J. G. Fujimoto, G. L. Eesley, and T. W. Capehart. *Phys. Rev. Lett.*, 61:2596, 1988.

[44] R. W. Schoenlein, J. G. Fujimoto, G. L. Eesley, and T. W. Capehart. *Phys. Rev. B*, 41:5436, 1990.

[45] R. W. Schoenlein, J. G. Fujimoto, G. L. Eesley, and T. W. Capehart. *Phys. Rev. B*, 43:4688, 1991.

[46] P. L. de Andrés, P. M. Echenique, and F. Flores. *Phys. Rev. B*, 39:10356, 1989.

[47] P. L. de Andrés, P. M. Echenique, and F. Flores. *Phys. Rev. B*, 35:4529, 1987.

[48] P. M. Echenique, F. Flores, and F. Sols. *Phys. Rev. Lett.*, 55:2348, 1985.

[49] E.V. Chulkov, I. Sarría, V.M. Silkin, J.M. Pitarke, and P.M. Echenique. *Phys. Rev. Lett.*, 80(22):4947, 1998.

[50] M.W. Cole. *Phys. Rev. B*, 3(12):4418, 1971.

[51] M. Wolf, E. Knoesel, and T. Hertel. *Phys. Rev. B*, 54:R5295, 1996.

[52] K.J. Gaffney, S.H. Liu, A.D. Miller, P. Szymanski, and C.B. Harris. *J. Chin. Chem. Soc.*, 47(4A):759, 2000.

[53] N.-H. Ge, C.M Wong, R.L. Lingle, J.D. McNeill, K.J. Gaffney, and C.B. Harris. *Science*, 279(5348):202, 1998.

[54] R.L. Lingle, N.-H. Ge, R.E. Jordan, J.D. McNeill, and C.B. Harris. *Chem. Phys.*, 205(1-2):191, 1996.

[55] N.-H. Ge, C.M. Wong, and C.B. Harris. *Acc. Chem. Res.*, 33:111, 2000.

[56] J.D. McNeill, R.L. Lingle, N.-H. Ge, C.M. Wong, and C.B. Harris. *Phys. Rev. Lett.*, 79(23):4645, 1997.

[57] K.J. Gaffney, C.M. Wong, S.H. Liu, A.D. Miller, , J.D. McNeill, and C.B. Harris. *Chem. Phys.*, 251(1-3):99, 2000.

[58] J.D. McNeill, R.L. Lingle, R.E. Jordan, D.F. Padowitz, and C.B. Harris. *J. Chem. Phys.*, 105(9):3883, 1996.

[59] N.-H. Ge. *Ultrafast Studies of Electron Dynamics at Metal-Dielectric Interfaces.* PhD thesis, University of California at Berkeley, 1998.

[60] C.M. Wong. *Femtosecond Studies of Interband and Intraband Electron Dynamics at Dielectric-Metal Interfaces.* PhD thesis, University of California at Berkeley, 2000.

[61] J.D. McNeill. *Ultrafast Dynamics of electrons at Interfaces.* PhD thesis, University of California at Berkeley, 1999.

[62] H. Petek, M.J. Weida, H. Nagano, and S. Ogawa. *Science*, 288(5470):1402, 2000.

[63] S. Ogawa, H. Nagano, and H. Petek. *Phys. Rev. Lett.*, 82(9):1931, 1999.

[64] G.M. Watson, P.A. Brühwiler, H.J. Sagner, K.H. Frank, and E.W. Plummer. *Phys. Rev. B*, 50(23):17678, 1994.

[65] W. Jacob, E. Bertel, and V. Dose. *Physical Review B (Condensed Matter)*, 35(11):5910, 1987.

[66] P. A. Dowben, Y. J. Kime, S. Varma, M. Onellion, and J. L. Erskine. *Physical Review B (Condensed Matter)*, 36(5):2519, 1987.

[67] Ed. S.D. Kevan. *Angle-Resolved Photoemission.* Prentice Hall, New Jersey, 1989.

[68] R. Haight. *Surf. Sci. Reports*, 21(8):277, 1995.

[69] C.B. Harris, N.-H. Ge, R.L. Lingle, J.D. McNeill, and C.M. Wong. *Ann. Rev. Phys. Chem.*, 48:711, 1997.

[70] T. Fauster and W. Steinmann. Two photon photoemission spectroscopy of image states. In P. Halevi, editor, *Photonic Probes of Surfaces*, page 347. Elsevier, Amsterdam, 1995.

[71] N. Memmel. *Surface Science Reports*, 32(3-4):91, 1998.

[72] S. Ogawa, H. Nagano, and H. Petek. *Phys. Rev. Lett.*, 78(7):1339, 1997.

[73] H. Petek, H. Nagano, and S. Ogawa. *Phys. Rev. Lett.*, 83(4):832, 1999.

[74] S. Ogawa, H. Nagano, and H. Petek. *Phys. Rev. B*, 55(16):10869, 1997.

[75] H. Petek, A.P. Heberle, W. Nessler, H. Nagano, S. Kubota, S. Matsunami, N. Moriya, and S. Ogawa. *Phys. Rev. Lett.*, 79(23):4649, 1997.

[76] C. A. Schmuttenmaer, M. Aeschlimann, H. E. Elsayed-Ali, R. J. D. Miller, D. A. Mantell, J. Cao, and Y. Gao. *Phys. Rev. B*, 50:8957, 1994.

[77] W. S. Fann, R. Storz, H. W. K. Tom, and J. Bokor. *Phys. Rev. Lett.*, 68:2834, 1992.

[78] J. Cao, Y. Gao, R. J. D. Miller, H. E. Elsayed-Ali, and D. A. Mantell. *Phys. Rev. B*, 56:1099, 1997.

[79] R. Haight and M. Baeumler. *Phys. Rev. B*, 46:1543, 1992.

[80] A. Rettenberger and R. Haight. *Phys. Rev. Lett.*, 76:1912, 1992.

[81] M. Aeschlimann, M. Bauer, S. Pawlik, R. Burgermeister, D. Oberli, and H.C. Siegmann. *Phys. Rev. Lett.*, 79(25):5158, 1997.

[82] C.M. Wong, J.D. McNeill, K.J. Gaffney, N.-H. Ge, A.D. Miller, S.H. Liu, and C.B. Harris. *J. Phys. Chem. B*, 103:282, 1999.

[83] J. E. Ortega, F. J. Himpsel, R. Haight, and D. R. Peale. *Phys. Rev. B*, 49(19):13859, 1994.

[84] S. Bao, C. F. McConville, and D. P. Woodruff. *Surface Science*, 187(1):133, 1987.

[85] D. L. Seymour, S. Bao, C. F. McConville, M. D. Crapper, D. P. Woodruff, and R. G. Jones. *Surface Science*, 189/190:529, 1987.

[86] B. Heinz and H. Morgner. *Surface Science*, 372(1-3):100, 1997.

[87] T. Soloman, H. Christmann, and J. Baumgrtel. *J. Phys. Chem.*, 93:7199, 1989.

[88] P. A. Stevens, R. J. Madix, and J. Stohr. *J. Chem. Phys.*, 91(7):4338, 1989.

[89] T. Soloman, H Christmann, A. Neumann, and J. Baumgrtel. *J. Electroanal. Chem.*, 309:355, 1991.

[90] K. Wandelt. In P. Wissman, editor, *Thin Metal Films and Gas Chemisorption*, page 280. Elsevier, Amsterdam, 1987.

[91] K. Wandelt. *Appl. Surf. Sci.*, 111:1, 1997.

[92] S. N. Yaliraki and M. A. Ratner. *Journal of Chemical Physics*, 109(12):5036, 1998.

[93] L.H. Dubois and R.G. Nuzzo. *Annu. Rev. Phys. Chem.*, 43:437, 1992.

[94] A. Ulman. *Chem. Rev.*, 96(4):1533, 1996.

[95] H. Sellers, A. Ulman, Y. Shnidman, and J. E. Eilers. *Journal of the American Chemical Society*, 115(21):9389, 1993.

[96] A. Dhirani, M. A. Hines, A. J. Fisher, O. Ismail, and P. Guyot-Sionnest. *Langmuir*, 11(7):2609, 1995.

[97] H. Rieley, G. K. Kendall, R. G. Jones, and D. P. Woodruff. *Langmuir*, 15(26):8856, 1999.

[98] L. A. Bumm, J. J. Arnold, T. D. Dunbar, D. L. Allara, and P. S. Weiss. *J. Phys. Chem. B*, 103(38):8122, 1999.

[99] L. A. Bumm, J. J. Arnold, M. T. Cygan, T. D. Dunbar, T. P. Burgin, II Jones, L., D. L. Allara, J. M. Tour, and P. S. Weiss. *Science*, 271(5256):1705, 1996.

[100] M. T. Cygan, T. D. Dunbar, J. J. Arnold, L. A. Bumm, N. F. Shedlock, T. P. Burgin, L. Jones II, D. L. Allara, J. M. Tour, and P. S. Weiss. *J. Am. Chem. Soc.*, 120(12):2721, 1998.

[101] K. Slowinski, R. V. Chamberlain, C. J. Miller, and M. Majda. *J. Am. Chem. Soc.*, 119(49):11910, 1997.

[102] G. E. Poirier and E. D. Pylant. *Science*, 272(5265):1145, 1996.

[103] M. Buck, M. Grunze, F. Eisert, J. Fischer, and F. Trager. *J. Vac. Sci. Technol. A*, 10(4):926, 1992.

[104] K.J. Gaffney. *Dynamics of Electrons Photoinjected into Organic Semiconductor and Aromatic-Metal Interfaces.* PhD thesis, University of California at Berkeley, 2001.

[105] D.R. Lide, editor. *CRC Handbook of Chemistry and Physics.* CRC Press, Boca Raton, Florida, 1990-1991.

ERNEST ORLANDO LAWRENCE BERKELEY NATIONAL LABORATORY
ONE CYCLOTRON ROAD | BERKELEY, CALIFORNIA 94720

Prepared for the U.S. Department of Energy under Contract No. DE-AC03-76SF00098